Laboratory Measurements of Sea Salt Aerosol Refractive Index

Thesis submitted for the degree of Doctor of Philosophy

Ranah Irshad

Magdalen College

Atmospheric, Oceanic and Planetary Physics

University of Oxford

Laboratory Measurements of Sea Salt Aerosol Refractive Index

Ranah Irshad, Magdalen College, DPhil Thesis submitted Trinity 2008

Abstract

Aerosols play a crucial role in atmospheric reactions and radiative transfer. It is important to understand their properties and behaviour in order to better understand the behaviour of the Earth's atmosphere. Transmission measurements of laboratory generated sodium chloride and sea salt aerosols (SSA) were made with a view to retrieving refractive index spectra using a classical damped harmonic oscillator model. The resulting extinction spectra showed significant differences when compared to spectra calculated from current refractive indices and volume mixing rules. New refractive index spectra were therefore derived from the new measurements for six different relative humidity values, and at a higher resolution than any other SSA refractive index data to date.

Volume mixed calculations performed using the new data and the refractive indices of water result in spectra for wet SSA that are different to direct measurements. This implies that the volume mixing rules are inadequate in describing the refractive indices of solutions. Furthermore, the existing data for the real and imaginary parts of the refractive indices of dry sea salt aerosol are found not to display the Kramers-Kronig relationship. This implies that the original data used for the volume mixing calculations is also inaccurate. This has significant implications for the numerous studies performed every year with volume mixed refractive indices.

Additional measurements on ammonium sulphate and nitrate show a possible variation of the extinction spectra with temperature, which provides justification for more detailed measurements.

Contents

List of Figures

List of Tables

Chapter 1

Introduction

Atmospheric aerosols can have significant forcing effects on the radiation budget of the atmosphere. Aerosol particles may act as cloud condensation nuclei and influence the lifetime of clouds (Penner et al., 2001; Lohmann and Feichter, 2005) or they can influence radiative transfer by scattering and absorbing solar radiation (IPCC, 2007). They also play a crucial role in atmospheric chemical reactions. The optical properties of aerosols are particularly important in order to perform radiative transfer calculations in global climate models, and allow the radiative effect of such aerosols on the climate to be estimated (Hess et al., 1998; Dobbie et al., 2003). In fact the need for refined optical aerosol models for improving satellite retrieval algorithms has been identified by many authors (Dubovik et al., 2002; King et al., 1999; Torres et al., 1998).

In the following chapter, the importance of aerosols is discussed briefly, with particular reference to sea salt aerosol, as this forms the basis of the experimental work discussed later. The optical properties of aerosols are also discussed, as are the various ways in which aerosol particles interact with their environment.

1.1 Importance of Aerosols

An aerosol may be defined as a suspension of small particles or droplets in a gas. Aerosols are present throughout the atmosphere and occur both naturally (e.g. volcanic ash) and artificially (e.g. as a result of industrial combustion processes). Primary aerosols are those that are emitted directly from the source, for example: windblown dust from quarries or marine aerosols arising from sea spray. Secondary aerosols are those which are formed as a result of chemical reactions in the atmosphere.

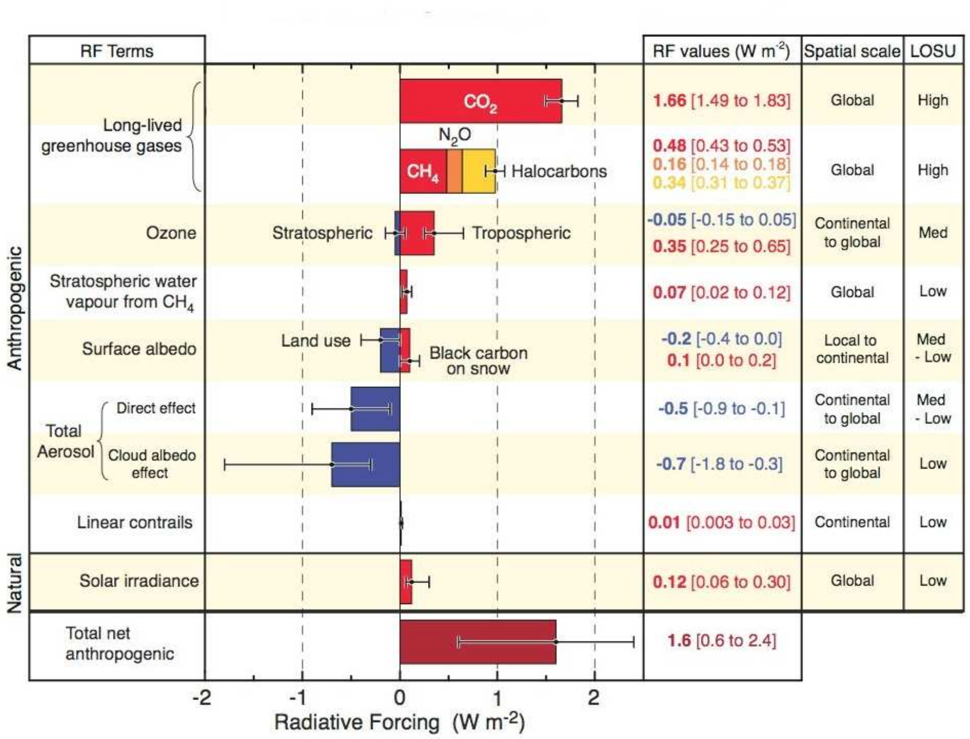

Figure 1.1: Global radiative forcing estimates for a number of different sources including aerosols. Figure taken from IPCC (2007). In the final column, LOSU is the level of scientific understanding.

Aerosols have a significant effect on the Earth's radiation balance (figure 1.1).

This is the balance that arises from the heating of the planet by solar radiation and cooling due to terrestrial infra-red radiation escaping into space. The effects of aerosols on radiative balance may be direct or indirect. Direct effects involve the scattering of short-wave radiation back into space by aerosol particles, thereby reducing visibility and altering climate. Most aerosols cause cooling of the atmosphere in this way, although short-wave absorption by carbonaceous aerosols may also lead to a warming of the atmosphere as well as a resultant cooling of the surface. Indirect effects involve cooling as a result of the influence of aerosols on cloud properties (Vinoj and Satheesh, 2004). Aerosols act as cloud condensation nuclei (CCN) (Twomey, 1960) and so can affect the microphysical properties of clouds. An increase in aerosol concentrations means an increase in CCN so there are more cloud droplets and therefore more scattering of solar radiation. An increase in aerosol concentration will also reduce the effective size of cloud droplets, affecting the lifetime of the clouds. This will increase the cloud albedo, causing cooling and thus affecting the Earth's radiation budget (Twomey, 1977a).

Latham and Smith (1990) propose a possible negative feedback mechanism on climate change as a result of increased aerosol particle number densities arising from increased wind speeds associated with global warming (Lewis and Schwartz, 2004). Stronger wind speed would suspend more material, increasing average aerosol concentrations and thus increasing the effects of aerosols on the climate.

It is also believed that aerosols have an effect on crop production (Chameides et al., 1999). This is due to the attenuation of radiation by aerosols, which results in less photosynthetically active radiation reaching the surface (radiation of wavelengths 400–700 nm).

Of course, there is a great deal of spatial and temporal variation in aerosol concentration. For example, emissions associated with biomass burning and volcanic eruptions will clearly be dependent on those events. Emissions of industrial sulphate aerosols are also specific to industrial areas and the magnitude of these emissions has doubled since 1950 (Andreae, 1995). The distance travelled by an aerosol from its source will depend on its residence time in the atmosphere. This in turn depends on the size distribution, which will be discussed later in this chapter.

There is currently a great deal of uncertainty regarding the overall effect of direct and indirect forcing by aerosols (IPCC, 2007). It is crucial to reduce this uncertainty in order to improve current models of climate change. Direct forcing calculations can be made using the single-scattering[1] optical properties of aerosols to determine how single particles interact with radiation (Vinoj and Satheesh, 2004). This is then extended to model the radiative properties of whole layers of aerosols. Currently direct aerosol forcing estimations have been made primarily for anthropogenic aerosols. However, the contribution to both direct and indirect forcing from aerosols such as sea-salt and compounds of ammonia has been the subject of few studies (IPCC, 2007).

1.2 Aerosol Optical Properties

In order to estimate the forcing due to aerosols it is necessary to characterise their optical properties. These include the single scattering albedo, the extinction and the asymmetry parameter. These in turn depend on the particle shape, size distribution and refractive index. All of these properties will be defined and discussed in this section.

---

[1] The term 'single-scattering' refers to any event where radiation is scattered from a single particle.

1.2.1 Single-Scattering and Extinction

When an atom or molecule is exposed to light, its electric charges (i.e. the electrons) become excited and begin to oscillate. The excited charges then reradiate some of the energy from the incident radiation as scattered light (Seinfeld and Pandis, 1998). The remainder of the extinction is absorbed. The scattering and absorption make up the total attenuation of the incident light and this is the particle extinction. The extinction cross-section, C_{ext}, is then given by equation 1.1.

$$C_{ext} = C_{scat} + C_{abs} \tag{1.1}$$

where C_{scat} is the single particle scattering cross-section and C_{abs} is the single particle absorption cross-section, both with units of m^2. This is the projected area of the particle that would geometrically intercept the total amount of radiation actually scattered and absorbed by the particle. Then defining Q_{ext} as the dimensionless extinction efficiency C_{ext}/A, where A is the particle cross-sectional area, we can write:

$$Q_{ext} = Q_{scat} + Q_{abs} \tag{1.2}$$

where Q_{scat} and Q_{abs} are the scattering and absorption efficiencies respectively. The ratio of Q_{scat} to Q_{ext} is called the single scattering albedo, ω, and represents the amount of attenuated light that is scattered by the particle (Seinfeld and Pandis, 1998).

1.2.2 Asymmetry Parameter

As scattered light from a particle is not always isotropic, the scattering phase function, P, is used to describe the angular distribution of scattered light intensity. It is defined as the scattered intensity per unit solid angle in a given direction compared to the average intensity in all directions (NASA, 2008). The asymmetry parameter, g, is then the average of the cosine of the scattering angle, weighted by the phase function P (see equation 1.3).

$$g = \frac{1}{2}\int_0^{\pi} \cos\theta P(\theta)\sin\theta\,\mathrm{d}\theta \tag{1.3}$$

For isotropic light scattering, $g = 0$. When scattering is mainly in the forward direction, $\theta < 90\,^{\circ}$ and $g > 0$; when scattering is mainly in the backwards direction, $\theta > 90\,^{\circ}$ and $g < 0$.

The asymmetry parameter will be affected by the shape of the aerosol particle. In general, the amount of side- and back-scattering from non-spherical particles is greater than that from spherical particles (Syvitski, 2007), although the amount of forward-scattering by large[2] particles is relatively insensitive to particle shape (Hodkinson and Greensleaves, 1963).

1.2.3 Complex Refractive Index

The complex refractive index, $m = n+ik$, is a key parameter governing the extinction of light by a particle, and is determined by that particle's chemical composition. It describes the variation of the speed of light when travelling through a medium,

---

[2] Here, particles are considered large if their diameter is greater than the wavelength of incident light.

usually with respect to a vacuum or air, as a function of wavelength. The real and imaginary parts of the refractive index, n and k, represent the non-absorbing and absorbing components of a particle respectively (Seinfeld and Pandis, 1998). The role of the complex refractive index in the scattering and absorption of light by aerosol particles will be discussed in more detail in chapter 2.

1.2.4 Size Distribution

Atmospheric aerosols are divided into three main size[3] classes. These are the fine particles (radius $< 0.1\mu$m), the accumulation mode particles ($0.1\,\mu$m $<$ radius $<\ 1\,\mu$m) and the coarse particles (radius $> 1\,\mu$m). The accumulation mode is considered the most important with regards to radiative forcing (Charlson and Heintzenberg, 1994) as particles in this mode have the longest residence times in the atmosphere. They can be carried up to altitudes were cloud interactions are possible, as well as over long geographical distances.

Atmospheric aerosols have commonly been described by three size distribution functions. These include the Junge power-law function (Junge, 1958), the modified gamma distribution (Deirmendjian, 1969) and the lognormal distribution.

Junge Power-Law

This function describes the size of aerosol particles with a power-law distribution function (see equation 1.4).

$$\frac{\mathrm{d}N}{\mathrm{d}\log(r)} = \ln(10) C r_0 \left(\frac{r_0}{r}\right)^{\alpha-1} \tag{1.4}$$

---

[3] Throughout this thesis, references to size imply the aerosol particle radius.

where $C = n(r_0)$, the number density of particles with $r = r_0$, N is the number density of particles with $r > r_0$, α is a constant such that $3 < \alpha < 5$ and r_0 is an arbitrary radius. This equation holds over the range $0.1\,\mu\mathrm{m} \leq r < 100\,\mu\mathrm{m}$ (d'Almeida et al., 1991).

The power-law distribution is relatively easy to apply and understand; however it is often inadequate in accurately describing any but the simplest of aerosol size distributions (Seinfeld and Pandis, 1998).

Modified Gamma Distribution

This is the generalised form of a size distribution originally intended to apply to clouds, and can be represented by equation 1.5 which holds for values of particle radius, r, such that $0 \leq r \leq \infty$.

$$\frac{\mathrm{d}N}{\mathrm{d}r} = ar^{\alpha} \exp(-br^{\gamma}) \tag{1.5}$$

Here, α, a, b and γ are all positive parameters. However, the physical meanings of these parameters are not well understood, and the use of this distribution can often be cumbersome (d'Almeida et al., 1991).

Lognormal Distribution

This distribution was introduced by Davies (1974) and describes the size distribution of particles from a single source, produced via a single mechanism. For particles from a source i:

$$\frac{\mathrm{d}N_i(r)}{\mathrm{d}(\log r)} = \frac{N_i}{(2\pi)^{\frac{1}{2}} \log(\sigma_i)} \exp\left(-\frac{(\log r - \log r_{m_i})^2}{2(\log \sigma_i)^2}\right) \tag{1.6}$$

where r_m is the median particle radius, $\log r_{m_i}$ is the most probable value of $\log r$ and $\log \sigma_i$ is the standard deviation of $\log r$.

This distribution can be extended to describe the sum of a number of lognormal distributions, from a number of different sources. This is useful as it means a mixture of particles from different sources may be accurately described.

Of the three common distribution functions, the lognormal distribution most often provides the best fit to observed particle size distributions (Hinds, 1982) and is regularly used in atmospheric aerosol studies. This is therefore the function that will be used to model aerosol size distribution in this thesis.

1.3 Aerosol Interactions

This section describes the way aerosols interact with their environment. There are a number of processes that involve a change in the physical or chemical properties of aerosol particles, and many of these take place simultaneously. The effects that these processes have on individual particles will now be considered for some of the most important interactions.

1.3.1 Gravitational Settling and Brownian Motion

The time taken for a particle to reach its terminal settling velocity will depend on the force of gravity and the drag force experienced by the particle as it moves through air, or another fluid. The drag experienced by a single, spherical particle is given by Stokes' Law:

$$F_{drag} = 6\pi\mu r v \tag{1.7}$$

where μ is the fluid viscosity, r is the particle radius and v is the speed of the particle, relative to the fluid (Seinfeld and Pandis, 1998). This may be balanced with the gravitational force to obtain the terminal velocity, V_s of the aerosol particle:

$$V_s = \frac{2\rho_p r^2 g}{9\mu} \tag{1.8}$$

where ρ_p is the particle density and g is the gravitational acceleration (Baron and Willeke, 2001). The relaxation time, T_s, is then the time taken for the particle to reach terminal velocity:

$$T_s = \frac{2r^2}{9v}\left|1 - \frac{\rho_p}{\rho_0}\right| \tag{1.9}$$

where v is the particle velocity and ρ_0 is the fluid density. Detailed derivations of these equations may be found in the literature, for example, Baron and Willeke (2001); Seinfeld and Pandis (1998). Table 1.1 gives the relaxation times for particles of varying sizes.

Particle Radius (μ)	Relaxation Time (s)
0.05	9.2×10^{-8}
0.25	1.0×10^{-6}
0.5	3.6×10^{-6}
2.5	7.9×10^{-5}
5.0	3.1×10^{-4}

Table 1.1: Table showing the time taken to reach terminal velocity in air for particles of unit density. Taken from Seinfeld and Pandis (1998).

As the particle size becomes smaller, the distance travelled by the particle due to gravitational settling becomes smaller, while the distance travelled due to Brownian motion becomes more important. Brownian motion describes the movement of a particle due to random bombardment by the surrounding fluid molecules and may be considered as a diffusion process. When comparing the relative importance of Brownian motion and gravitational settling, Twomey (1977b) states that a particle of radius 1 μm will diffuse a distance of approximately 4 μm while falling 200 μm under gravity. However, a particle of radius 0.1 μm will diffuse a distance of 20 μm while falling only 4 μm. Brownian motion has a significant effect on the coagulation rate of aerosol particles (Pruppacher and Klett, 1997). However, Seinfeld and Pandis (1998) state that it is not expected to be an efficient transport mechanism for aerosol particles in the atmosphere.

1.3.2 Thermophoresis

If a temperature gradient exists in the aerosol-carrying fluid there will be a resultant force from the higher to the lower temperature areas due to the difference in the kinetic energies of the hot and cold aerosol particles. This effect is known as thermophoresis and is usually negligible compared to other forces experienced by atmospheric aerosols, unless the temperature gradient is very large (Seinfeld and Pandis, 1998). Table 1.2 gives the thermophoretic and settling velocities of various particles in air.

1.3.3 The Kelvin Effect

Aerosols that are water soluble, such as sulphate or sea salt aerosols, are hygroscopic. This means that they can absorb moisture from the surrounding atmosphere. The physical changes in the aerosol particles will be dependent on the ambient relative humidity (RH). This is defined as the ratio of the partial pressure of water to the

Thermophoretic Velocity ($\mathbf{cm\,h^{-1}}$)			
Particle Radius (μ)	$\nabla T = 1\,\mathrm{K\,cm^{-1}}$	$\nabla T = 10\,\mathrm{K\,cm^{-1}}$	Terminal Velocity ($\mathrm{cm\,h^{-1}}$)
0.005	0.74	7.4	0.02
0.025	0.70	7.0	0.14
0.05	0.68	6.8	0.31
0.25	0.55	5.5	3.6
0.5	0.42	4.2	12.6
2.5	0.15	1.5	279
5.0	0.10	1.0	1098

Table 1.2: Table showing the thermophoretic and terminal settling velocities of particles of various sizes. Taken from Seinfeld and Pandis (1998).

saturation vapour pressure of water at a particular temperature[4], and is usually expressed as a percentage. However, this definition of RH usually applies to a flat liquid surface, as this is the interface for which the saturation vapour pressure is defined. Liquid aerosol particles have a curved surface for which a greater partial pressure is required in order to maintain equilibrium at a particular temperature. This is known as the Kelvin effect (Thomson, 1871) and becomes increasingly significant as particle size decreases resulting in a more extreme curvature of the surface. The relationship between the partial pressure over a droplet of radius, r is given by the Kelvin equation:

$$p = p_0 \exp\left(\frac{2\gamma V_m}{rRT}\right) \tag{1.10}$$

where p is the partial pressure, p_0 is the saturation vapour pressure, γ is the surface tension, V_m is the molar volume of the liquid, R is the universal gas constant and T is the temperature. The Kelvin effect is described in greater detail by Adamson and

---

[4] Partial pressure is the pressure that would be exerted by a component of a gas mixture, if that component were to occupy a fixed volume alone. The saturation vapour pressure is the pressure of a vapour when it is in equilibrium with its liquid phase (Baron and Willeke, 2001).

Gast (1997), and a complete derivation of the Kelvin equation has been outlined by Seinfeld and Pandis (1998) .

1.3.4 Nucleation

The process of formation of an aerosol droplet from vapour is known as nucleation. When this occurs spontaneously in the absence of other particles, it is known as homogeneous nucleation. For this process to take place, the air must be supersaturated so that the relative humidity is greater than 100 %. This is possible for very small particles since, from equation 1.10, the relative humidity is proportional to $\exp\left(\frac{a}{r}\right)$, where a is a constant at any particular temperature and pressure, for a particular liquid. This means that, as the particle radius becomes smaller, the relative humidity can become very large. Pure water at 20 °C requires an RH value of 350 % or more in order for droplets to form by homogeneous nucleation (Baron and Willeke, 2001).

The conditions required for homogeneous nucleation are rarely present in the atmosphere. A more common process is heterogeneous nucleation, where vapour condenses onto existing sub-micrometer particles known as condensation nuclei. Where the condensation nuclei are soluble, they have a strong affinity for water that allows condensation and droplet growth at lower RH values than would be required for insoluble nuclei (Pruppacher and Klett, 1997). This means that heterogeneous nucleation is much more likely to occur in the atmosphere than homogeneous nucleation.

1.3.5 Coagulation

Coagulation of aerosol particles is due to collisions between those particles and leads to an increase in size as well as a decrease in the particle number concentration. When inter-particle collisions occur due to Brownian motion, the process is termed thermal coagulation. The rate of this thermal coagulation is directly proportional to temperature and inversely proportional to the particle diameter and the viscosity of the gas in which the particle is carried.

Aerosol particles also experience coagulation due to shear flow of the surrounding air, as well as the gravitational settling of particles onto each other. However, the coagulation rates due to these kinetic processes are much lower than for thermal coagulation (Seinfeld and Pandis, 1998).

1.4 Sea Salt Aerosols

Marine aerosols provide a significant contribution to the aerosol environment, due to the large source area of the ocean, which covers approximately 70 % of the Earth's surface.

Sea salt aerosol (SSA) is a component of marine aerosol made up of seawater and dry sea salt particles. The chemical composition of SSA particles may vary with location and time. For example, coastal waters may be polluted with chemical run-offs from land, which means that the SSA produced in these areas may contain more nitrates or sulphates than that produced over oceanic waters (Fang et al., 1998). The elemental ratios of chlorine, sodium and sulphur in many sea salt aerosol particles may differ from those in normal seawater (McInnes et al., 1994). However, it is frequently assumed that the composition of SSA particles is approximately equivalent to that of seawater, with respect to the major components. These are given in table 1.3.

Species	Mass Fraction	Mole Fraction	Molarity (mol)
H_2O	0.9648	0.9795	55.510
Cl^-	0.0194	0.0100	0.566
SO_4^{2-}	0.0027	0.0005	0.029
HCO_3^-	0.0001	< 0.0001	0.002
Br^-	0.0001	< 0.0001	0.001
Na^+	0.0108	0.0086	0.486
Mg^{2+}	0.0013	0.0010	0.055
Ca^{2+}	0.0004	0.0002	0.011
K^+	0.0004	0.0002	0.011
minor species	< 0.0001	< 0.0001	0.001

Table 1.3: Table showing the composition of seawater of salinity 35. Based on Lewis and Schwartz (2004), table 6.

SSA is produced when winds on the surface of the ocean form and break waves which then draw in air to different depths. These air bubbles, as well as bubbles from other mechanisms, rise to the surface and burst, dispersing droplets of seawater into the atmosphere. Similarly, any other mechanism that causes seawater droplets to be sprayed upwards may contribute to sea salt aerosol formation.

1.4.1 Importance of SSA

Like many other aerosols, sea salt aerosols act as cloud condensation nuclei (Twomey and McMaster, 1955); they may also act as sinks for condensable gases, affecting the deposition rate of nitrogen in the form of ammonia to the ocean and thus possibly inhibiting the formation of other aerosol particles (Savoie and Prospero, 1982). Coarse SSA particles cause corrosion and are a main contributor to ocean-atmosphere fluxes of organic substances, electric charge, micro-organisms etc. SSA also plays a part in the atmospheric cycles of chlorine and other halogens (Finlayson-Pitts and Hemminger, 2000).

Recent observations suggest that most of the accumulation mode aerosols in the marine boundary layer contain sea salt, and that this sea salt aerosol is responsible for the majority of aerosol-scattered light (Murphy et al., 1998). Accumulation mode SSA particles have residence times of up to many weeks and so spend sufficient time in the atmosphere to be important with regards to atmospheric chemistry, cloud formation, light scattering and other atmospheric processes. Coarse SSA particles have high abundances compared to non-SSA particles, as do accumulation mode SSA particles. However, coarse SSA has residence times of seconds to days, which are much shorter than those of the accumulation mode (Lewis and Schwartz, 2004).

The concentration of SSA particles in the atmosphere is obviously greatest over the oceans. The long residence times of SSA mean that it can be entrained high into the atmosphere, and may be carried over large distances. The direct radiative forcing effect of SSA over the Arabian sea has been reported as $-2\pm1\,\mathrm{Wm^{-2}}$, and the indirect forcing effect as $-7\pm4\,\mathrm{Wm^{-2}}$ (Vinoj and Satheesh, 2004). When compared to the total anthropogenic aerosol forcing in this region ($5.0\pm2.5\,\mathrm{Wm^{-2}}$) this is considerable. Naturally, the forcing effects of SSA are dependent on its particle number concentrations. Figure 1.2 gives an overview of the global concentration of SSA compared to other atmospheric aerosols. While the pure SSA is limited primarily to the southern hemisphere from March to August, the mixture of sulphate and SSA is ubiquitous.

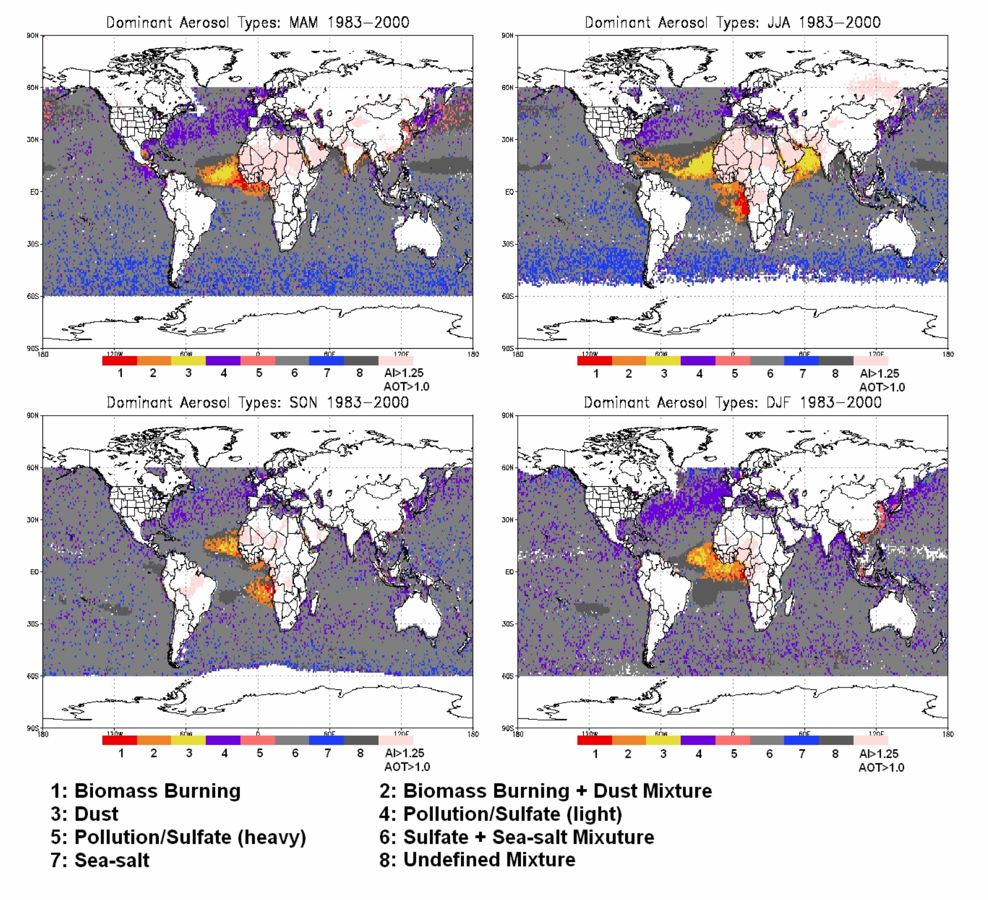

Figure 1.2: Global seasonal maps of dominant aerosol types over the oceans, taken from (Jeong and Li, 2005). MAM refers to the time period from March to May, JJA refers to the period from July to August, SON is September to November and DJF is December to January.

1.4.2 Variation with Relative Humidity

SSA particles are hygroscopic and can therefore readily exchange moisture with the atmosphere. The soluble salts of which SSA is composed have a strong affinity for water, which means that they can facilitate particle growth. The equilibrium radius of an SSA particle is therefore determined by the ambient relative humidity (RH) (Arons and Kientzler, 1954; Salhotra et al., 1987). The typical equilibrium RH of

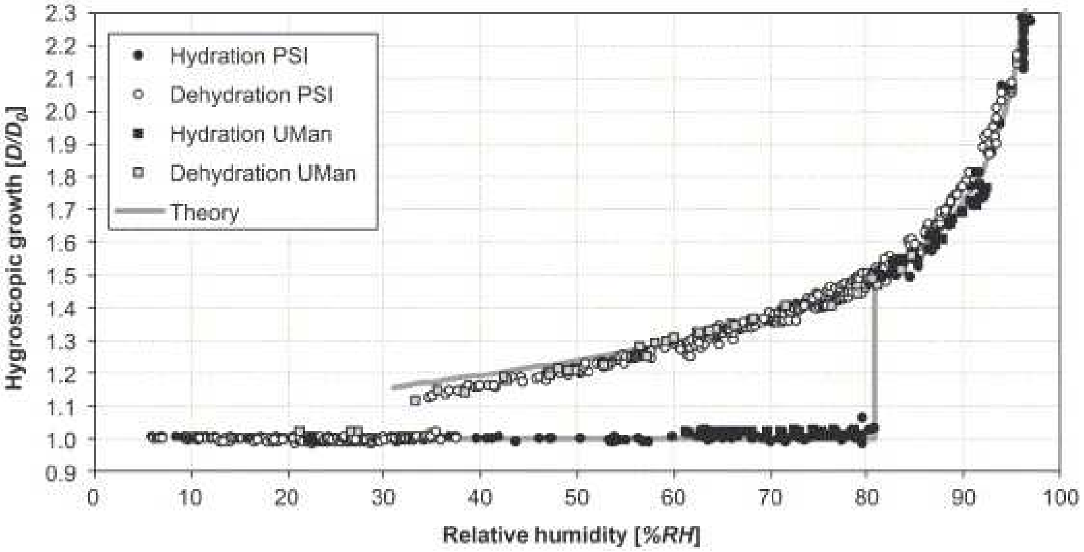

Figure 1.3: Variation of the hygroscopic growth factor (the ratio of the actual particle size to the dry particle size) of an aerosol particle with relative humidity. Graph shows measurements of ammonium sulphate particles from two different instruments as the relative humidity is increased (Sjogren et al., 2007).

an SSA droplet at formation is 98 % for a typical salinity[5] of 35 (Robinson, 1954). Over the first tens of metres above the ocean the RH is typically greater than 75 %, but may fall to below 45 % (Lewis and Schwartz, 2004).

At very low RH, pure salts will exist in dry particle form. As the RH increases, the particles will abruptly take up water at the deliquescence relative humidity (DRH) and become droplets of saturated salt solution (see figure 1.3). However, if the RH is then reduced to below the DRH, the particle will remain as a supersaturated droplet until a lower effluorescence relative humidity (ERH) is reached, at which point the particle spontaneously becomes dry. Additionally, as the droplet

---

[5] Salinity is a dimensionless number based on conductivity, that is approximately equal to the mass ratio of dissolved sea salt per kilogram of seawater. For the majority of the world's oceans, this value is between 33 and 37 (Montgomery, 1958; Millero and Sohn, 1992)

grows, the concentration of salt within the droplet decreases, and this causes the droplet's affinity to water to decrease, thus reducing its growth rate (Hinds, 2001). Sea salt is made up of many compounds and so does not exhibit a sudden change in state. Instead SSA particles exhibit a more gradual change in size as they begin to absorb water or release it to the atmosphere. Nevertheless, this hysteresis behaviour is present in SSA particles as well as particles of the composite salts of SSA (Tang et al., 1997).

A number of different quantities are used to characterise the size of SSA particles. These include the equivalent dry radius (r_{dry}), which can be calculated from the mass of dry sea salt (m_{dry}) within the particle, as well as the density of dry sea salt (ρ_{ss}):

$$r_{\mathrm{dry}} = [3m_{\mathrm{dry}}/(4\pi\rho_{\mathrm{ss}})]^{\frac{1}{3}} \tag{1.11}$$

If the radius of dry particles is known, then the above equation may be used to calculate the dry mass of sea salt in the particle. Ignoring hysteresis effects, the dry mass can then in turn be used to calculate the size of the particle at a specific relative humidity using the following parametrisation:

$$r_{RH} = \left(\frac{3m_{\mathrm{dry}}}{4\pi\rho_{\mathrm{ss}}}\right)^{\frac{1}{3}} \left(\frac{4.0}{3.7}\right) \left(\frac{2.0 - RH}{1.0 - RH}\right)^{\frac{1}{3}} \tag{1.12}$$

which is applicable to all salinities (Lewis and Schwartz, 2006). This parametrisation is physically based and agrees with experimental data to an accuracy of 3 % (Tang et al., 1997).

At RH values between 45 % and 75 %, SSA particles may exist in either liquid droplet or dry salt form. As SSA particles are usually formed as liquid droplets, and the RH rarely drops to below 75 %, it may be assumed that they always exist as liquid solution drops in the first tens of metres above the oceans (Lewis and Schwartz, 2004).

1.4.3 Previous Measurements

The refractive indices of sea salt aerosol have previously been obtained using reflectance and transmission measurements made on bulk samples (Volz, 1972). These were made using pellets of KBr with a layer of powdered sea salt pressed onto the surface, and not using actual aerosol. There is also some ambiguity as to whether or not the samples remained dry during measurement as it was reported both that the surface of the samples remained essentially dry, and that there was evidence of serious deterioration of the samples due to exposure to humidity. Figure 1.4 shows the refractive indices reported by Volz (1972). The peaks at $\sim 1625\,\mathrm{cm}^{-1}$ and $\sim 3430\,\mathrm{cm}^{-1}$ are both attributable to water. The large size of the peak at $\sim 3430\,\mathrm{cm}^{-1}$ suggests a significant amount of water in the sample. The resolution of this data varies over the wavenumber range 250–4000 cm^{-1}, but the average resolution is approximately $87\,\mathrm{cm}^{-1}$.

Detailed measurements of refractive index have been made on bulk solutions of NaCl (Querry et al., 1976; Yunus, 1992; Neto et al., 2004). However, these may not be directly applicable to SSA which contains compounds other than NaCl. Yunus (1992) also made measurements of $MgCl_2$ and Na_2SO_4 solutions. The ions of these solutions are found in abundance in natural seawater. A bulk solution of artificial seawater was also prepared and measured. Yunus (1992) found that the refractive indices obtained for the components of seawater were all smaller than the refractive

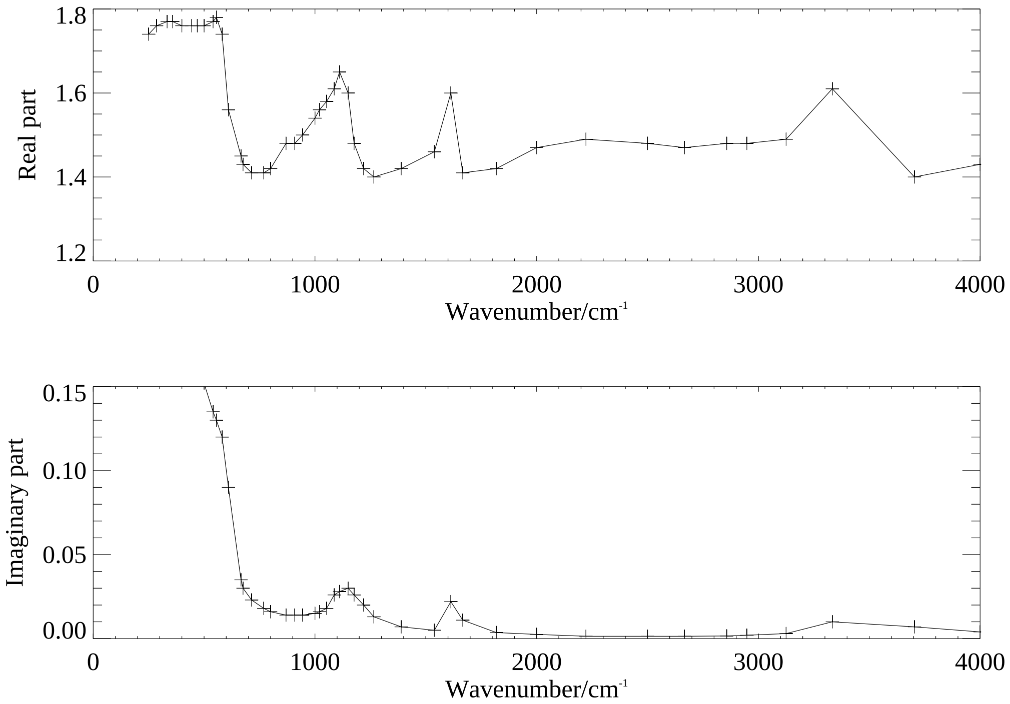

Figure 1.4: Graphs showing the real and imaginary parts of the refractive indices of sea salt as measured by Volz (1972).

indices of both artificial and natural seawater.

Tang et al. (1997) have made measurements on sea salt solution using a single particle levitation technique (Tang and Munkelwitz, 1991). However the solution used was made up of four salts selected to approximate sea salt composition rather than actual sea salt. The particle on which measurements were made was 6–8 μm in diameter when dry, meaning that the particle was significantly larger than accumulation mode aerosol and therefore not necessarily representative of atmospheric SSA. Additionally both the single particle levitation method and the methods employed by Yunus (1992) and Neto et al. (2004) involve measurements made at a single wavelength[6] rather than over a range of wavelengths.

Cziczo and Abbatt (2000) made measurements of the major components of SSA, in aerosol form, over a range of temperatures and humidities. These involved measurements of extinction over the spectral range 500 to 4000 cm^{-1}. However, no measurements were made on actual SSA, and the refractive indices were not retrieved from the data. Therefore the scope remains for more accurate measurements of SSA refractive index spectra.

1.4.4 Volume Mixing Rules

Currently, the refractive indices of wet SSA are calculated using mixing rules. These involve a volume weighting formula that uses the modal radii of wet and dry aerosols to find an average value of the refractive index (Shettle and Fenn, 1979):

$$m_e = \sum_j m_j f_j \tag{1.13}$$

where m_e is the effective refractive index of internally mixed particles, m_j is the refractive index of species j, and f_j is the volume fraction of species j.

While this method may be valid for a mixture of particles in water, it may not hold for solutions of salts such as sodium chloride that readily dissolve in water. These salts dissociate into separate ions on dissolving; for example, sodium chloride dissolves into Na^+ and Cl^- ions. This means that the values of refractive index of SSA currently used in climate and retrieval models may not be physically realistic.

Winter and Chylek (1997) use the refractive index data calculated by Shettle and Fenn (1979) using volume mixing rules to calculate the global planetary clear-sky

---

[6] This is the wavelength of the He-Ne laser used for the experiments i.e. 632.8 nm.

albedo. However, they obtain values for optical depth that are lower than measured values, suggesting that the SSA refractive index values used may be incorrect. Furthermore, no validation or verification of the mixing rules is undertaken either by Shettle and Fenn (1979) or by Winter and Chylek (1997). This suggests that there remains a pressing need for direct measurements of the optical properties of SSA at different RH values in order to quantify and improve on those currently in use.

Advantages of Aerosol Measurements

Previous methods of determining the optical properties of aerosol substances include spectroscopy of bulk samples, individual droplets and thin films. However, thin film techniques introduce the possibility of heterogeneous nucleation and interaction with a substrate. It has been shown by McPheat et al. (2002) that there are significant differences in the extinction spectra of thin films and those of actual aerosol particles of a particular compound. Also, the relative humidity of accumulation mode aerosols will differ to that above a bulk solution due to the Kelvin effect (refer to section 1.3.3). For accurate measurements at differing RH values it is therefore preferable to perform measurements on actual aerosol particles.

Additionally, aerosol particles can be created over the full range of RH values, from $\sim 0\,\%$ to $\sim 100\,\%$. Consequently SSA particles which have a large salt to water ratio may exist. With bulk samples there is an upper limit to this ratio that is determined by the saturation point of the solution. Aerosol particles may exist as solid particles with thin liquid coatings, especially under conditions of low RH. However, the extinction response of such particles could not possibly be modelled by bulk solutions for which there is no equivalent state. Measurements made on actual accumulation mode SSA are therefore likely to be more accurate than those made on bulk solutions.

1.4.5 Current Data

The current sea salt refractive index data is available on the HITRAN data base (Rothman, 2005), as well as on other databases. This consists of the data from the Volz measurements after mixing rules have been applied so that a slightly wet aerosol refractive index is emulated (Shettle and Fenn, 1979). Additionally, Shettle and Fenn (1979) provide refractive indices for dry sea salt that are extended up to 50,000 cm^{-1} (0.2 μm) using data compiled by Dorsey (1940). This data will be used to provide comparison datasets during the following investigation. A summary of the data presented by Shettle and Fenn (1979) is given in table 1.4. However, as the data for wet SSA is calculated using volume mixing rules, equivalent refractive indices at other RH values may be calculated using the same mixing rules.

Modal Radius (μm)	Relative Humidity (%)
0.160	0
0.171	50
0.204	70
0.318	80
0.380	90
0.461	95
0.602	98
0.751	99

Table 1.4: Table giving a summary of data presented by Shettle and Fenn (1979) and available on the HITRAN database. The modal radii are those used in the volume mixing calculations, and the refractive index data is presented over the wavenumber range 250–50,000 cm^{-1}.

1.5 Summary

- Aerosols contribute to the global radiative balance. Detailed knowledge of their optical properties is therefore important in order to quantify this contribution.
- The way in which aerosol particles interact with their environment depends on their optical properties, size and composition.
- Sea salt aerosols are particularly important due to the large source area of the oceans.
- There is a pressing need for new measurements of the refractive indices of SSA since:
    - Previous refractive index measurements were made on bulk material rather than actual accumulation mode aerosol.
    - There is some uncertainty over the possible contamination and degradation of these samples due to exposure to humidity.
    - Currently, the refractive indices of wet aerosols are calculated using volume mixing rules which may not be valid for salt solutions where the salts readily dissociate in water.
    - Volume mixed refractive indices are being used in global climate models without verification or validation, in spite of discrepancies between measured and modelled data.
- Dry measurements of actual SSA particles are required. The accuracy of the volume mixing rules with regards to salt solutions needs to be verified. Further

measurements of wet SSA are required due to possible invalidity of the volume mixing rules with regards to salt solutions.

Chapter 2

Spectroscopy of Aerosols

The optical properties of an aerosol determine the way in which it scatters and absorbs electromagnetic radiation. These may be derived from measurements of the aerosol extinction or transmission. In general, extinction in the mid infra-red region, from ~ 400 to $4000\,\mathrm{cm}^{-3}$, is dominated by absorption, while the extinction in the near infra-red, from ~ 4000 to $8000\,\mathrm{cm}^{-3}$, is dominated by scattering[1]; although the exact relationship is dependent on the particle size distribution. Once the aerosol extinction or transmission spectrum is determined, the complex refractive index of the aerosol can be calculated using scattering and absorption coefficients.

2.1 Fourier Transform Spectroscopy

The transmission spectrum of an aerosol sample may be obtained using Fourier transform spectroscopy. A Fourier transform spectrometer measures an interferogram from light transmitted through a laboratory sample. It is based on the Michel-

---

[1] A notable exception to this trend is carbon.

son interferometer (see figure 2.1). A beam from a collimated source is divided and

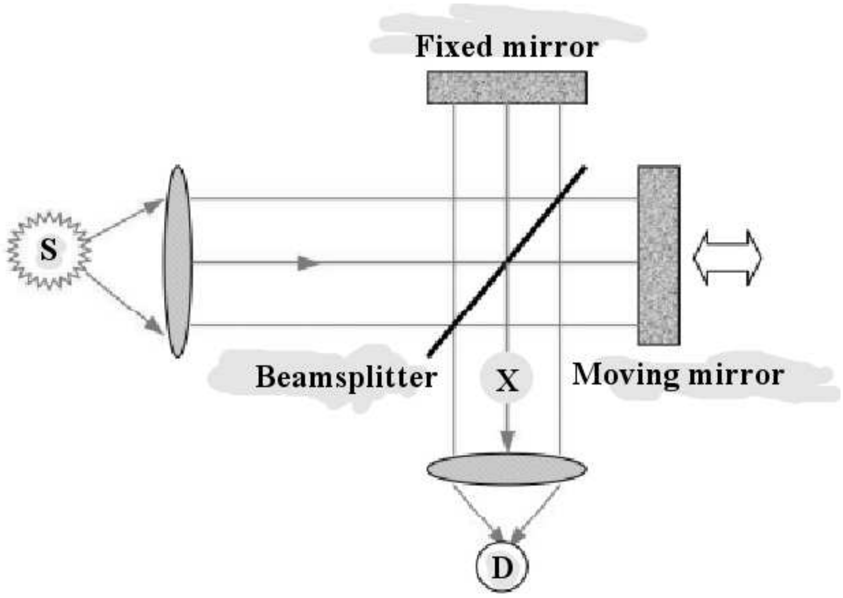

Figure 2.1: Diagram of a typical Fourier transform spectrometer. Here, S indicates the source, X denotes the position of the sample and D is the detector position.

a variable phase delay is introduced to one component of that beam by means of a movable mirror. The two beams are recombined and then split again, with one half returning to the source while the sample to be analysed is exposed to the remaining, reflected beam. At particular frequencies, specific to the measured sample, light will be absorbed and scattered, resulting in a series of peaks and troughs which are unique to the chemical compound measured (Chamberlain, 1979). The intensity of the transmitted radiation is recorded as a function of the mirror displacement. The Fourier transform of this interferogram returns a transmission spectrum in the frequency domain.

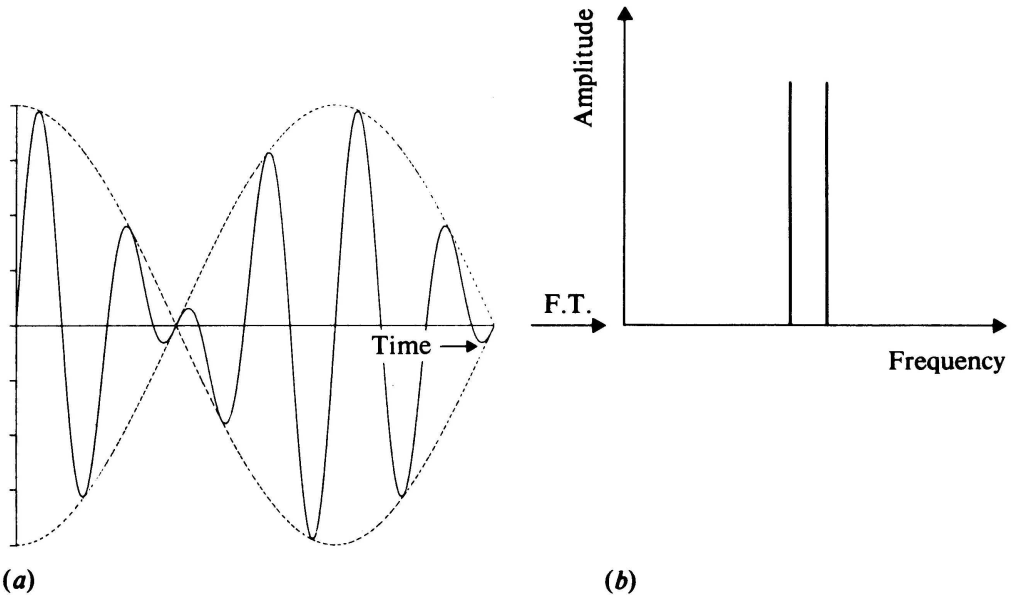

Figure 2.2: Conversion of signal from time domain to frequency domain (Banwell, 1983).

2.1.1 Fourier Transforms

A Fourier transform allows a time-dependent variable to be expressed as a frequency-dependent variable (see figure 2.2). Fourier transforms may be used with both periodic and aperiodic functions. For the function $I(t)$, the Fourier transform may be written as

$$G(\omega) = \int_{-\infty}^{\infty} I(t) \exp^{-i\omega t} \, \mathrm{d}t \tag{2.1}$$

where t is time and ω is angular frequency. In Fourier transform spectroscopy the intensity of transmitted light is measured as a function of the path difference of one of the interfering light beams[2]. Equation 2.1 may therefore be rewritten in terms of path difference, x, rather than time, in which case the measured interferogram is represented by $I(x)$. Rewriting this equation so that it is in terms of frequency, ν,

---

[2] This path difference is equal to twice the mirror displacement.

where $\nu = \frac{\omega}{2\pi}$, gives:

$$T(\nu) = \int_{-\infty}^{\infty} I(x) \exp^{-2\pi i \nu x} \, \mathrm{d}x \tag{2.2}$$

where $T(\nu)$ now gives the transmission as a function of frequency. Similarly, the inverse transformation may be used to convert a function in the frequency domain to one in the path difference domain:

$$I(x) = \int_{-\infty}^{\infty} T(\nu) \exp^{2\pi i \nu x} \, \mathrm{d}\nu \tag{2.3}$$

2.1.2 Resolution

The integral in equation 2.2 assumes a knowledge of x over an infinite range. In reality, the optical path difference of an instrument is finite. This can be represented by multiplying $I(x)$ by a boxcar function, $B(x)$ where $B(x) = 1$ for $0 \leq x \leq$ path difference and $B(x) = 0$ elsewhere. The Fourier transform of this function results in a normalised sinc function (see figure 2.3). Therefore the multiplication of $I(x)$ by the boxcar function is equivalent to the convolution of $F(x)$ with this normalised sinc function. As a result, any lines narrower than the sinc function are broadened and this may result in the loss of spectral information, for example, if a doublet is broadened it may appear as a single broad line in the final spectrum. The instrument resolution is thus limited by the maximum optical path difference, and the two are inversely proportional. The sinc function is known as the instrument line shape (ILS), and may also cause spectral artefacts in the sidelobes of a line, for example transmission values greater than 1.

In order to reduce the magnitude of the sidelobes in the ILS, the measured interferogram may be multiplied by an apodisation function. However, while this

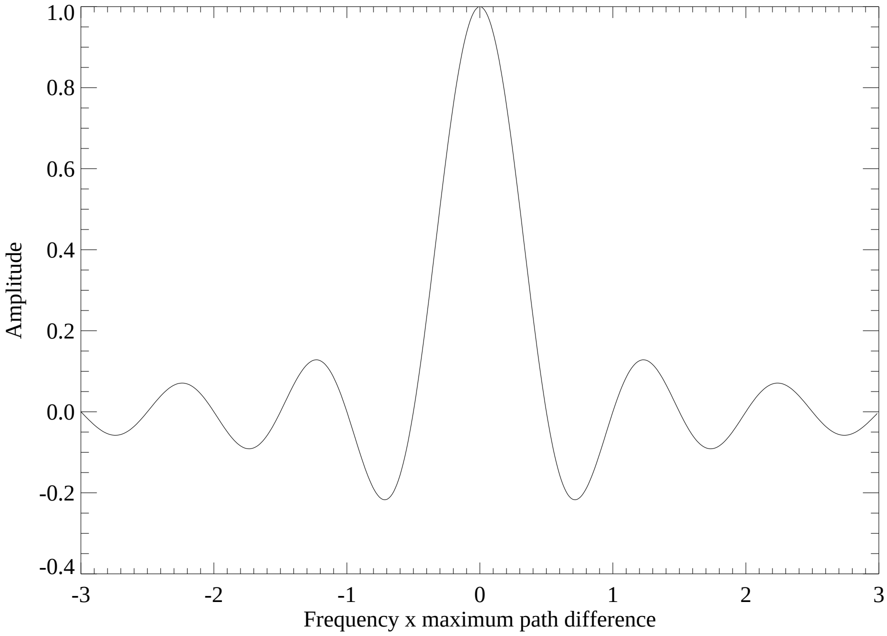

Figure 2.3: The normalised sinc function $sin(2\pi\nu x)/(2\pi\nu x)$.

reduces the ringing in the ILS, it also increases the line width, thereby reducing the instrument resolution further. Norton and Beer (1976) investigated approximately 1150 functions in order to find the optimal compromise between loss of resolution and reduction of the ILS ringing. One of their optimal formulations was the Norton-Beer Strong function, which is used for these studies. While this apodisation function reduces the resolution slightly, a high spectral resolution is not as crucial for aerosol studies as reducing the impact of sidelobes in the ILS, which the chosen apodisation function does well.

2.1.3 Spectral Lines

Real spectral lines extend over a range of frequencies due to various mechanisms[3] (e.g. pressure broadening). These broadened lines can be considered as small packages of slightly different frequencies (Banwell, 1983). The Fourier transform of a broadened line shows a beat pattern resulting from the superimposed waves of the small packages making up the line, as shown in figure 2.4. The signal in the time domain decays as the packages of sine waves become more out of phase with time. Similarly, the amplitude of an interferogram will decrease with increasing path difference of the interfering beams. Hence if the interferogram is measured, equation 2.2 can be used to provide full information on the position, size and width of spectral lines.

2.2 Refractive Index Retrieval

The optical properties of the aerosol can be derived from transmission spectra using a retrieval algorithm. In retrieval theory a forward model, $\mathbf{F}(\mathbf{x})$, is used to relate a state vector, $\mathbf{x}$, consisting of the parameters to be determined, to the measurement vector, $\mathbf{y}$. The retrieval program compares the measurement vector to the output from the forward model (an estimate of the state) and iteratively reduces the differences between the two to a minimum by varying the physical parameters represented in the model. These differences are described by the cost function. A more in-depth explanation of retrieval theory is given in appendix A.

A novel method of refractive index retrieval was developed by Thomas et al.

---

[3] These will not be discussed here but are described at length in many other publications, for example Kuhn (1969); Peach (1981); Lajunen and Peramaki (2005)

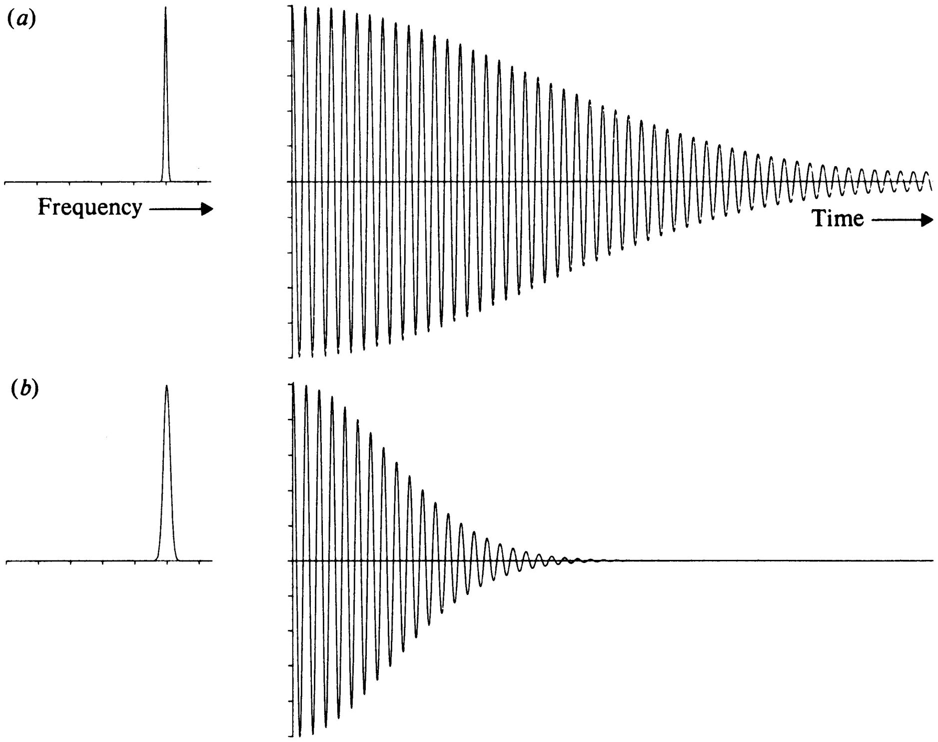

Figure 2.4: Effect of line broadening in frequency domain on time domain signal (Banwell, 1983).

(2004). In this method the molecular absorption of aerosol molecules is modelled using a classical damped harmonic oscillator (CDHO) model. This relies on the fact that dispersive absorption due to an oscillating molecule has a specific peak shape, determined by the fundamental modes of atomic and inter-atomic oscillation within a molecule (Bass, 2003). It produces modelled absorption bands that are very close to observed band shapes, provided the features are symmetric.

For the refractive index retrieval, the CDHO model is combined with a Mie scattering algorithm to provide a forward model that fully describes the spectrum. The final model of the spectrum is fitted to measurements of extinction using a numerical optimal estimation algorithm (the retrieval algorithm). A priori data[4] is used to calculate the initial extinction spectrum for the algorithm. This may be obtained using independent measurements of parameters describing particle number density and particle size distribution. The retrieval algorithm also uses a fixed index point in the visible part of the spectrum to calculate the aerosol extinction. This is the offset value of the real part of the dielectric constant at infinite frequency, ϵ'_∞, such that $\epsilon'_\infty = m^2_\infty$. This is known as Maxwell's relation (Hecht and Zajac, 1980). Away from absorption bands, at large frequencies, m_∞ becomes equal to the real part of the refractive index.

Once the cost function has been minimised, the retrieval algorithm calculates final values for both the refractive index and the parameters describing the particle size distribution.

2.2.1 Classical Damped Harmonic Oscillator Model

The CDHO model evaluates the dielectric spectrum for the aerosol by relating a complex wavelength dependent polarisability ($\alpha_m(\nu) = \alpha'_m(\nu) + i\alpha''_m(\nu)$) to a set of p band parameters (Thomas et al., 2004). These bands are each described by the central wavenumber position of the oscillator ν_j, a width (damping constant) γ_j, and the band intensity S_j.

The complex polarisability is given by the following equations (Bertie et al., 1994):

$$\alpha'_m(\nu) = \frac{3N_A(\epsilon_\infty - 1)}{4\pi N(\epsilon_\infty + 2)} + \frac{N_A}{4\pi^2 c^2} \sum_j \frac{(\mu_j^2/3)(\nu_j^2 - \nu)}{(\nu_j^2 - \nu^2)^2 - \gamma_j^2 \nu^2} \tag{2.4}$$

---

[4] The a priori state vector contains all prior information known about the band parameters and particle size distribution before measurement.

$$\alpha''_m(\nu) = \frac{N_A}{4\pi^2 c^2} \sum_j \frac{(\mu_j^2/3)\gamma_j \nu}{(\nu_j^2 - \nu^2) - \gamma_j^2 \nu^2} \tag{2.5}$$

where N_A is Avogadro's number, μ_j is the derivative of the dipole moment with respect to the normal coordinate for the jth band, N is the particle number density and ϵ_∞ is the value of the dielectric constant at infinite frequency (or zero wavelength).

In order to find the complex dielectric spectrum, we employ the Lorentz-Lorenz relation (Dignam, 1988):

$$\frac{\epsilon(\nu) - 1}{\epsilon(\nu) + 2} = \frac{m(\nu)^2 - 1}{m(\nu)^2 + 2} = \frac{4}{3}\pi N \alpha(\nu) \tag{2.6}$$

where ϵ, m and α are all complex quantities to account for the absorption features in the spectrum, represented by the imaginary parts. The wavenumber dependent complex forms of the refractive index and dielectric constant can therefore be written in the following form:

$$m(\nu) = n(\nu) + ik(\nu) \tag{2.7}$$

$$\epsilon(\nu) = \epsilon'(\nu) + i\epsilon''(\nu) \tag{2.8}$$

Using the Lorentz-Lorenz formula it can be shown that:

$$\epsilon'(\nu) = \epsilon_\infty + \sum_j \frac{S_j(\nu_j^2 - \nu^2)}{(\nu_j^2 - \nu^2)^2 + \gamma_j^2 \nu^2} \tag{2.9}$$

$$\epsilon''(\nu) = \sum_j \frac{S_j \gamma_j \nu}{(\nu_j^2 - \nu^2)^2 + \gamma_j^2 \nu^2} \tag{2.10}$$

where the dipole moment derivative μ_j is replaced by the band intensity S_j with a slight local field correction[5] (Bass, 2003). It can also be shown from equation 2.6 and Maxwell's relation that the complex refractive indices are given by:

$$n(\nu) = \left(\frac{\sqrt{\epsilon'(\nu)^2 + \epsilon''(\nu)^2} + \epsilon'(\nu)}{2} \right)^{\frac{1}{2}} \tag{2.11}$$

$$k(\nu) = \left(\frac{\sqrt{\epsilon'(\nu)^2 - \epsilon''(\nu)^2} + \epsilon'(\nu)}{2} \right)^{\frac{1}{2}} \tag{2.12}$$

where $n(\nu)$ is the real part of the refractive index and $k(\nu)$ is the imaginary part. Similarly, the complex polarisability can now also be written in terms of $\epsilon(\nu)$, N_A and N alone:

$$\alpha'(\nu) = \frac{3N_A}{4\pi N} \frac{(\epsilon'(\nu) - 1)(\epsilon'(\nu) + 2) + \epsilon''(\nu)^2}{(\epsilon'(\nu) + 2)^2 + \epsilon''(\nu)^2} \tag{2.13}$$

$$\alpha''(\nu) = \frac{9N_A}{4\pi N} \frac{\epsilon''(\nu)}{(\epsilon'(\nu) + 2)^2 + \epsilon''(\nu)^2} \tag{2.14}$$

2.2.2 Mie Scattering Theory

Mie theory (Mie, 1908) is a special solution of Maxwell's equations for a homogeneous sphere, and is usually applied when considering the scattering of electromagnetic radiation from particles of a similar size to the wavelength of the incoming radiation, for example with aerosol particles. It describes the diffraction of a monochromatic plane wave by a homogeneous sphere in a homogeneous medium. It also applies to diffraction by any number of randomly distributed spheres of the same composition and diameter that are separated by distances greater than the wavelength of the

---

[5] In a dense optical medium, such as a solid, it is necessary to consider the response of individual atoms to the local field when calculating the dielectric constant. This may be different to the external field as dipoles themselves generate electric fields that are experienced by all other dipoles (Fox, 2001).

incident radiation.

In reality, dry SSA particles are not spherical but, under low RH conditions, crystallise into cubic shapes. However, Chamaillard et al. (2006) have shown that for particles with radius $< 0.5\,\mu$m, Mie theory describing the interactions of spherical particles with light gives results that are approximately equal to the Discrete Dipole Approximation (DDA) model, which describes the interaction of cubic SSA particles with light.

From Mie theory, the ratio of the amount of energy intercepted by a particle to the amount of energy incident on the particle is given by the extinction efficiency, Q_{ext}:

$$Q_{ext}(m,\alpha) = \frac{2}{\alpha^2}\sum_{l=1}^{\infty}(2l+1)Re[a_l + b_l] \tag{2.15}$$

where

$$a_l = \frac{\alpha\psi_l'(\alpha m)\psi_l(\alpha) - \alpha m\psi_l'(\alpha)\psi_l(\alpha m)}{\alpha\psi_l'(\alpha m)\zeta_l(\alpha) - \alpha m\zeta_l'(\alpha)\psi_l(\alpha m)} \tag{2.16}$$

$$b_l = \frac{\alpha m\psi_l'(\alpha m)\psi_l(\alpha) - \alpha\psi_l'(\alpha)\psi_l(\alpha m)}{\alpha m\psi_l'(\alpha m)\zeta_l(\alpha) - \alpha\zeta_l'(\alpha)\psi_l(\alpha m)} \tag{2.17}$$

Here

$$\psi_l(\rho) = \sqrt{(}\frac{\pi\rho}{2})J_{l+\frac{1}{2}(\rho)} \tag{2.18}$$

$$\zeta_l(\rho) = \sqrt{\frac{\pi\rho}{2}}H_{l+\frac{1}{2}(\rho)} \tag{2.19}$$

where $J_{l+\frac{1}{2}(\rho)}$ are the Bessel functions and $H_{l+\frac{1}{2}(\rho)}$ is one of the Hankel functions (for further details see Born and Wolf (2003)). The volume extinction coefficient is then given by:

$$\beta_{ext}(\nu) = \pi\int_0^{\infty} r^2 Q_{ext}(r,\nu,m(\nu))n(r)\,\mathrm{d}r \tag{2.20}$$

where r is the radius of a spherical particle and m is the complex refractive index. Assuming a log-normal distribution, equation 2.20 becomes:

$$\beta_{ext}(\nu) = \frac{N_0}{\sigma}\sqrt{\frac{\pi}{2}}\int_0^\infty rQ_{ext}(r,\nu,m(\nu))\exp\left[-\frac{(\ln r - \ln r_m)^2}{2\sigma^2}\right]\,\mathrm{d}r \tag{2.21}$$

where σ is the width of the particle size distribution, r_m is the median particle radius and N_0 is the total particle number density.

2.2.3 Size Measurements

It is important to make independent measurements of the aerosol particle size and number density. This data provides a priori information for the refractive index retrieval. Additionally, the aerosol particles are modelled using Mie theory which makes a number of assumptions. It is assumed that the particles are spherical, that the size distribution is log-normal, that only single-scattering occurs and that scattering from these individual particles occurs in isolation from other particles. It is also assumed that the particles and the medium in which they are carried are homogeneous, and that all scattering is elastic. While it has been shown by Chamaillard et al. (2006) that Mie theory may be applied to small cubic particles to give results that are approximately equal to the actual scattering from these particles, the combined effect of the approximations and assumptions may significantly affect the final model. Independent verification of the Mie calculations is therefore prudent. Measurements of particle size and number density would provide this independent validation of the models used.

2.3 Summary

- Fourier transform spectroscopy may be used to measure the intensity of radiation transmitted by an aerosol. The Fourier transform of the measured interferogram gives the aerosol transmission spectrum as a function of frequency.

- A retrieval algorithm can be used to obtain refractive index from transmission spectra using a classical damped harmonic oscillator model and Mie theory.

- The CDHO model provides the best estimate of the shape of the aerosol absorption bands using a priori information. Mie theory describes scattering from homogeneous spheres and is used to calculate a modelled extinction spectrum using the a priori information and information from the CDHO model.

- Wet SSA particles may be considered to be spherical. Dry SSA particles are cubic. However, the light interaction of cubic particles with radius $< 0.5\,\mu$m may be approximated by Mie theory.

- A numerical optimal estimation algorithm is used to fit modelled data to measured values and the refractive index is calculated from the final spectrum obtained.

- Measurements of particle size and number density provide a priori information for the retrieval and independent validation of the Mie calculations.

Chapter 3

Experimental Design

In order to determine the optical properties of SSA, as outlined in chapter 1, it was necessary to design an experiment to obtain measurements of the aerosol optical transmission, as well as the particle size and number density. The experiment would involve four main stages (see figure 3.1). First it would be necessary to produce a sea salt aerosol of a size representative of tropospheric SSA, and of a sufficient

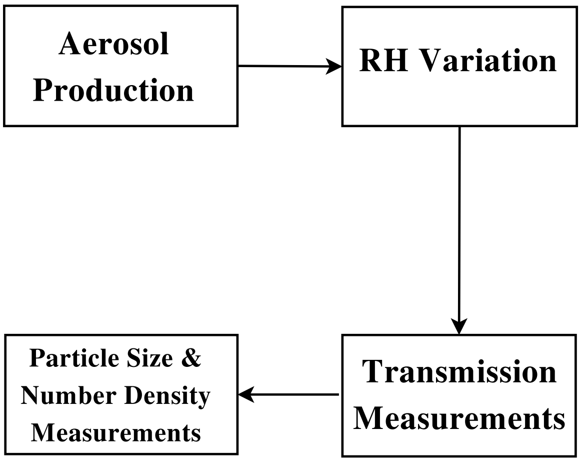

Figure 3.1: Outline of the different stages required to complete aerosol measurements for refractive index retrieval.

number density to ensure adequate light extinction for a reasonable signal to noise level in the measurements. The aerosol would need to be of a relatively consistent size distribution and number density in order to ensure accurate measurements over a range of wavenumbers. Next, a method of varying the RH of the SSA particles would be required so that measurements of wet aerosol could be made. The aerosol particles would also need sufficient time to equilibrate to a new RH before transmission measurements took place. These would need to be taken in a fixed volume using a Fourier transform spectrometer and detector with sufficient resolution to at least match the resolution of previous measurements. A method of monitoring the RH and temperature of aerosol being measured would be advantageous in order to characterise the SSA particles and determine the likelihood of thermophoretic effects. Finally a method of measuring the aerosol particle size distribution and number density would also be required. It would also be important to find a method of carrying the aerosol particles through the experiment and evacuating them safely without compromising any measurements made.

Each of these four stages would involve the acquisition, development or modification of a number of different instruments. An overview of the instruments chosen, their technical specifications and the experimental methods employed at these stages is given below.

3.0.1 Aerosol Generation

A constant, reproduceable aerosol was required, of a size representative of atmospheric aerosol. This is $0.1\,\mu\text{m} < \text{radius} < 1.0\,\mu\text{m}$ in the accumulation mode and radius $> 1.0\,\mu\text{m}$ for coarse particles. As fine particles dominate in the atmosphere

(Hinds, 1982) the accumulation mode was preferable.

Aerosols were required at varying relative humidity values. The RH can be varied by the addition of water to a dry aerosol using a heated water bath. Previous methods of producing dry aerosol substances have included dry dispersion of ground solids (Peters and Grainger, 2004), and the drying of wet aerosols by diffusion (Blackford and Simons, 1986). The dry dispersion method proved unreliable due to electrostatic charging of the aerosol during dispersion. This led to a significant loss in aerosol number density before possible measurement of variation of RH. The second method was therefore chosen.

It was also important to generate an appropriate number density of aerosol particles in order to obtain satisfactory transmission spectra. This was estimated using Mie theory to calculate the scattering parameters for sea salt aerosol at $0\,\%$ RH in the accumulation mode, assuming a lognormal distribution of particles. Extinction data for the sea salt aerosol was taken from the OPAC[1] database (Hess et al., 1998) and used to calculate the volume extinction coefficient of the aerosol. This, in turn, was used to find transmission, as outlined in the previous chapter.

Various plots of transmission were produced for dry sea salt aerosol, assuming a mean particle radius of approximately $0.2\,\mu$m. From these plots it was clear that, in order to reduce the transmission by up to $70\,\%$ at infra-red wavelengths and thereby produce a suitable spectrum for refractive index retrieval, a number density of approximately $1 \times 10^6\,\mathrm{cm}^{-3}$ was required (see figure 3.2). There are a number of possible instruments that may be used to produce an aerosol. The different types of instrument were investigated to determine if the required particle number density was obtainable. Many of these instruments involved the same basic technology, and

---

[1] Optical Properties of Aerosols and Clouds

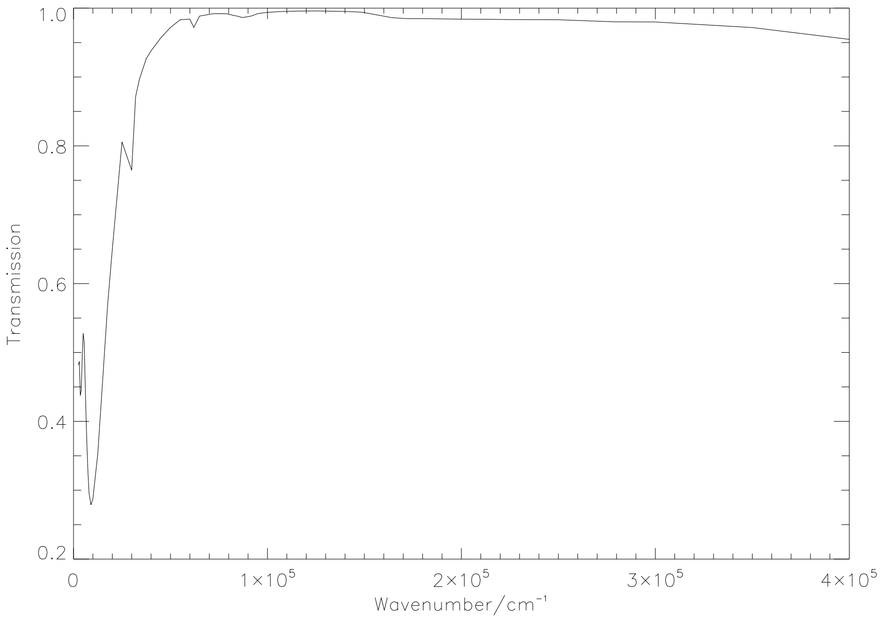

Figure 3.2: Modelled transmission spectrum of dry sea salt aerosol with a particle number density of approximately 10^6 particles cm^{-3}. Spectrum produced using extinction data from the OPAC database.

selected examples of each of the different designs are outlined below.

Simple Atomising Device

Bernoulli's principle states that fast-flowing fluids exert less pressure than slow-moving fluids (White, 2003). This is the concept that governs the basic atomising device shown in figure 3.3. In this apparatus a liquid solution is fed through a tube with a narrow nozzle at the end. Air is blown over the opening of the nozzle at high speed, lowering the pressure at this opening. The reduced pressure draws the liquid out of the tube and it is dispersed as a fine aerosol mist. A steel plate positioned behind the hypodermic needle acts as an impactor, removing larger particles which then slide to the bottom of the vessel. This excess solution is then removed by

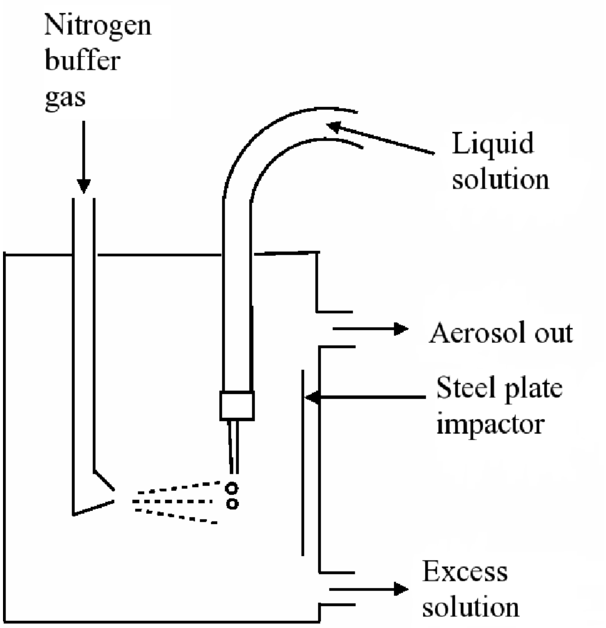

Figure 3.3: Diagram of a simple nebulising apparatus.

a peristaltic pump and recirculated. The aerosol leaves at the top of the unit and passes through a reservoir to further ensure that all larger particles may settle out. A simple atomising device constructed by the Department of Chemistry at Cambridge University (Brabham, 2004) produces particles of size between approximately 120 nm to 150 nm, depending on the molarity of the solution used, and a maximum number density of approximately 10^5 particles cm^{-3}.

TSI Constant Output Atomiser

This is an example of a typical atomiser manufactured specifically for research industries. The TSI atomiser generates aerosols from solutions or suspensions. The average size of particles generated is approximately 0.3 μm, and the device can provide a particle number density of approximately 2×10^6 cm^{-3}. A cut-away schematic

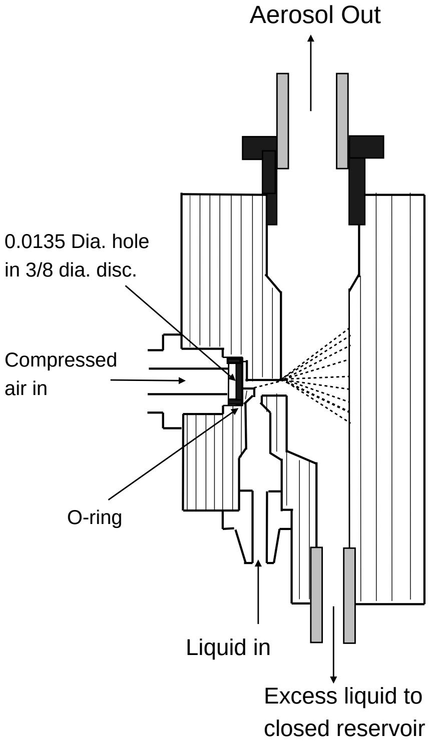

Figure 3.4: Schematic of TSI Atomiser assembly block.

of the atomising system is shown in figure 3.4. Fluid is drawn in through the base of the unit from a supply bottle. Compressed air is forced through a small hole to form a high velocity jet that runs across the path of the fluid, causing it to atomise. Larger particles are removed by impaction on the wall opposite the jet. Excess liquid then drains into a reservoir and may be recirculated back into the supply bottle. The aerosol leaves the unit through an outlet at the top.

OMRON NE-U17 Nebuliser

This is an example of a typical ultrasonic medical nebuliser. Ultrasonic vibrations are used to disperse a liquid solution and this is carried out of the instrument on a

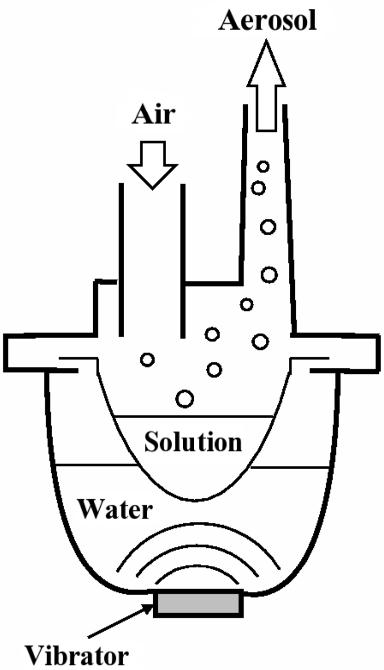

Figure 3.5: Nebulisation chamber of the Omron U17 medical nebuliser.

buffer flow of air. This is shown more clearly in figure 3.5.

The nebulising chamber consists of a water tank, at the bottom of which sits a vibrator. The fluid to be nebulised is placed in a thin plastic cup which rests in the water. Ultrasonic vibrations transmitted through the water to the plastic cup nebulise the liquid and a flow of air over the chamber carries the resulting aerosol out of the unit.

The nebuliser may be run continuously for up to 72 hours, and also allows for the use of buffer gases other than air, for example, nitrogen. The instrument has ten different nebulisation rate settings that are determined by the frequency of the ultrasonic vibrations. Tests were conducted on the unit to provide independent verification of the instrument performance.

OMRON NE-U17 Performance Tests

A test unit was set up at AOPP with ambient air input via the inbuilt air filter. The output was connected first to an API Aerosizer instrument to measure particle size, and then to a GRIMM CPC instrument in order to measure particle number density. Further information on these instruments is given later in this chapter.

Samples of distilled water were nebulised using the OMRON device. Measurements were taken at various different settings of flow rate and nebulisation rate in order to assess the effect on particle size and number density.

OMRON Nebuliser Test Results

The maximum number density of particles recorded by the CPC instruments was $3.37\,\mathrm{x}\,10^6$ particles cm^{-3}. The average particle size obtained at differing nebuliser settings is shown in table 3.1.

Nebulisation Setting (1–10 increasing rate)	Air Flow Volume (1–10 increasing volume)	Average Particle Size (μm)
1	10	1.52
1	1	1.69
5	1	1.69
10	1	1.84

Table 3.1: Table showing the variation of particle size with nebuliser settings

From table 3.1 it is clear that, at a constant nebulisation rate, the average particle size increases as the air flow volume is decreased. When the air flow volume is constant, the average particle size increases with nebulisation rate. Thus the largest particles are produced when the nebulisation rate is at its highest setting, and when the air flow volume is at a minimum.

However, as the particle size increased, the sigma value of the particle size distribution decreased. This would reduce the amount of absorption by the aerosol at a particular number density. Nevertheless, the data from the aerosizer and CPC suggest that a maximum absorption of ~ 75 % would be possible with aerosol produced using the OMRON nebuliser. This is well over the absorption required for adequate transmission spectra, implying that the nebuliser is a viable instrument for use in any subsequent sea salt aerosol experiments.

Summary

Model	Wet Size (μm)	Dry Size (μm)	Flow Rate (l / min)	Number Density (x 10^6 cm^{-3})
Dispersion Method - Airblast Type				
Collision	1.9–2.0	1.0–1.1	2.7	1.60–1.80
	2.5–3.0	1.3–1.6	2.0	0.53–0.92
DeVilbiss D-40	2.8	1.5	21.0	0.89
	3.2	1.7	16.0	0.69
	4.2	2.2	12.0	0.35
DeVilbiss D-45	3.4–4.0	1.8–2.1	9.4–14.0	0.58–0.96
Lovelace	2.6–5.8	1.4–3.0	1.5–2.3	0.34–2.50
Retec X-70/N	3.2–5.7	1.7–3.0	5.0–9.7	0.41–2.30
TSI Atomiser	0.4	0.2	3.0–3.2	2.0
Dispersion Method - Ultrasonic				
Mistogen	6.5	3.4	24.7	0.37
Monaghan 650	5.1–5.2	2.7	8.0	0.20–0.58
OMRON NE-U17	1.0–8.0	0.1–1.0	max 17.0	3.4

Table 3.2: Table showing the properties of various nebulisers.

The properties of all nebulisers investigated are summarised in table 3.2. In addition to the factors discussed at the beginning of section 3.1.1, cost was also important in the selection of an appropriate method of aerosol dispersal. The TSI atomiser and the OMRON U17 nebuliser are both capable of producing aerosols of a size representative of accumulation mode aerosol. These instruments are also capable of providing a particle number density that is adequate for suitable transmission spectra. However, the TSI atomiser is far more costly, both to purchase and maintain. This meant that the OMRON U17 instrument was more attractive. In-house testing of the OMRON nebuliser, confirmed that the instrument would provide a constant, replicable particle size distribution and number density that was within required parameters, and so this was the instrument chosen to generate the wet aerosol for all experiments.

The nebuliser inlet and outlet were adapted to take specially modified swagelok fittings. This would allow a sealed interface with 3/8" PFA (perfluoroalkoxy) tubing to carry the aerosol through the experiment. This was selected due to its non-reactivity, flexibility, resistance to both high and low temperatures[2] and low coefficient of friction, which means that contaminants and aerosol particles are less likely to become attached to the walls of the tubing. Nitrogen was selected as the buffer gas, with mass flow controllers to regulate the flow rates.

3.0.2 Diffusion Dryers

In order to avoid the hysteresis effects associated with particle growth due to increased relative humidity, it would be necessary to produce a dry aerosol which could then be rehydrated to a controlled humidity, following one specific branch of the hysteresis curve, by the introduction of water vapour. Diffusion dryers (Black-

---

[2] Low temperature embrittlement occurs at $-196\,^{\circ}\mathrm{C}$ and the melting point is approximately $580\,^{\circ}\mathrm{C}$.

ford and Simons, 1986) were therefore required to dry the wet aerosol produced by the nebuliser. A diffusion dryer is a device that removes water by means of diffusion into beaded silica gel.

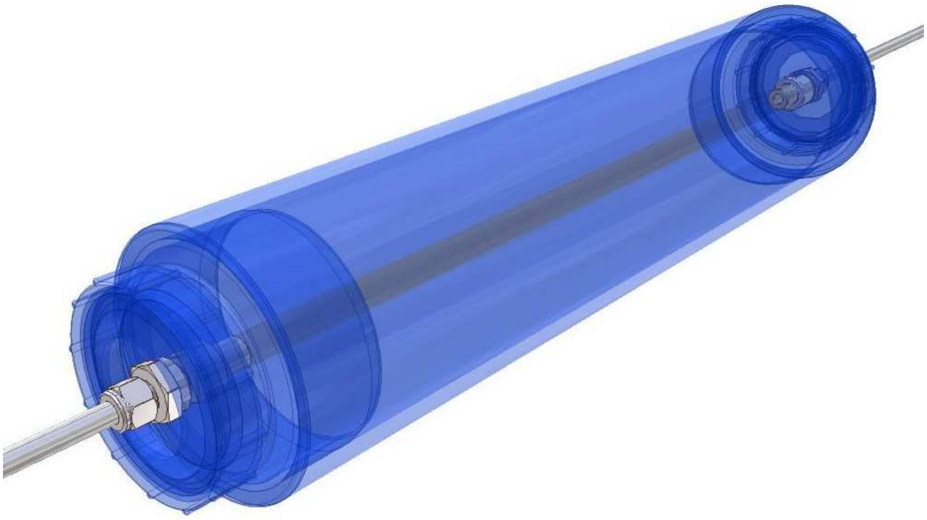

Figure 3.6: Diffusion Dryer

The aerosol enters the diffusion dryer through stainless steel mesh tubing running through its centre (see figure 3.6). The desiccating effect of the silica gel surrounding the mesh tube causes water to diffuse from the aerosol particles to the silica, where it is absorbed and collected. The aerosol then passes out of the dryer. After prolonged use the silica becomes saturated and no longer removes water vapour. It is therefore important to replenish the silica regularly to avoid loss of efficiency of the dryers.

The residence time required for an aerosol to equilibrate to surrounding conditions is of the order of 10 s (Baron and Willeke, 2001). In order to ensure that the aerosol produced was as dry as possible two diffusion dyers were designed and manufactured of length 40 cm and mesh pipe diameter approximately 2 cm. At a maximum flow rate of $\sim 250\,\text{sccm}$[3] this would result in a minimum residence time of approximately one minute. This is more than sufficient to allow the aerosol to dry before leaving the second dryer. Figure 3.6 gives the exact finished design of the dryers used.

The dryers were constructed from 10 cm diameter soil pipe with end caps that included o-ring seals and screw caps. Suitable fittings were fashioned to slot into the central mesh tube and connect it to 3/8" Swagelok bulkhead fittings so that the dryers could be connected to 3/8" PFA tubing. A detailed breakdown of the endcaps and fittings is shown in figure 3.7.

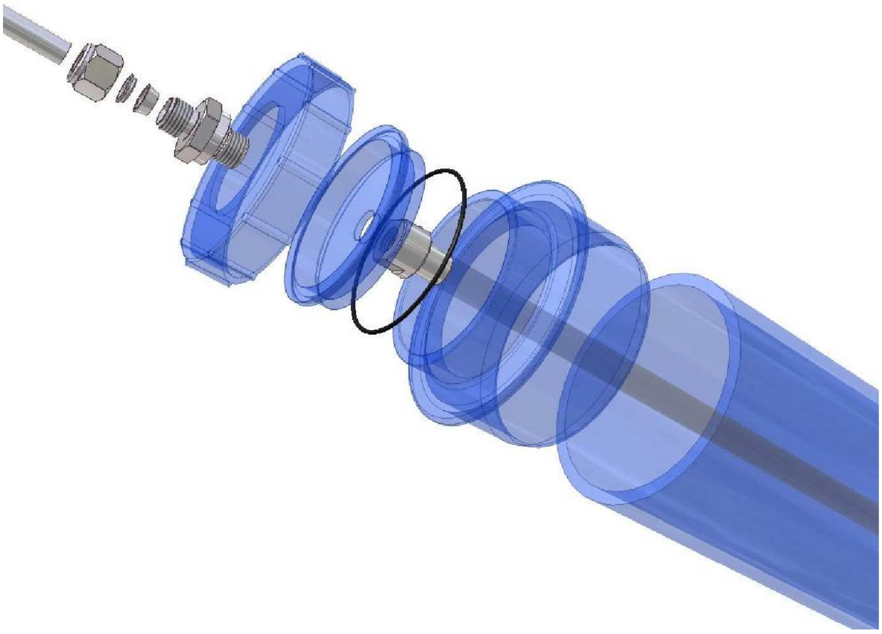

Figure 3.7: Schematic of diffusion dryer, end caps and fittings.

The space between the mesh tubing and outer pipe was filled with 2–5 mm orange

---

[3] This refers to standard cubic centimetres a minute and will be the standard unit used for flow rate in this experiment.

to green self-indicating beaded silica gel[4]. This was chosen over the more common blue to pink cobalt chloride based self-indicating silica as this is now classed as toxic and therefore an additional hazard in any experiment. Colour changes of the silica could be observed through small plastic windows in the endcaps.

Additionally, the dryers were flushed with dry nitrogen gas and pressure tested to 1 bar before use. The fittings were plugged with bungs during transport and storage of the dryers to minimise exposure of the silica to moisture. Measurements during the first phase of experiments showed that the dryers could provide a dried aerosol with RH down to 0.4 %.

3.1 RH Variation

After the aerosol was dried, the aerosol RH would be varied by the introduction of water vapour from a heated bath. The ratio of the gas flows from the nebuliser and the water bath could be varied to provide a range of RH values for the final aerosol. As the water vapour was added to the aerosol flow, the particles would start to grow and the heaviest of these would begin to settle out. It was important that this process should take place before transmission measurements were made, as a stable aerosol was required for consistent, accurate and repeatable measurements. A conditioning vessel was therefore required to allow for gravitational settling and growth of the aerosol particles to occur before measurement.

---

[4] supplied by GeeJay Chemicals (GeeJay Chemicals, 2005)

3.1.1 Conditioner

The residence time required for the aerosol to equilibrate to surroundings due to hygroscopic growth is of the order of 10 s (Baron and Willeke, 2001). However, relaxation times due to gravitational settling must also be considered.

The relaxation time, T_s, is given by Stoke's law, which was described in section 1.3.1:

$$T_s = \frac{2a^2}{9v} \mid 1 - \rho/\rho_0 \mid \tag{3.1}$$

For accumulation mode aerosol particles with a maximum flow rate, v, of 500 sccm and density, ρ, of 2.17 kgm^{-3} carried in nitrogen of density, ρ_0, 1.25 kgm^{-3}, the maximum relaxation time is approximately 0.175 μs. For a salt particle of diameter 1.0 μm, the settling velocity, given by equation 1.8, is approximately 97 cm h^{-1}. If the conditioning vessel is cylindrical with a diameter of 10 cm and the inlet and outlet pipes are approximately 1 cm in diameter and positioned at the centre of each of the end faces, then the time taken for the aerosol particles to settle out will be approximately 3.75 minutes. This would mean that the minimum volume of the conditioning vessel should be approximately 2 litres. Therefore, to allow for a reasonable margin of error, a 2.75 litre glass conditioning vessel was designed and manufactured with two inlets and one outlet (see figure 3.8). This allows for the addition of water vapour through a separate inlet so that mixing and hygroscopic growth can occur within the vessel. The outlet consists of a short tube at the upper left hand wall of the vessel to ensure that none of the large particles that have settled at the bottom of the vessel may leave. Greaseless PTFE (polytetrafluoroethylene) o-ring ball joints connected to swagelok fittings link the conditioner to the PFA tubing carrying the aerosol.

Figure 3.8: Conditioning vessel containing aerosol

At a maximum flow rate of 500 sccm, the vessel gives a residence time of approximately 5.5 minutes, and this is more than sufficient to allow the aerosol to equilibrate before measurement. Glass was chosen for the vessel as this would allow the flow of aerosol to be visible through the walls. In addition, the conditioner was designed and built with a double wall. A separate inlet and outlet in the outer wall resulted in a jacket which could be used to introduce a fluid at a fixed temperature should low temperature measurements be required, although this is beyond the scope of the current measurements. However, this double wall would insulate the aerosol from external temperatures while it was settling into an equilibrium state.

A Honeywell humidity and temperature sensor was used to monitor the RH of the aerosol particles. This was mounted at the exit of the conditioner, attached to the upper part of the glass fitting to avoid saturation by any settling aerosol particles.

3.2 Transmission Measurements

After the aerosol has been brought up to the required RH, the transmission measurements can be made. The Molecular Spectroscopy Facility (MSF) at the Rutherford Appleton Laboratory (RAL) has been used to make transmission measurements of aerosols in the past. They have developed a cell designed to hold the aerosol in the sample compartment of a Bruker Fourier transform spectrometer to allow transmission measurements to be made. All experimental work was therefore undertaken at this facility.

3.2.1 Bruker IFS 66V/S Spectrometer

The IFS 66V/S is a Fourier transform spectrometer with a spectral range that goes from the far-infra-red to the near-ultraviolet (approximately 370–7500 cm^{-1}). A basic schematic of the spectrometer is shown in figure 3.9. The optical configuration is a slight variation of that described in section 2.1.

The source is a silicon carbide globar which is collimated using a parabolic mirror. This is highly stable with an intensity drift of less than 1 % over 24 hours. The spectrometer uses a germanium coated KBr beamsplitter with a spectral range of 500–13,000 cm^{-1}. A deuterium lanthanum triglycero sulphide (DLaTGS) detector is incorporated in the Bruker for room temperature measurements. This has a highly linear response to photon detection rate over the range 350–8000 cm^{-1}, and an effective resolution of 4 cm^{-1}. The DLaTGS detector can be operated at higher spectral resolution. However, it has a relatively slow response compared to some other detectors. Therefore, in order to produce good quality measurements in a reasonable time frame, and since no higher resolution spectral structure is expected

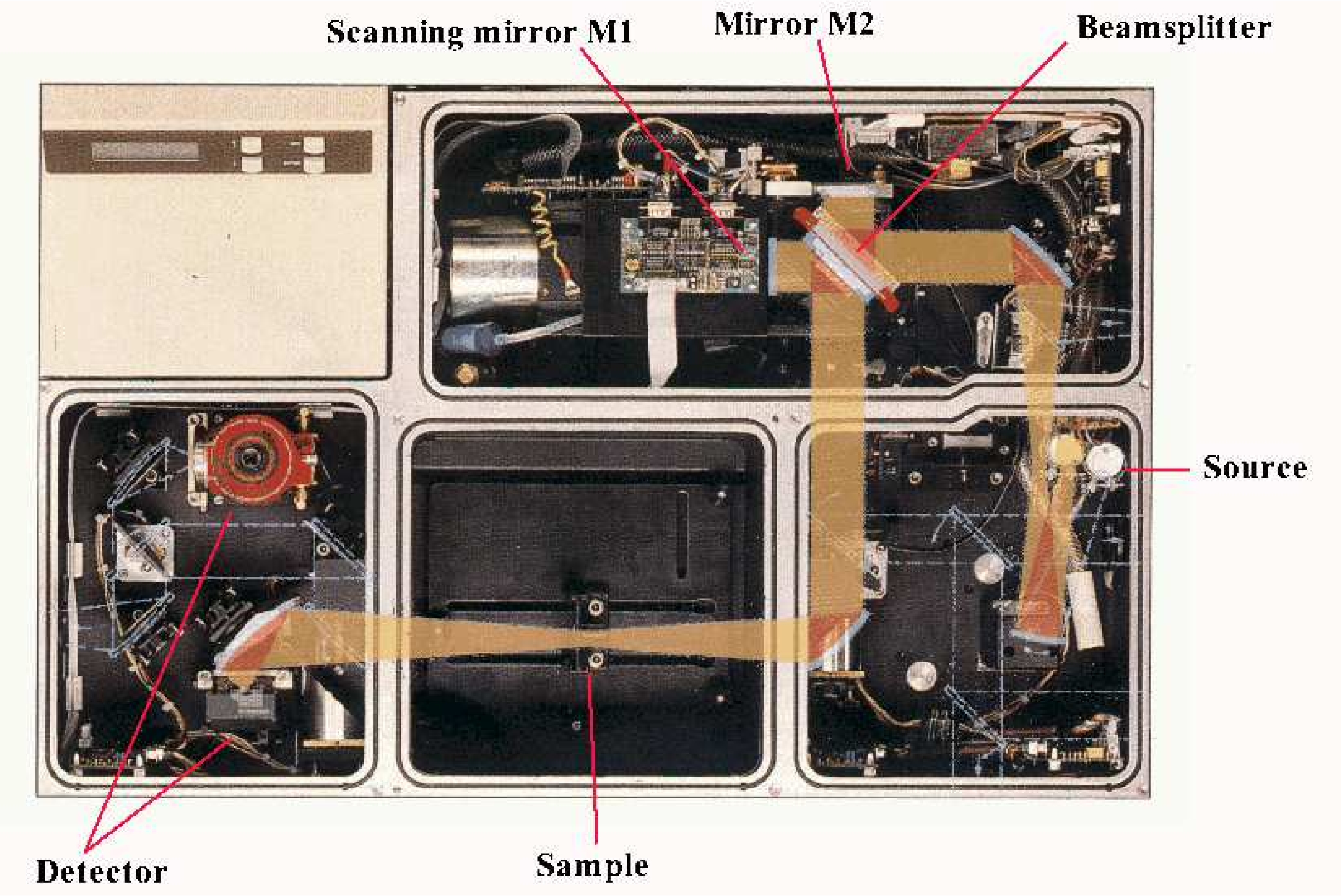

Figure 3.9: Schematic of the Bruker IFS 66v Fourier transform spectrometer, taken from Thomsen (2008).

with aerosol measurements, a resolution of 4 cm^{-1} is sufficient. The optics and the sample chamber of the spectrometer are evacuated before measurement to avoid contaminants.

3.2.2 MSF Aerosol Cell

The aerosol cell is 26.3 cm long with an internal diameter of 3.4 cm. It is a double-walled, stainless steel cell with an internal volume of approximately 145 cm^3 (see figure 3.10). The input and output ports are located approximately 12.0 cm apart on one side of the cell. It is mounted horizontally inside the evacuated sample compartment of the spectrometer with the beam forming a focal point in the middle of the cell.

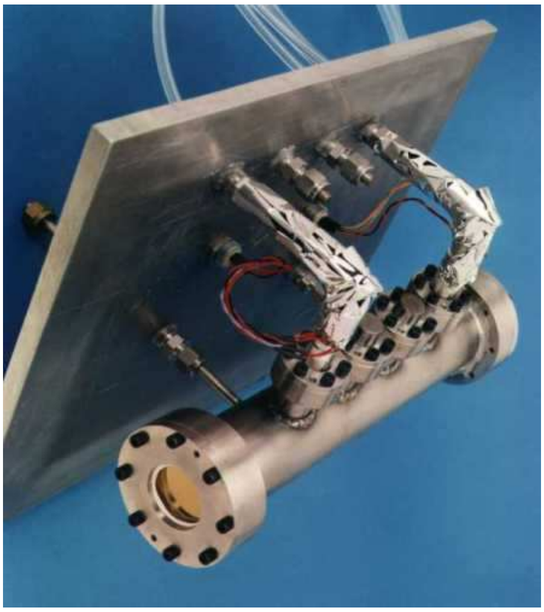

Figure 3.10: Small aerosol cell used at the RAL MSF.

The cell allows the measurement of actual aerosol samples, rather than thin films of aerosol substances or pellets of material representing aerosol. The temperature in the cell can be varied from 180 K to 350 K, allowing the study of different phases of aerosols (e.g. amorphous, crystalline solid and liquid droplets). Potassium bromide was chosen for the optical windows at each end of the cell due to its high transmittance over a wide wavenumber range (maximum transmission at approximately 450–40,000 cm^{-1}).

Multiple Scattering

Multiple scattering occurs when a photon interacts multiple times with the aerosol particles in the cell. As the Mie scattering calculations assume single-scattering, this could provide a significant source of error. However, a study by Brian (2001) found that multiple scattering in the RAL aerosol cell was significant for only a very narrow wavenumber range between $5600\,\mathrm{cm}^{-1}$ and $7000\,\mathrm{cm}^{-1}$; a range in which no aerosol absorption is expected for the compounds being studied. It is therefore reasonable to assume that multiple scattering will have negligible effects on the experimental data.

Channelling

Channelling refers to optical interference between multiple reflections from the front and back surfaces of transmissive elements in an optical configuration. It is usually manifest as a near-sinusoidal modulation of the spectral continuum (Beer, 1992).

Channelling effects may be minimised by a number of techniques:

- Anti-reflective coatings on the surfaces of the transmission optics. While these are effective at eliminating reflections, they are expensive and usually only effective over a narrow wavenumber range. They are therefore unsuitable for Fourier transform infra-red (FTIR) measurements over a large spectral range.

- The use of uncollimated beams will reduce interference effects, though it may not necessarily eliminate them. However, this is not a practicable solution for these studies.

- Wedged transmission optics produce a geometrical separation of the multiply reflected beams (Naylor et al., 1988). This is also expensive. However, it is the most practical option for the current investigation.

Therefore, in order to reduce channelling effects in the aerosol cell, there is a 1° wedge across the surfaces of the KBr windows at each end.

3.3 Particle Size and Number Density

API Aerosizer instrument and a GRIMM Scanning Mobility Particle Sizer + Counter (SMPS+C) were acquired in order to make particle size and number density measurements. Critically, neither instrument requires the refractive index value of particles in order to determine size. The Aerosizer instrument is designed to cover a size range of $0.1\,\mu$m to $350\,\mu$m. However, in practice there was a cut-off at approximately $0.3\,\mu$m. The SMPS+C covers a size range of $0.005\,\mu$m to $0.55\,\mu$m. Similarly, the number densities measured by the Aerosizer instrument may be innaccurate for number densities greater than $\sim 10^3\,\mathrm{cm}^{-3}$. Two instruments were therefore used to improve the accuracy of the results and to cover the full size range of particles produced.

3.3.1 Aerosizer LD

The API Aerosizer measures particles size and concentration using an aerodynamic time of flight method. The method used is independent of aerosol refractive index but requires the density of the aerosol sample. It can take both dry powders and wet aerosols, and measures particles one at a time in the range of $0.20\,\mu$m to $700\,\mu$m. Sample times are selected as a series of three minute runs and the instrument can measure up to 10^5 particles per second. Figure 3.11 shows a schematic diagram of the Aerosizer. The aerosol enters the unit through a capillary tube at the top,

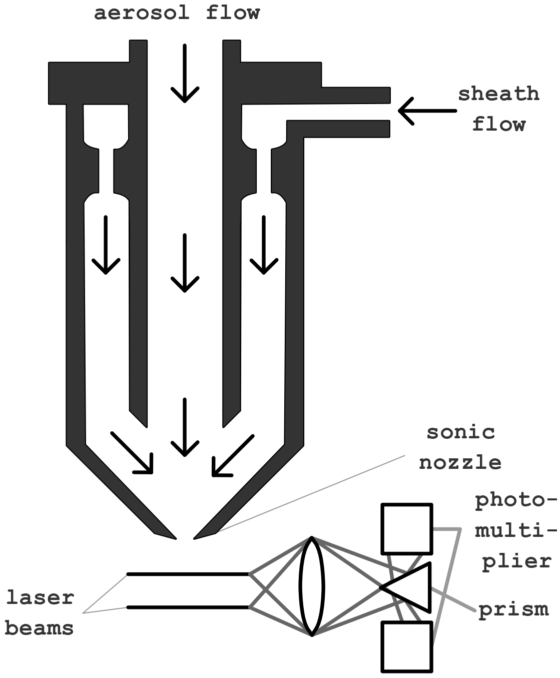

Figure 3.11: Schematic of API Aerosizer LD Instrument.

as shown in the diagram. It is then dispersed in sheath air from the outer tubes and accelerated through a nozzle at near sonic velocity to a partially evacuated chamber. The force of acceleration is controlled by the airflow, and smaller particles experience greater acceleration than larger particles. Two laser beams measure the time of flight of the particles as they pass through the measurement region, shortly after passing through the nozzle. The light scattered by the particles is measured by two photomultiplier tubes. The time of flight is that taken for the particles to pass from one laser beam to the next. The start and stop times of each particle are correlated for each size range. The density of the aerosol is entered and used with the time of flight to determine the size distribution of the aerosol sample (calibration method established by Oskouie et al. (1998)).

A 3 mW laser diode is used to provide a light source. The Aerosizer requires a dilution air flow before the inlet if the number density of particles is expected to be greater than $1 \times 10^3\,\mathrm{cm}^{-3}$. This dilution can be taken into account when plotting the data to ensure accurate number density figures. Data used for the following experiments was plotted using a procedure that plots number density and aerodynamic radius against time (refer to results section for examples).

It is important that the optics of the Aerosizer are cleaned regularly, as they may become saturated with particles and this can lead to inaccurate readings. The sonic nozzle may also become clogged due to large deposits of particulate matter and can similarly be cleaned using isopropanol. The instrument has a diagnostics mode which runs a count rate of background particles. If this is greater than a base value the instrument optics require cleaning and any measurements are unreliable.

3.3.2 GRIMM SMPS + C

The Sequential Mobility Particle Sizer plus Counter (SMPS + C) is designed to make measurements of particles in the size range of $\sim 5\,\mathrm{nm}$ to $30\,\mu\mathrm{m}$. It consists of two parts: the Differential Mobility Analyser (DMA) and the Condensation Particle Counter (CPC).

Differential Mobility Analyser

The DMA differentiates particles by their electrical mobility and is based on the principle of electrostatic classification. When a uniform electric field acts upon a charged particle, the particle accelerates to a limiting velocity. The electrical mobility is the ratio of the limiting velocity to the magnitude of the electric field. Aerosol particles pass between electrodes in the DMA and are subject to an electric field. These particles will all have different electrical mobilities and this allows the DMA to separate the particles. Aerosol particles within a certain size range are removed and passed on to the CPC. Since the voltage size will determine the size range of particles selected, the DMA may be used to produce a monodisperse aerosol of specific size. A schematic diagram is shown in figure 3.12: The sample enters the device at Q$_a$ and meets an impactor. This impactor is designed to remove larger particles at the inlet before they enter the DMA cylinder. Different sizes of impactor are available so that different cut-off sizes may be used. Clean air is supplied from the CPC and enters the top of the DMA at Q$_s$. This sheath air provides a laminar flow close around the high voltage rod in the centre of the DMA. The excess air

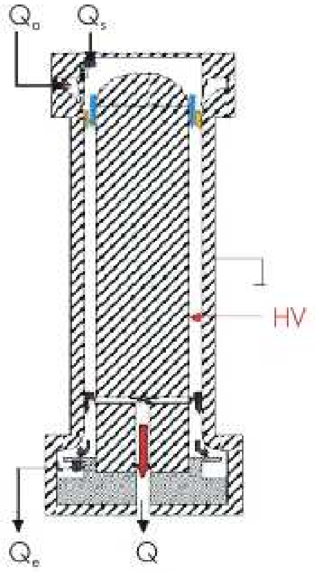

Figure 3.12: Cross-section of Differential Mobility Analyser (GRIMM, 2006).

later exits the DMA and is recirculated.

The aerosol is then passed over a neutraliser. This is a radioactive source that provides a known (Boltzmann) distribution of charge to the incoming aerosol particles. There are a number of different sources that may be used as neutralisers, the most common of which is Am-241. This is an alpha-emitter. It is a bipolar charger that usually consists of gold-coloured foil strips, permanently integrated into a steel housing. The intensity of the source is 3.7 Bq, which is $\sim 100\,\mu$Ci (1 Ci is approx. 3.1×10^{10} Bq; 1 Bq is one disintegration per second). The aerosol particles are ionised after passing over the alpha-source. The charge of the aerosol leaving the neutraliser will be described by a Boltzmann distribution; however, to be sure of this, a value of $\mathrm{N} > \sim 1 \times 10^7$ is required, where N is the number of charged particles.

The sample then enters the top of the DMA cylinder. The DMA consists of two concentric cylinders. These are the electrodes and are connected to a high voltage power supply. The electrodes are charged positively and negatively, so the charged aerosol particles are attracted to them (neutral particles will pass straight through and exit as sheath air at Q_e). The differing mobilities of the (appropriately charged) particles will determine how quickly they reach the central rod. Only particles of a specific size and charge will travel to the rod and escape via a slot to enter the CPC at Q.

The voltage determines the size of the particles selected, and this may be varied in fixed steps of specific sizes. A scan will involve a 10 second pause after each voltage change to ensure that the DMA is empty before the next readings are taken. It is important to note that the DMA differentiates particles according to mobility and not size. Also, not all particles of the relevant size will be appropriately charged to exit via the central rod.

Instrument Limitations & Sources of Error

- Occasionally, particles will become multiply charged. As the particles are classified by electrical mobility rather than directly by size, this will affect the final result. The charge distributions are modelled in the software, and attempts are made to control these distributions using the neutraliser. Neutral particles travel straight through the DMA and exit as sheath air.
- Particle losses are possible due to electrostatic forces generated in the DMA inlet and outlet (Hummes et al., 1996). Additionally, diffusion within the DMA may cause particle losses to the walls (Mamakos et al., 2007).
- There is an ambient humidity operating limit of 95% not condensing - otherwise there may be spark discharge within the high voltage DMA.
- The DMA is only suitable for the particle range 10 – 1100 nm.
- It should be noted that the DMA will not work if the impactor is dirty/blocked, the flow rate is wrong etc., so the impactor was checked and cleaned regularly between measurements.

Condensation Particle Counter

The GRIMM condensation particle counter may be used to find real time concentrations of particles that are too small to be counted by usual light scattering methods. Liquid vapour is condensed onto small aerosol particles to allow them to grow to a sufficient size to scatter light. This is then measured by photodiodes. Butanol is used as the vapour as it is more volatile than water, and therefore more efficient for this purpose. A diagram of the CPC system is shown in figure 3.13. A contin-

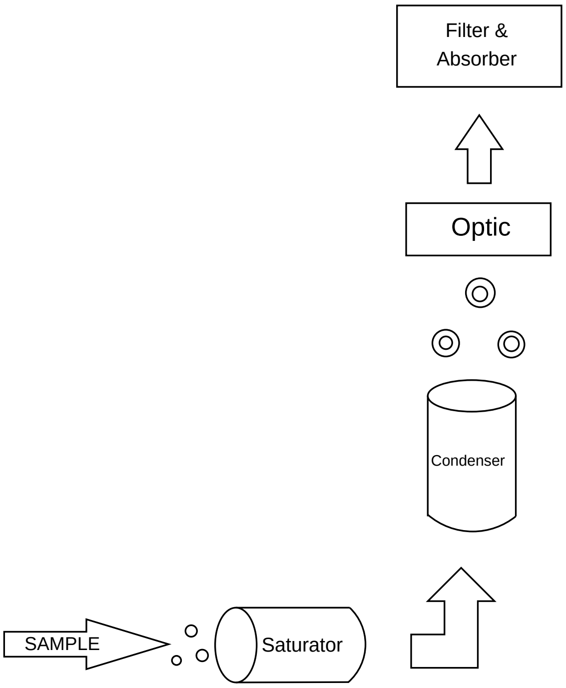

Figure 3.13: Nebulous condensation in the CPC.

uous flow of filtered air carries the aerosol through the CPC. The aerosol sample enters the instrument through a sampling tube and travels to the saturator. Here the aerosol crosses a heated N-butyl-alcohol saturated pipe. The butanol is kept at 35 °C in a felt sponge which is supplied automatically from an integrated alcohol tank. The supply is controlled by an internal sensor. This mixture of alcohol vapour and aerosol particles then enters the cooling condenser unit, which remains at a constant temperature of 10 °C. The supersaturated alcohol vapour condenses onto the aerosol particles, thus increasing their size to $\sim 10\,\mu$m. A carefully managed saturation level ensures that each aerosol particle receives a single droplet of butanol. Nevertheless, information on particle size is lost at this stage, so any size measurements should be conducted before CPC measurements are taken.

The aerosol/butanol droplets leave the condenser and enter the optics where they cross a laser beam causing scattering onto a photodiode. Signal counts per ccm are taken continuously in real time and stored on computer or onto a removeable data card if used in the field. The particles then travel through an active carbon filter before leaving the CPC in order to reduce alcohol odours and particle emissions to the environment.

Raw data is recorded in 300 s scans and stored in a measurement file. It may be exported either as a .txt file or directly into Excel as a spreadsheet.

Instrument Limitations & Sources of Error

- The CPC is able to count up to a maximum of $1 \times 10^{7}\,\mathrm{cm}^{-3}$. For accurate measurements the aerosol input must be stable for at least one minute.
- The instrument may not function reliably if the optics are dirty, or if the droplets are growing to different sizes due to a dilute or insufficient butanol supply. An external reservoir is kept filled and attached to the instrument in order to ensure a continuous supply of alcohol.
- Condensation of ambient humidity in the condenser may dilute the butanol, thus reducing the efficiency of the instrument. To prevent this, an automatic micropump positioned before the condenser removes any such fluid before it runs back into the saturator. Water molecules have a high diffusion rate and very quickly hit the walls of the condenser, whereas the aerosol/alcohol particles are unlikely to do this before leaving the condenser. Therefore only this water, and not the aerosol, is removed. The connection of a reservoir to the outside of the CPC automatically triggers the peristaltic pump to operate

and remove water from the instrument.

- An ambient temperature of greater then 30 °C may adversely affect the operation of the instrument as the internal temperatures of the saturator and condenser then become difficult to maintain. However, such temperatures are not anticipated during the course of this work.

3.4 Summary

A number of different instruments were required as part of the experimental design. Some of these instruments were sourced and purchased from external sources. These were:

- Nebuliser - this was required for aerosol generation. Industrial designs of nebulisers produced a wider size range of aerosol particles and greater number densities than an atomising device that might have been manufactured in-house. The OMRON U-17 nebuliser was purchased after in-house testing and comparison with other devices showed its optimal performance and suitability for this work. The instrument was adapted and fittings were designed and produced to connect the nebuliser to a gas source and the remaining experimental set-up.

- MSF Aerosol Cell & FTS Spectrometer - Previous studies at the RAL MSF had resulted in the production of the small aerosol cell which was designed specifically for spectroscopy of aerosols. The decision to use these instruments was therefore straight-forward.

- API Aerosizer - The Aerosizer instrument had previously been used for aerosol studies at Oxford and exhibited a good response for most of the size range that was to be studied. While the aerosizer does not cover the whole of the expected size range, the information it provides will be useful in determining the accuracy of the final model of the aerosol size distribution.

- GRIMM SMPS+C - This was chosen after an introductory training session on its use and application at GRIMM headquarters in Germany. A secondary instrument was required to ensure complete coverage of the size range of particles to be analysed, and the CPC instrument provided increased accuracy over the Aerosizer due to its counting mechanism, which ensured that only single particles, rather than any aggregates, were counted.

The remaining instruments were designed and manufactured, either in-house or, in the case of the conditioner, out-sourced to an external glass-blower. These instruments were:

- Diffusion Dryers - two diffusion dryers were designed and produced to suit specific requirements for the experiment. This meant that the materials used could be specially chosen to avoid reactivity. The dryers were designed specifically to withstand the pressures and temperatures to be experienced during the aerosol studies, and could be part-filled or regenerated as required during the experimental work.

- Conditioner - This was designed to satisfy requirements specific to the aerosol studies being undertaken. It was manufactured by R. Payne, a glassblower that was associated with the Department of Biochemistry, University of Oxford, in 2005.

Chapter 4

Experimental Procedures

The final outline of the experimental configuration is given in figure 4.1.

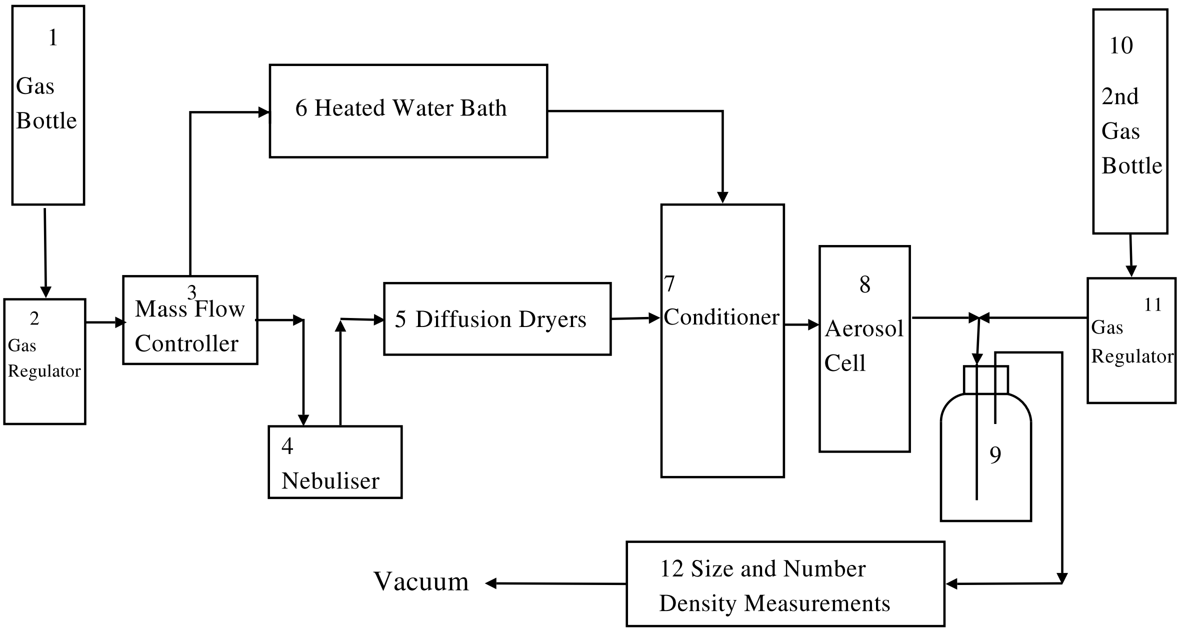

Figure 4.1: Overview of experimental set-up at the RAL MSF in November 2005. Part 9 is a glass dilution vessel required to dilute the aerosol flow to a level acceptable to the particle sizing instruments.

The laboratory measurements were undertaken at the Molecular Spectroscopy Facility at the Rutherford Appleton Laboratory. Measurements were made at room temperature with both wet and dry sea salt aerosols, as well as dry sodium chloride aerosols. The aerosols were made by nebulising solutions of the appropriate compounds prepared using analytical reagent grade water. Sea salt solutions were prepared using Maldon sea salt crystals. These are obtained by simple evaporation of sea water collected from the southeast coast of Britain. The chemical analysis of the composition of these crystals was performed and is given in table 4.1[1].

Chemical compound	Percentage (%)
sodium chloride	98.80
potassium chloride	0.018
magnesium sulphate	0.100
calcium sulphate	0.550
water	0.800
insoluble residue	0.035

Table 4.1: Chemical composition of Maldon sea salt.

Nitrogen was used as an inert buffer gas into which the wet aerosol was introduced by the nebuliser. This was then dried through two diffusion dryers (figure 4.2) before it passed into a two litre glass conditioning vessel. Here the relative humidity of the aerosol was varied by the introduction of water vapour from a heated water bath. The conditioner was of an appropriate volume to ensure the correct residence time to allow the aerosol particles to grow to a stable size. The aerosol then travelled into the aerosol cell where intensity measurements were made over a range of wavelengths using the Bruker 66V/S Fourier transform spectrometer. After this a dilution flow was added to the main aerosol flow and particle size and number den-

---

[1] We are aware that the percentage composition amounts to 100.3 %. We believe this anomaly is due to rounding errors

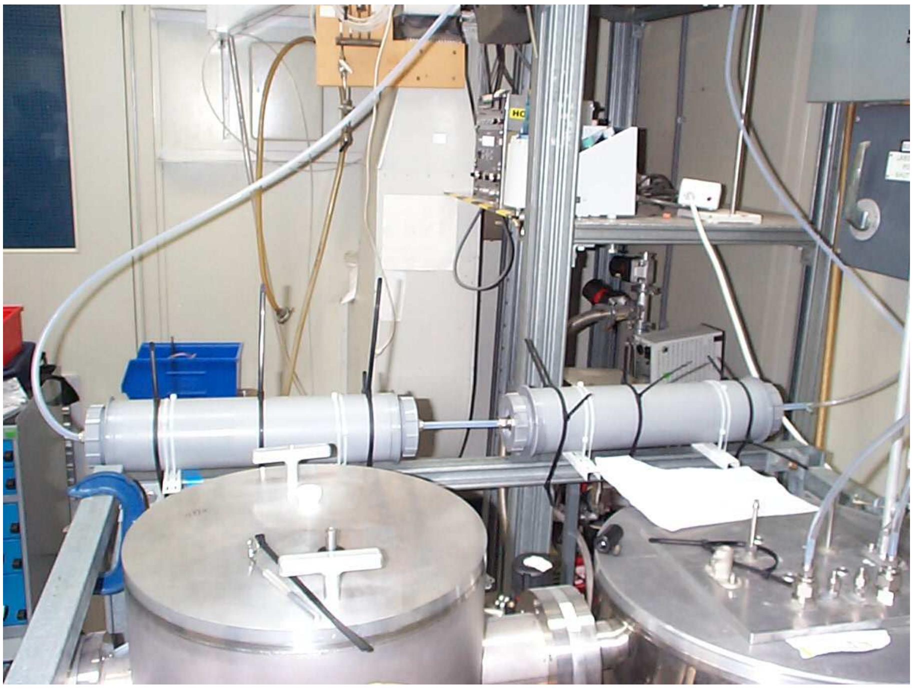

Figure 4.2: Diffusion dryers set-up over the aerosol cell and spectrometer optics at the RAL MSF in November 2005.

sity measurements were made before the aerosol was evacuated. It was important for the aerosol to be diluted after leaving the aerosol cell as the high number densities produced by the nebuliser were outside the range appropriate for the Aerosizer instrument. This dilution was taken into account in subsequent data analysis to ensure that values of particle number density were accurate. The GRIMM Condensation Particle Counter was used to record particle number density and, during certain experiments, the GRIMM Differential Mobility Analyser was also used to make particle size measurements. This was done to ensure the full range of particle sizes was covered. PFA tubing of 3/8” diameter and Swagelok fittings were used to connect all instruments. This provided a gas-tight configuration to minimise contamination of the aerosol. The nebuliser produced aerosol of varied size distributions depending on the concentration of the solution used. A number of different concentrations of solution were therefore prepared to cover a range of sizes representative of tropospheric aerosol.

The aerosol cell was cleaned before measurements began in order to minimise contaminants. The aerosizer optics were also cleaned at the beginning of each day, before experiments began, and at intervals during each day as required. The dryers were carefully monitored and dried out in a vacuum oven or replenished at the first sign of saturation (i.e. colour change of the silica gel). Measurements of relative humidity and temperature were made at the exit of the conditioner, as mentioned in the previous chapter.

It was assumed that the pressure in the aerosol cell remained constant at standard atmospheric pressure. However, only the temperature of the cell was monitored for the sodium chloride and sea salt aerosol measurements. Nevertheless, this temperature variation was of a maximum of $\pm 1\,^\circ$C throughout the experiment. As the volume of the cell is fixed, this would have resulted in a very minor effect on the pressure (± 0.3 mb).

The first phase of room temperature measurements was conducted in May, 2005. Dry aerosols of sodium chloride and sea salt were successfully produced and measured. However, the resulting spectra showed significant levels of noise due to a misalignment of the mirrors in the Bruker Fourier transform spectrometer, which led to a particularly low signal. No detailed analysis or refractive index retrieval could be undertaken on these spectra due to the poor signal to noise ratio. The experiments were therefore repeated in October, November and December, 2005.

4.1 Detailed Procedure

1. At the beginning of each day the system was flushed through with nitrogen for approximately 20 minutes. This purged the system of contaminants and also allowed the components to reach an equilibrium temperature before measurements began. The aerosizer optics were then cleaned and the impactor of the DMA was also cleaned and regreased to ensure each instrument was unclogged and working efficiently.

2. After this the background spectra were recorded. These contain the spectral response of the detector, the lineshape of the light source and any artefacts introduced by the windows of the optical cell. These backgrounds could then be removed from the spectra. Backgrounds were recorded as often as possible to monitor possible drift effects and contamination of the cell. Aerosizer and CPC background readings were also taken to record the level of background particulates.

3. The relative humidity of the system was then set by introducing water vapour from a flow of nitrogen over a heated water bath. The ratio of nitrogen to water was varied to control the relative humidity of the system. The nebuliser was switched on and the system was left to equilibrate for between 15–40 minutes, depending on the nitrogen flow rates set for the experimental run, in order to minimise thermophoretic effects. The nebuliser was set to the maximum nebulisation rate throughout the experiment to ensure that an adequate particle number density was obtained.

4. Once the relative humidity readings became constant, the aerosizer was used

to confirm that a sufficient number density of particles was passing through the aerosol cell before spectra were recorded. One spectrum was taken every minute for at least 30 minutes and the results were averaged to produce a final spectrum. This was done to minimise noise in the measurement. Aerosizer and SMPS + C measurements were also taken simultaneously.

5. The relative humidity was then varied by varying the flow rates of nitrogen and water vapour through the conditioner and the system was left to equilibrate for an appropriate length of time before measurements were once more taken. this was repeated for a number of different values of humidity.

6. If sufficient time remained, a final background measurement was taken at the end of the day, having flushed the system through with dry nitrogen, to ensure the background remained constant.

7. This process was repeated for solutions of different concentrations, for sea salt, and later for ammonium sulphate and ammonium nitrate compounds.

8. Occasionally, measurements were begun as soon as the nebuliser was switched on, in order to monitor the build up of aerosol in the cell.

9. The silica in the diffusion dryers was checked at the beginning and end of each day. If the silica seemed excessively green (i.e. wet) the wet silica was replaced with fresh, dry silica. The saturated silica would then be placed in a vacuum oven overnight. This was usually sufficient to allow the silica to dry out.

10. All equipment and tubing was thoroughly cleaned and flushed through with nitrogen at the end of each set of measurements with a particular aerosol compound, and before a new compound was introduced for measurement.

4.2 Results

Aerosols particles of sodium chloride, sea salt compounds were successfully produced. The nebuliser struggled to disperse solutions with a salt concentration greater than 12 %. It performed more efficiently with solutions of low concentration, where particle number densities of up to $2.9 \times 10^6\,\mathrm{cm}^{-3}$ were produced. However, once discovered, this phenomenon was of little importance as the solution concentration affects only the dry particle size of the aerosol. A summary of the experiments undertaken, and therefore the results obtained is given in table 4.2. Sodium chloride measurements were undertaken for validation purposes as the refractive indices of NaCl are well known (Querry et al., 1976). For the other compounds, several experiments were conducted at various different RH values within the ranges expressed. The individual experiments are too numerous to detail here. However, an example of the raw intensity spectra measured by the spectrometer is shown in figure 4.3. The overall intensity of light radiation through the cell is lower for the sample spectrum than for the background spectrum, as expected. The presence of water vapour contamination is evident at $\sim$1600 cm^{-1} and $\sim$3600 cm^{-1}, while the lines at 2400 cm^{-1} indicate the presence of carbon dioxide. These gas contaminants may be retrieved and removed from the spectra. This process will be outlined in the following chapter. Further examples of transmission spectra for each aerosol sample are shown in Appendix B.

Aerosol	Temperature	Concentration (%)	Relative Humidity (%)
sodium chloride	room	4.7	dry
sea salt	room	4.7	0.4–86.0
	room	3.1	0.00–95.6

Table 4.2: Summary of results obtained.

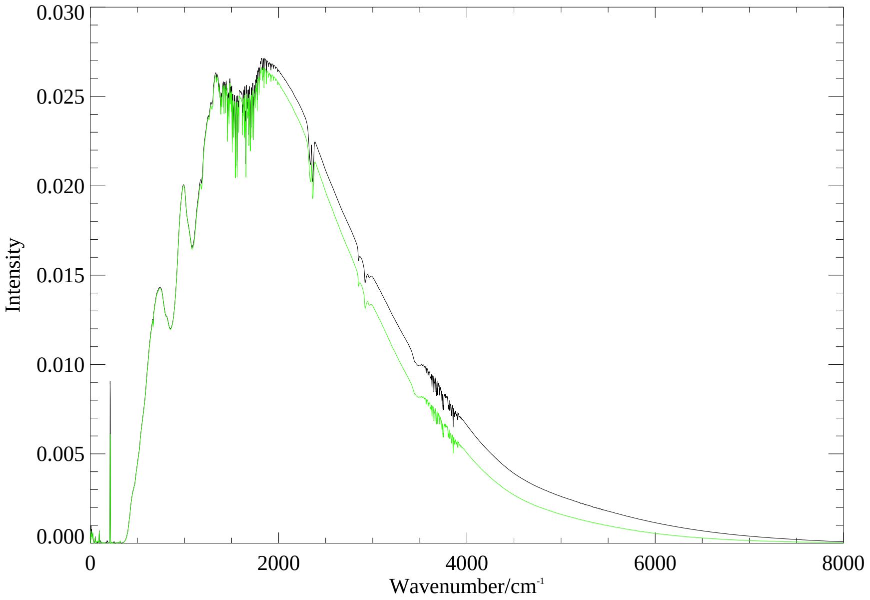

Figure 4.3: Plot showing the raw intensity spectrum for dry sea salt aerosol (green) and a corresponding background spectrum taken immediately before the sample measurement (black). Water vapour lines are visible at ∼1600 cm^{-1} and ∼3600 cm^{-1}. The lines at 2400 cm^{-1} are due to absorption by CO_2.

4.3 Summary

- Transmission, particle size and number density measurements of Maldon sea salt aerosol were made over a range of RH values. Analytical reagent grade water was used to create the salt solutions.
- Additional measurements of dry sodium chloride aerosol were also made for validation purposes.

Chapter 5

Pre-Processing of Data

A single aerosol spectrum was used to refine the analysis process required to retrieve refractive index data. In order to obtain suitable transmission spectra for the refractive index retrievals, the raw data would require pre-processing to remove the background information and any gas lines in the spectra. The final aim was to compose a generic IDL procedure that would take any file produced by the Bruker spectrometer and complete all pre-processing necessary to prepare the spectra for refractive index retrieval, regardless of the composition of the measured aerosol. This chapter outlines the processes undertaken to achieve this.

5.1 Removal of Backgrounds

The spectrometer measures an interferogram which is Fourier transformed to a corresponding intensity measurement automatically after the measurement is taken. The background spectra must then be removed from the measurements to give a spectrum corresponding solely to the salt aerosol introduced to the cell. This is done by taking the ratio of the two intensity spectra:

$$\tau_c(\nu, T) = \frac{I(\nu, T)}{I_0(\nu, T)} \tag{5.1}$$

The background measurements were taken at the beginning and end of every day, as well as at intervals throughout the day, if there was time. This allowed the monitoring of any drift in the baseline of the background spectra throughout the day. To compensate for these and to ensure the correct background state was used to calculate transmission for each measurement, the background data sets for each day were filtered and smoothed over time using a Kalman filter and, where possible, a Kalman smoother (Kalman, 1960). A detailed description of the mathematics of the Kalman filters and smoother is given in Appendix D. For a clearer understanding of how the filters are applied, consider the following examples:

5.1.1 Kalman Forward Filter - Example 1

Where there are only viable background measurements at the beginning of the day, a forward filter is applied. Figure 5.1 shows a plot displaying some of the forward filtered results. Each measurement spectrum is represented by a single value taken from a point in the spectrum where there is no absorption or scattering contribution from the aerosol. At the beginning of the day, a number of background spectra were measured. Aerosol was introduced to the sample chamber and intensity measurements were taken approximately 40 minutes later. A Kalman forward filter is then applied to the background measurements in order to calculate estimates of the backgrounds at the time of each aerosol measurement. At any time where background measurements were made, there are two estimates of the background. These are the

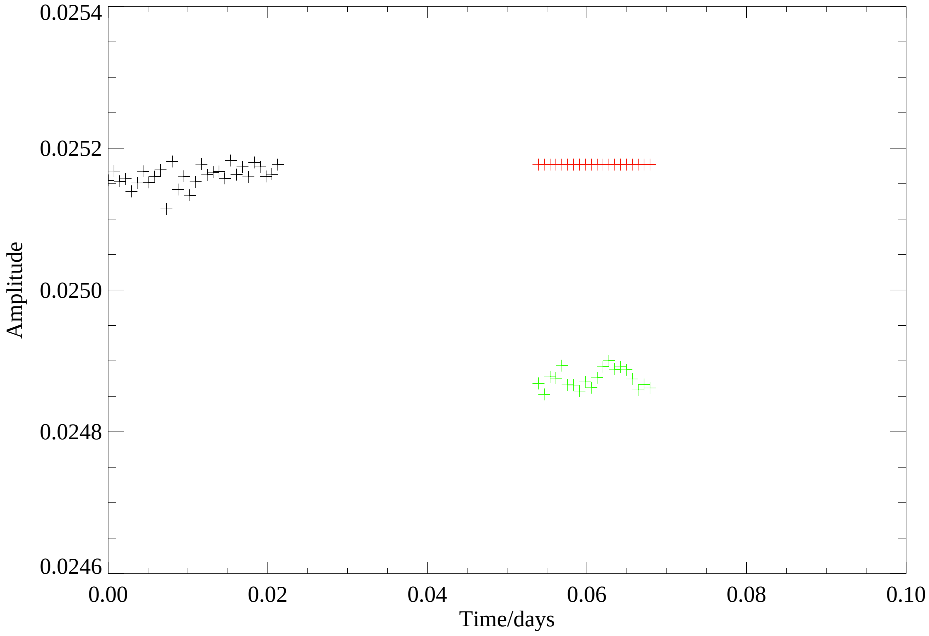

Figure 5.1: Kalman filtered backgrounds (red points) shown with original backgrounds (black points) and aerosol data for which backgrounds were required (green points).

actual measured values at that time, and the running estimate of the backgrounds based on all previous values. The uncertainty on the running estimates increases with time at a rate determined by a smoothing parameter. The two estimates of the state are combined to provide a final value. At times where no measurement of the background was taken, the value used is the value calculated at the last time the final background was updated. This is the forward filter. The backward filter works in the same way but begins with measurements taken at the end of the day and works backwards in time.

5.1.2 Kalman Smoother - Example 2

The Kalman smoother is used when there are background measurements at both the beginning and end of the day, or at various points throughout the day. It runs both the forward and backward filter and then combines the resulting estimates with appropriate weightings to give a final, more accurate value. Figure 5.2 shows an example of backgrounds that have drifted in intensity over the course of the day. The Kalman smoother is used to provide a more accurate estimate of the background at the time of the measurement, given the trend in drift of the backgrounds. It should be noted that whilst in this example the smoothing appears to simply provide a linear interpolation, this is not the case, as can be seen from figure 5.3 which gives a close up of the smoothed backgrounds. The red points show the backgrounds

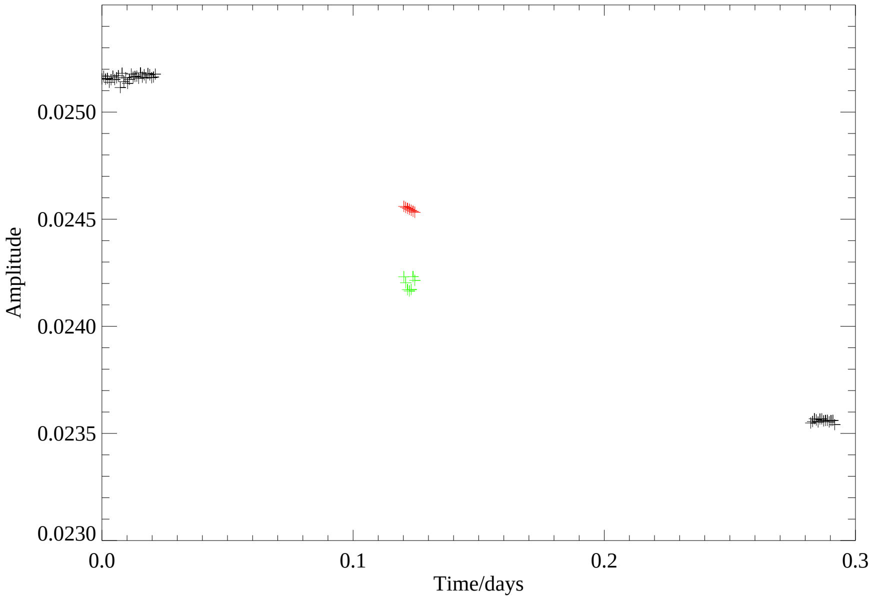

Figure 5.2: Kalman smoothed backgrounds (red points) shown with original backgrounds (black points) and aerosol data for which backgrounds were required (green points).

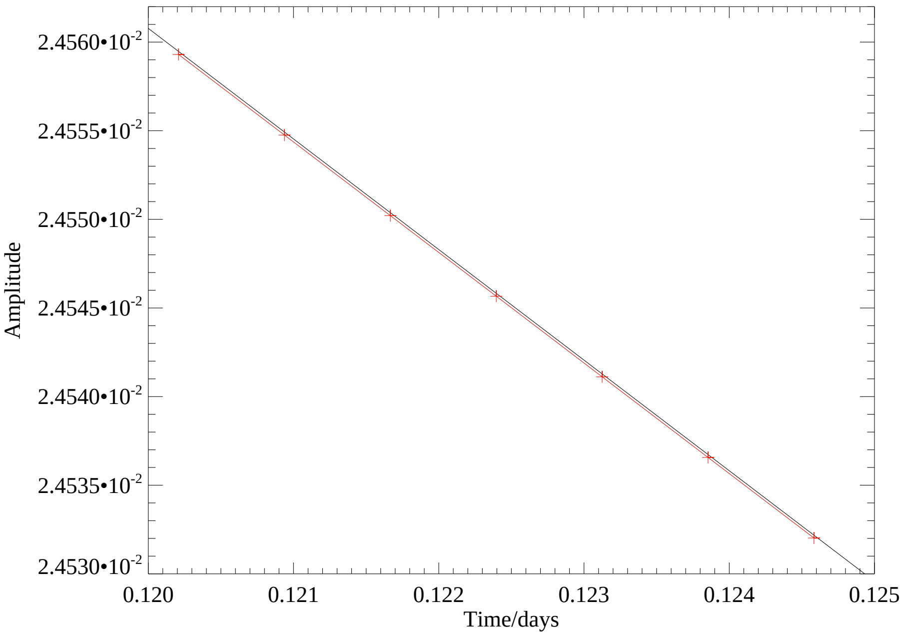

Figure 5.3: Close up of Kalman smoothed backgrounds (red points) shown with linear interpolation of original backgrounds (black line).

obtained at the times of the measurements, while the black line shows the position of a linear interpolation between the two sets of background measurements. There is a slight but nevertheless discernible difference between the two.

5.1.3 The Smoothing Parameter

The smoothing parameter, a, determines the level of smoothing applied. In the limiting case where $a = 0$, there is maximum smoothing and the final estimates will be a simple average of all measurements with no regard to the time at which each measurement was taken. Similarly, where $a = \infty$ there is minimum smoothing and each estimate is simply equal to the last background measurement.

The smoothing parameters were determined using a trial and error method. If deviations in the trend of the backgrounds was random, then the smoothing parameter was increased. Conversely, if these deviations were systematic then the smoothing parameter was decreased until a balance was found. Transmission spectra were then calculated using equation 5.1 with Kalman filtered backgrounds corresponding to the time of each particular measurement. A sample spectrum is shown in figure 5.4.

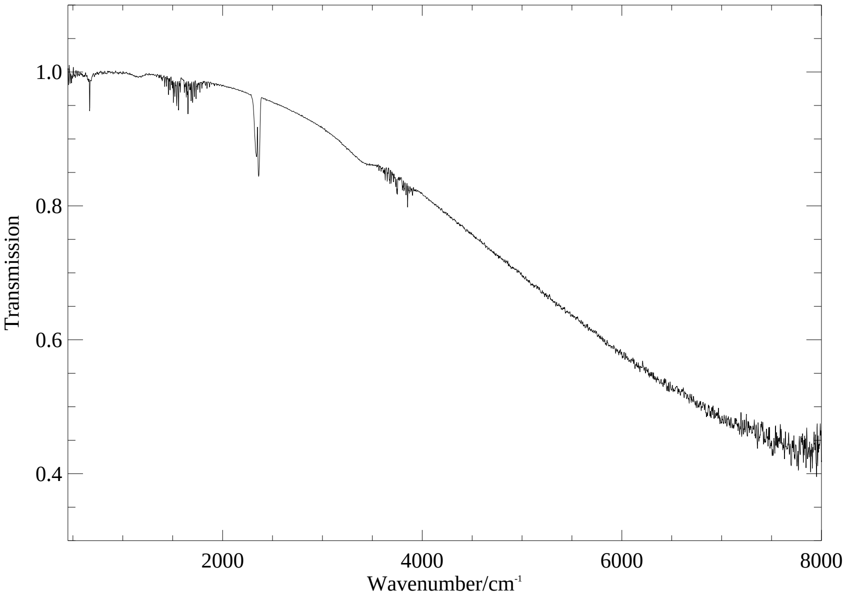

Figure 5.4: Transmission spectrum of dry sea salt aerosol.

5.2 Uncertainties in the Transmission Spectra

The noise in the transmission spectra varied with wavenumber. This can be seen in figure 5.4, where the noise is at its greatest at the edges of the spectral range featured. However, between 500 and 6000 cm^{-1}, the uncertainty due to the noise has a maximum of 5×10^{-3}, which is considered to be negligible. This was calculated by identifying areas of the transmission spectrum where there were no spectral features and fitting polynomial functions to the spectra. The standard deviation of the measurement points about this function was then used to estimate the noise.

The spectrometer took a measurement every minute and, on average, between 10 and 30 measurements were averaged to produce each intensity spectrum, in order to minimise the noise level in the measurement. These individual measurements usually exhibited very little deviation from each other, if the aerosol produced was stable. As a result, the error on the transmission spectra, calculated from the variance in the measurements, is very small. Figure 5.5 shows a close up of the dry transmission spectrum shown previously. This time the upper and lower error boundaries are also shown.

Further to section 3.2.2, there was no evidence of channelling in the measured spectra. Therefore no systematic errors due to this phenomenon were included in the analysis.

The calculated transmission spectra were seen to be oversampled. They were on a $0.2\,\mathrm{cm}^{-1}$ grid, but had an actual resolution of $2.0\,\mathrm{cm}^{-1}$. They were therefore converted to interferogram space by Fourier transform, truncated to a $2.0\,\mathrm{cm}^{-1}$ grid, and then converted back to transmission spectra.

After this, the removal of gas lines from the spectra was attempted.

5.3 Removal of Gas Lines

Some of the aerosol transmission spectra included gas lines of water and carbon dioxide (see figure 5.6). It was therefore necessary to retrieve the amount of water

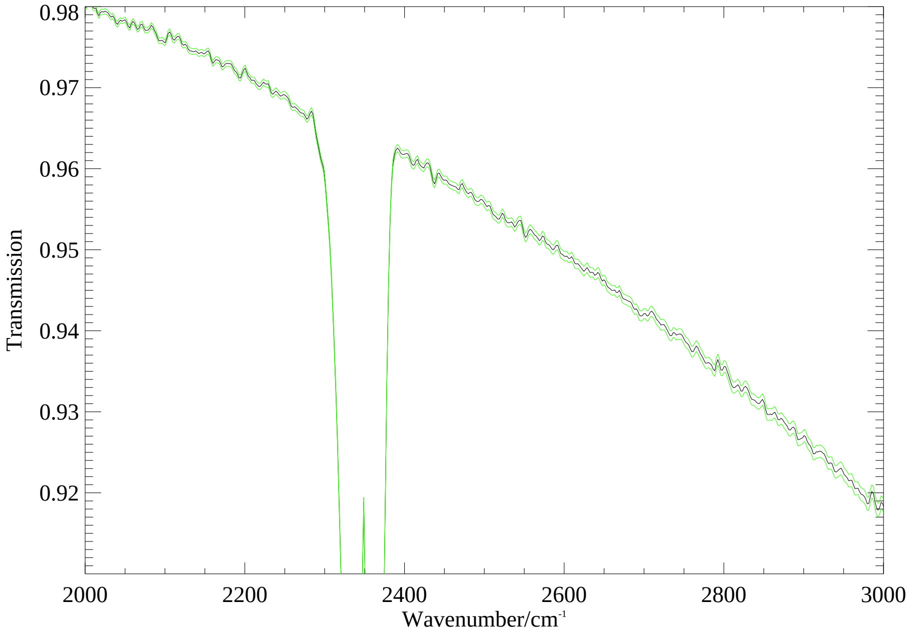

Figure 5.5: Transmission spectrum of dry sea salt aerosol (black line) with error boundaries (green lines).

and CO_2 in the spectra in order to remove the gas lines. This was done by means of an iterative non-linear least squares fit retrieval (see Appendix A for further details). A forward model was required to describe the transformation between the state vector, in this case the scalar value of the amount of unknown gas in the transmission spectra, and the measurements. The AOPP Reference Forward Model (RFM) (AOPP, 2006) was therefore used to derive transmission spectra at different values of CO_2 and H_2O concentration. This is a radiative transfer model originally designed to provide reference spectral calculations for the MIPAS[1] instrument.

Two methods of removing gas lines were eventually investigated.

---

[1] Michelson Interferometer for Passive Atmospheric Sounding

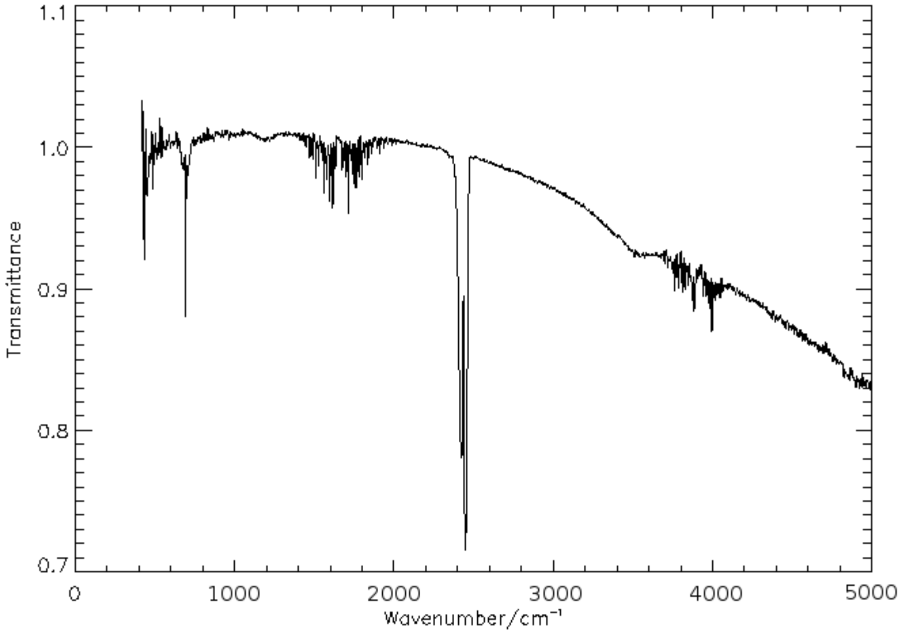

Figure 5.6: Sea salt transmission spectrum with water vapour and carbon dioxide gas lines.

5.3.1 Gas Retrieval - Method 1

The RFM is used to produce a gas spectrum for an initial estimate of the H_2O and CO_2 levels in the aerosol cell during the measurement. This is then convolved with the apodised instrument lineshape of the spectrometer. The gas retrieval is performed at a high resolution so the data must eventually be converted to interferogram space, truncated, and Fourier transformed back into spectral space to give the wavenumber values of peaks present due to the gases (figure 5.7). The measurement spectrum is then filtered to remove all points at which gas lines are expected, and the scattering curve is completed by linear interpolation (figure 5.8). The original measurement is then divided by this result to give a spectrum resulting solely from the gases in the aerosol cell during the measurement (figure 5.9). At this point, we

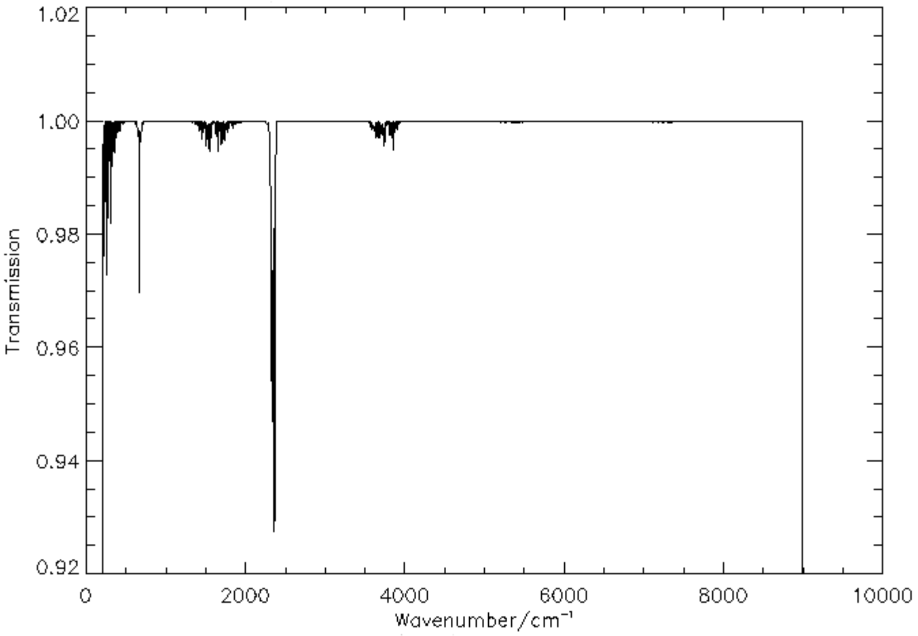

Figure 5.7: RFM output spectrum for H_2O and CO_2 for sea salt measurement (after convolution with instrument line shape).

have a measurement spectrum without gas lines but the method has also removed all other spectral information at these wavenumber points. A retrieval is therefore performed on the gas spectrum obtained from the measurement to determine the amount of CO_2 and H_2O present. The output of this retrieval is a modelled spectrum of H_2O and CO_2, this time more closely representing the actual amounts of gas in the cell. This is removed from the original data (figure 5.10). Hence a more accurate resultant spectrum without gas contaminants is obtained. However, much information is still lost due to salt features being obscured by the gas lines. These features are removed or reduced in size when the gas lines are removed. A different method of removing these lines was therefore investigated: one which would retain those features from the salt aerosol that were being obscured by gas lines.

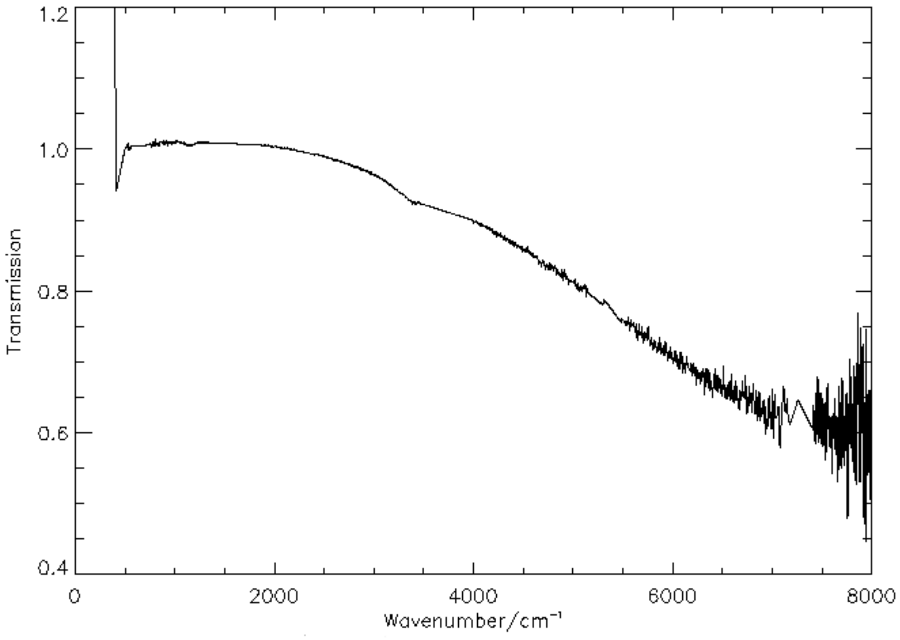

Figure 5.8: Sea salt transmission spectrum filtered to remove modelled gas lines (after linear interpolation).

5.3.2 Gas Retrieval - Method 2

This method was designed to remove contaminant lines in measured spectra whilst retaining spectral features due to salt aerosol that were being obscured by these lines. An overview of the method is outlined below:

1. The measured spectrum (M) is smoothed by applying a boxcar function of a specific width determined individually for each spectrum.
2. This smoothed spectrum (S) is removed from the initial measurement to give an estimated "gas" spectrum (Y). So $Y = M/S$.
3. The RFM is then run to provide a gas transmission spectrum (G) that corresponds to Y.

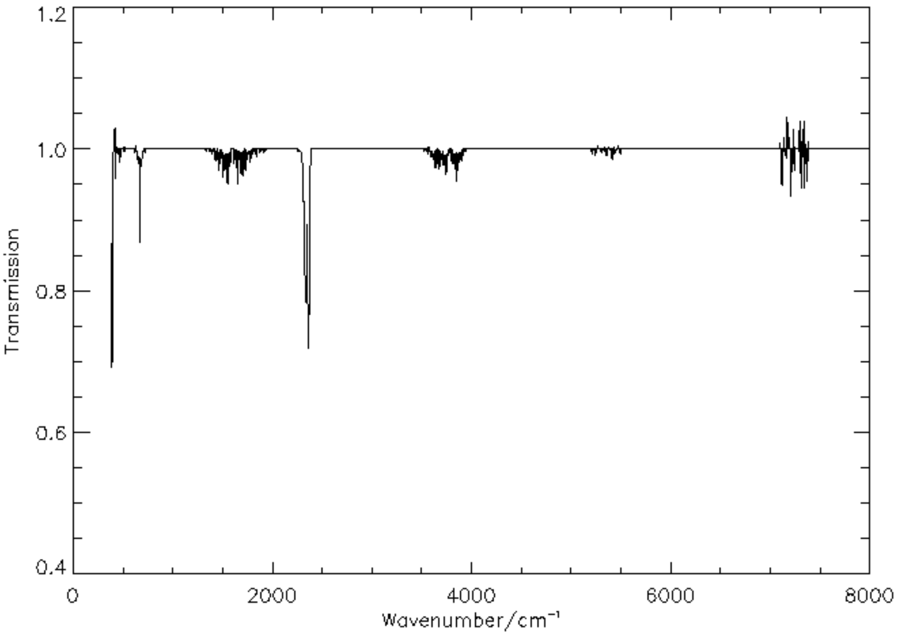

Figure 5.9: Transmission spectrum due to H_2O and CO_2 in the aerosol cell.

4. The RFM output is removed from the initial measurement i.e. $M = M/G$, and the process is repeated from the beginning until a convergence criterion is met. This usually involves specifying a limiting value for the cost change between iterations - in this case approximately 10^3 parts per million by volume of water vapour.

This method should be more effective than the previous methods in retaining aerosol features as we expect the aerosol features to be more slowly varying compared to the gas lines. The resultant spectrum is shown in figure 5.11 and the residual is shown in figure 5.12.

Comparison of figure 5.11 with figure 5.6 shows considerable improvement. Original features of the spectrum at approximately $1500\,\mathrm{cm}^{-1}$ and $3500\,\mathrm{cm}^{-1}$ are retained

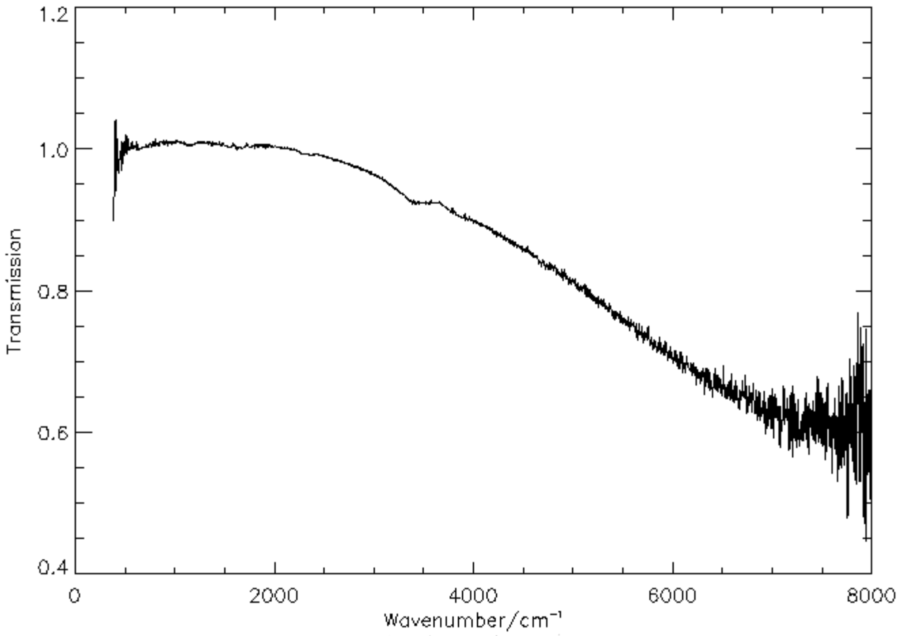

Figure 5.10: Final sea salt spectrum after removal of gas lines by method 1.

in figure 5.11, whereas in figure 5.10 there are merely straight featureless lines at these places in the spectrum. To demonstrate the extent of the removal of gas lines, figure 5.13 gives a close-up of the spectrum in a region where water features are present before gas line removal, and also shows the same region of the spectrum after gas line removal. Where the spectrum has remained unchanged, only the white line is visible.

A quantitative assessment requires comparison of the residual values from the retrieval with the noise level on the measurement. The noise increases rapidly at the edges of the spectral range measured. To determine the quality of the fit, the noise was calculated over the range 1000 to 4000 cm^{-1}, as the noise level remains relatively constant over this interval. The average noise in this region is 2×10^{-3},

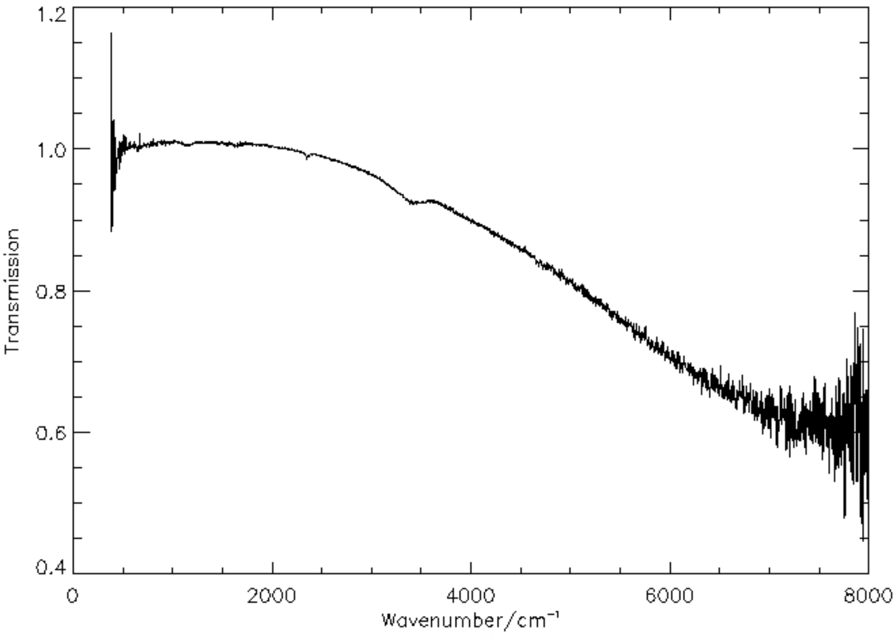

Figure 5.11: Sea salt transmission spectrum after removal of gas lines by method 2 ($Y - f$).

while the variation in the residual is 1.7×10^{-3}. However, this value increases as the amount of water vapour in the measurement increases, until at measurements of approximately 45 % RH, the residuals of the gas retrieval no longer represent noise and some gas lines remain after processing (see figure 5.14).

Nevertheless, the gas retrieval proved to be consistent. Successive retrievals converged to values that were within 3.5 % of each other, regardless of the first guess value provided.

5.4 Summary

- A Kalman smoother and filters were applied to the background measurements in order to obtain an accurate estimate of the background at the time of the

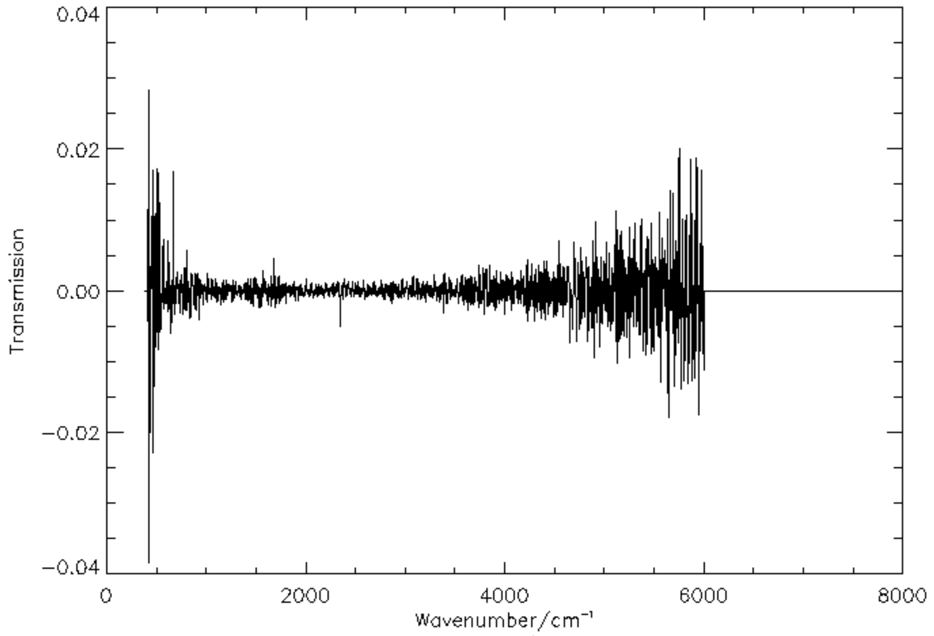

Figure 5.12: Residual of retrieval of gas lines by method 2.

sample measurements, and to eliminate errors due to drifts in the detector signal with time.

- Some of the aerosol spectra showed evidence of contamination with gas lines of water vapour and carbon dioxide. These lines were modelled and removed using a least squares fit retrieval and the AOPP RFM. Two methods were devised and the method which best removed gas lines while retaining aerosol spectral features was chosen.
- The gas retrieval reduced the contribution from gas lines to within the noise level of the spectra. However, the efficacy of the retrieval decreased as the amount of water vapour in the spectra increased. Once the RH of the sample was above approximately 50 % RH, residual gas lines became visible above the

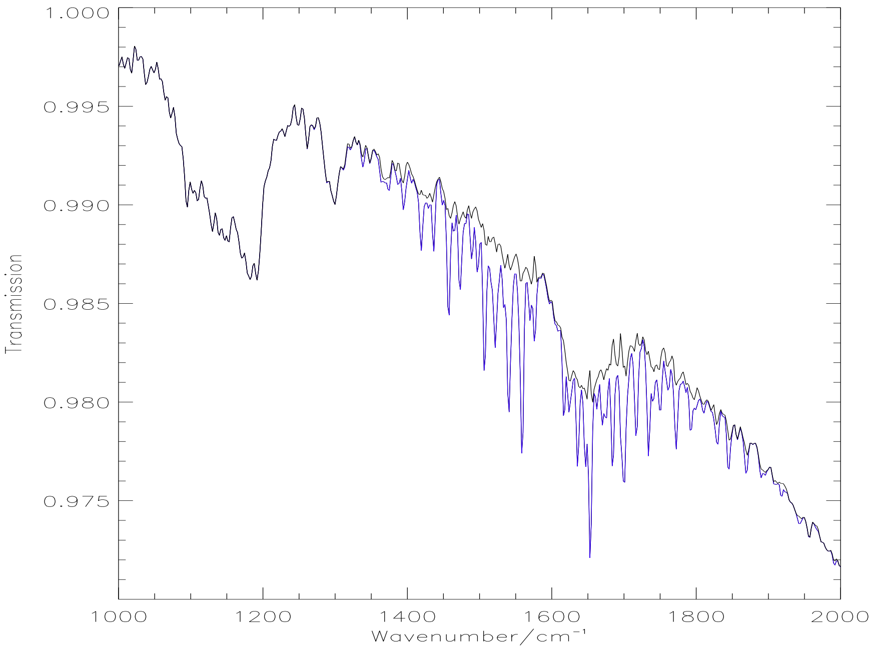

Figure 5.13: Comparison of the transmission spectra before (blue line) and after (black line) gas line removal. The two spectra are completely overlapping except where there are gas lines of water in the original spectrum that were later removed.

noise level after the retrieval was applied.

- A generic IDL pre-processing procedure was written, based on the work in this chapter. This takes the raw data files that are produced by the OPUS software, which controls the spectrometer, and completes all pre-processing, including removal of backgrounds, transmission calculation, gas retrievals, interpolation and convolution of the modelled gas spectra with the spectrometer instrument line shape for accurate gas retrieval, and also the Fourier transforms to and from interferogram space in order to truncate the spectral range. This procedure may be used for any aerosol species measured using a Fourier transform spectrometer.

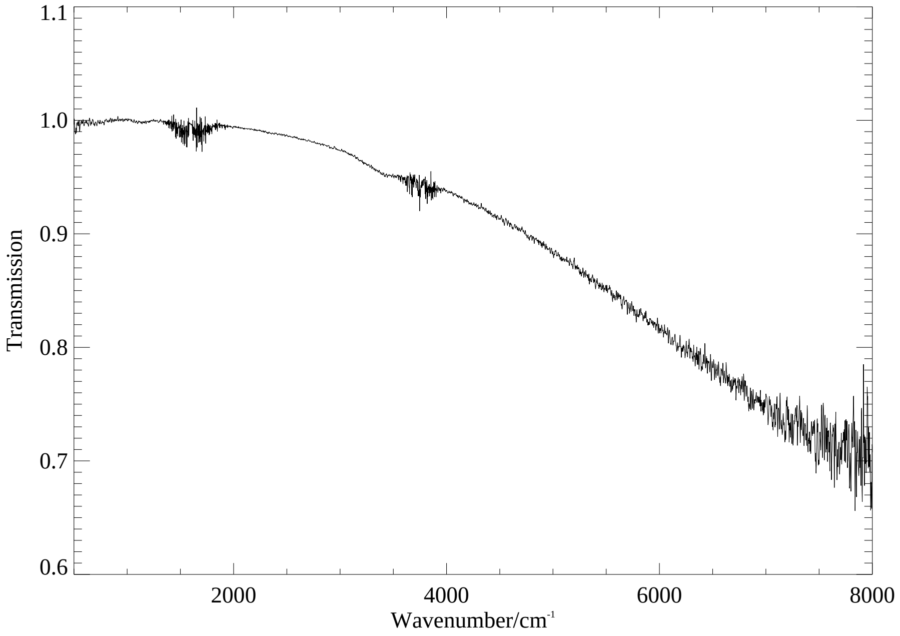

Figure 5.14: Transmission spectrum of sea salt aerosol at 44.7 % RH, after retrieval of gas lines. Note that some residual lines remain.

Chapter 6

Determination of Refractive Index

The refractive index retrieval algorithm used was based on the Levenberg-Marquardt method, as described in Appendix A. The forward model, $\mathbf{F(x)}$, used to relate the state vector, $\mathbf{x}$, to the measurement, $\mathbf{y}$, is based on the classical damped harmonic oscillator model, detailed in section 2.2. The retrieval algorithm minimises the cost function:

$$\chi^2 = [\mathbf{y} - \mathbf{F}(\mathbf{x})]^{\mathrm{T}}\mathbf{S}_{\epsilon}^{-1}[\mathbf{y} - \mathbf{F}(\mathbf{x})] + (\mathbf{x} - \mathbf{x}_{\mathrm{a}})^{\mathrm{T}}\mathbf{S}_{\mathrm{a}}^{-1}(\mathbf{x} - \mathbf{x}_{\mathrm{a}}) \tag{6.1}$$

where $\mathbf{x}_a$ is the best estimate of the state before measurement and $\mathbf{S}_a$ is the corresponding covariance matrix representing the uncertainty in $\mathbf{x}_a$.

6.1 Refractive Index Retrieval from Simulated Measurements

Simulated measurements were used to test the refractive index retrieval algorithm. The forward model was used to generate a model extinction spectrum from a predefined set of CDHO band parameters and particle size distribution data. This extinction spectrum was then used as the input measurement vector for the refractive index retrieval. The a priori band parameters were obtained by varying the measurement by different factors. The position, width and size of the bands were all varied by increasing amounts in order to analyse any resultant effect on the output.

The results of these tests showed that the retrieval was highly sensitive to the position of a priori bands. If these positions were different by too great a factor (in this case, 15 %) then the retrieval would not converge, but would continue to run indefinitely, unless stopped by some other factor (for example, a pre-defined number of iterations had been completed). If the a priori was quite close to the solution, then the retrieval would converge to a solution within one or two iterations (figure 6.1). Thus the selection of the a priori band set is critical to the outcome of the retrieval.

6.2 A Priori Band Set

As the band set parameters contain information about the composition of the aerosol compound, the ideal a priori band set would be defined by infra-red absorption features of component compounds of the aerosol (Thomas et al., 2004). However, such information is often difficult to find. Thus, the most reliable method of obtaining the a priori band set entails inclusion of expected absorption bands from prior knowledge, and the addition and removal of subsequent bands based on a trial and error method. This involves a great deal of user intervention, especially as the retrieval is very sensitive to the position of bands in the first guess.

To explain this, consider a Gaussian curve y_1 of unit peak height and width,

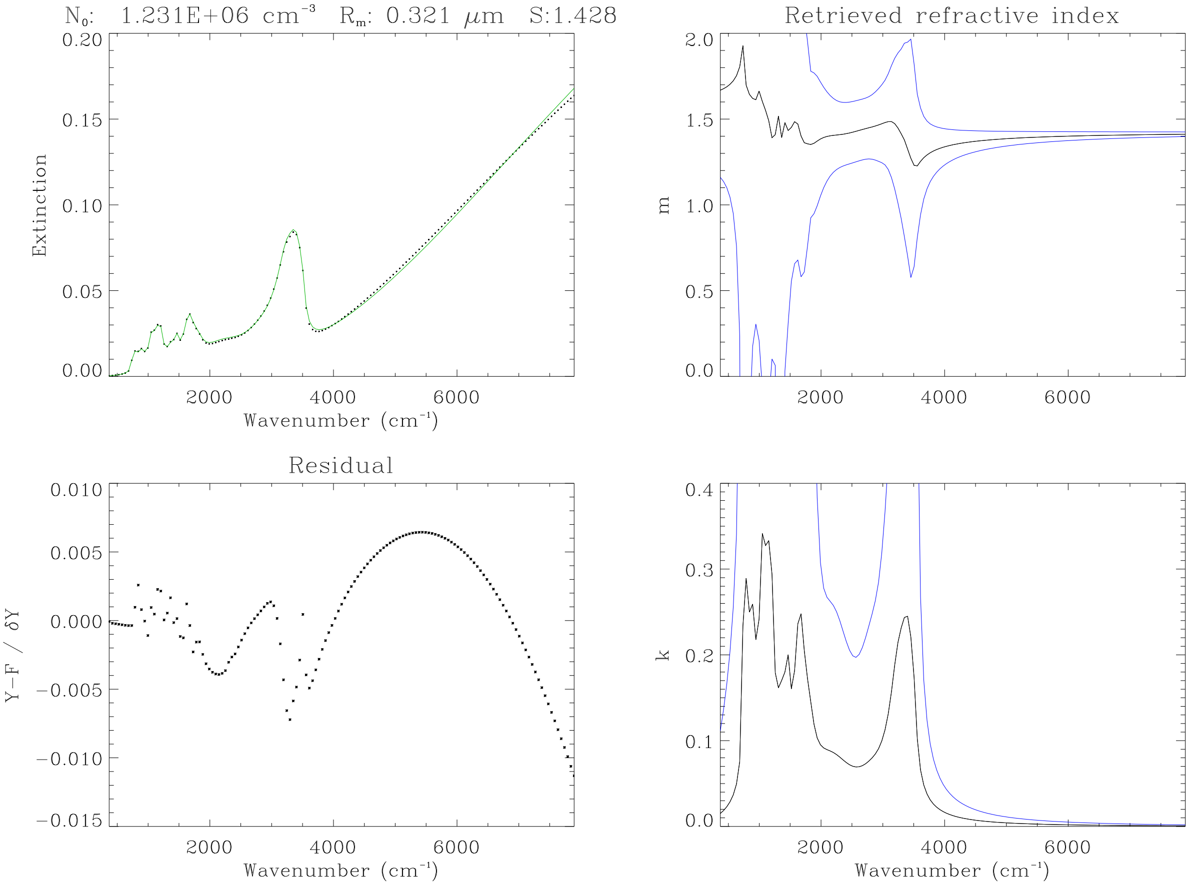

Figure 6.1: Retrieval output for simulated data (black dots on extinction plot) and resulting fit (green line on extinction plot), with retrieved refractive indices (black lines on left hand plots). The blue lines represent the errors.

representing an absorption feature. Now let us vary its position by $\pm x$ about the original central position at 0 (figure 6.2). If the translation of y_1 is called y_2 then let us plot the sum of the square differences $\sum(y_1 - y_2)^2$ against x, where x is the difference in position between y_1 and y_2 (the cost function) (figure 6.3). We can see clearly that there is a trough in this plot. As we move away from this through in either direction, the graph rises by increments so small that the plot appears horizontal in these areas. If a first guess Gaussian to the initial plot is chosen

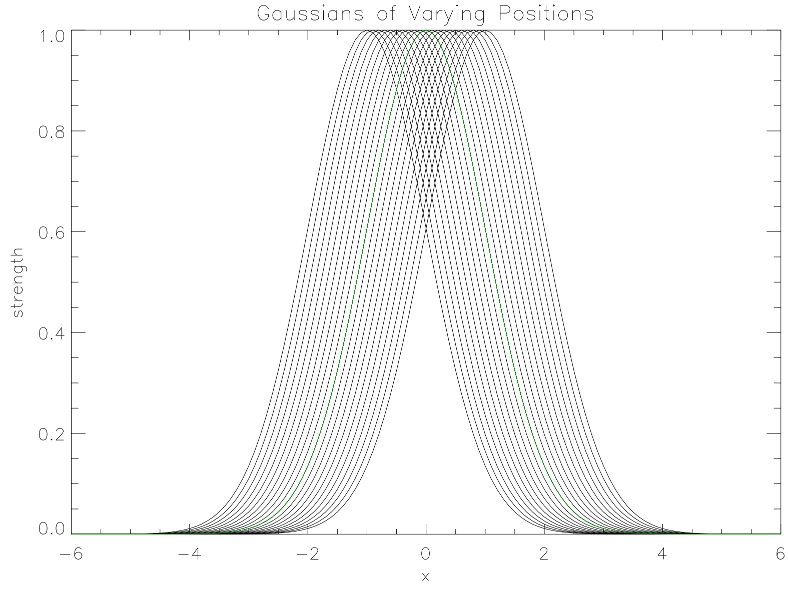

Figure 6.2: Plot showing varying positions of a central Gaussian curve at 0 (green curve)

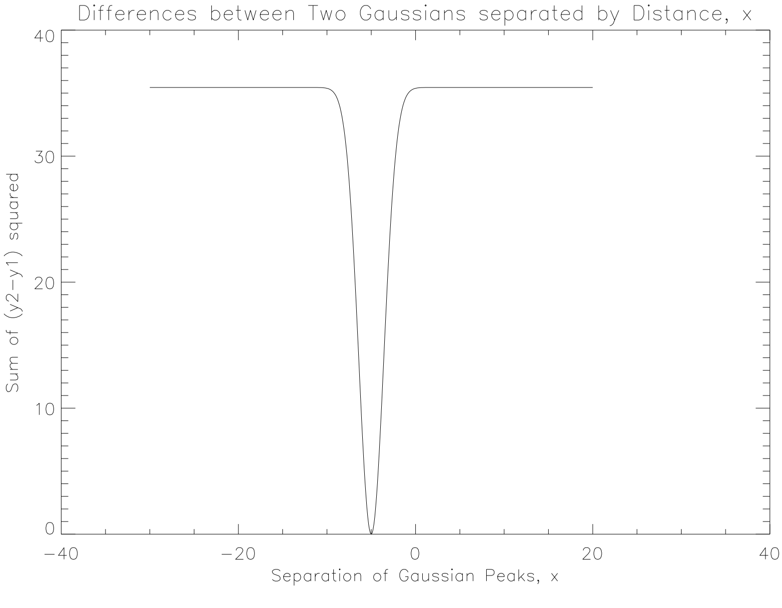

Figure 6.3: Plot showing the sum of the square differences of two Gaussians of varying separation.

that has a corresponding point outside the trough of figure 6.3 then subsequent iterations of a retrieval process will result in the retrieval moving along one of the horizontal arms of this graph, and convergence will occur very slowly or not at all within the stipulated number of iterations. Practically, therefore, it is necessary for the position of the initial guess to be within $3w$ of the solution where w is the width of the original Gaussian. This value comes from the width of the trough in figure 6.3. A similar analysis of the difference in width of the initial guess and solution is shown in figures 6.4 and 6.5 below: This time, the difference plot shows a sharp decline to the left of 0 and a shallow increase to the right. This shows that if the width of the initial guess is too large, the retrieval will be slow to converge, but the gradient is sufficient that convergence should occur nevertheless. Finally, looking at variations in the strength of a Gaussian plot (figures 6.6 and 6.7): The difference plot now shows a parabola, indicating that however far out the strength

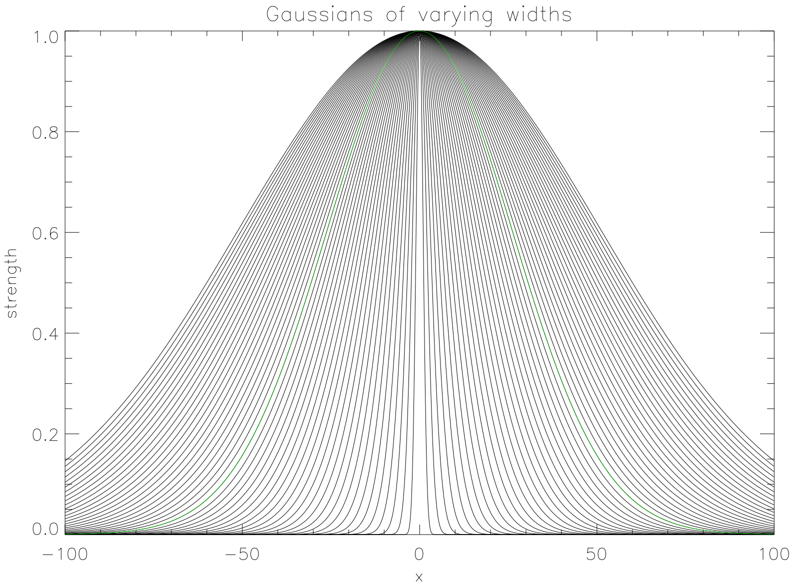

Figure 6.4: Plot showing varying widths of a central Gaussian curve at 0 (green curve)

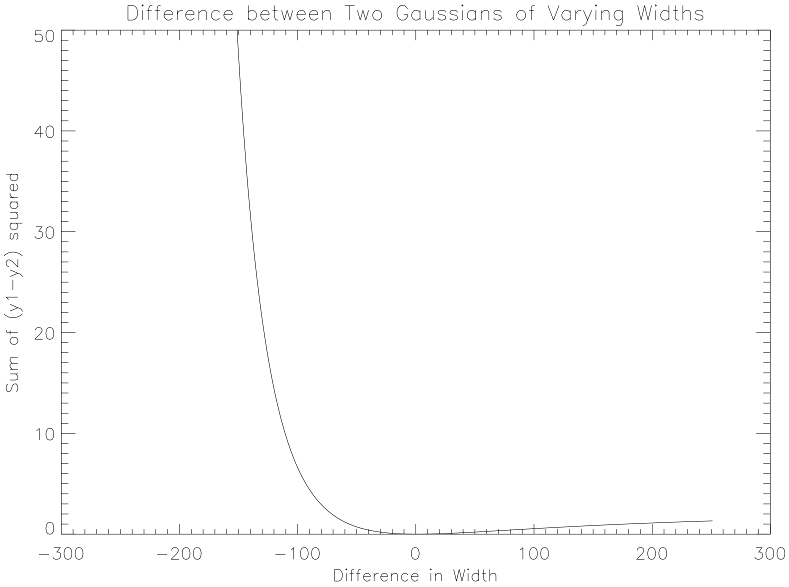

Figure 6.5: Plot showing the sum of the square differences of two Gaussians of varying width

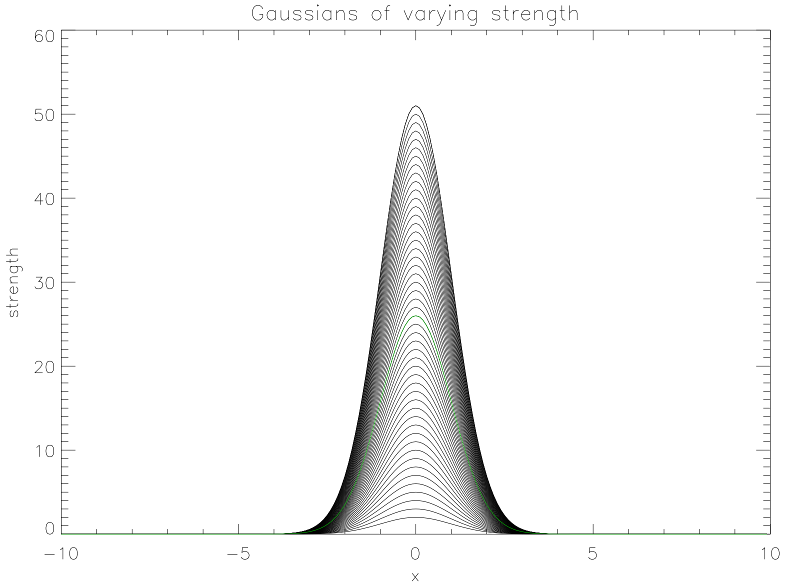

Figure 6.6: Plot showing varying heights of a central Gaussian at 0 (green curve)

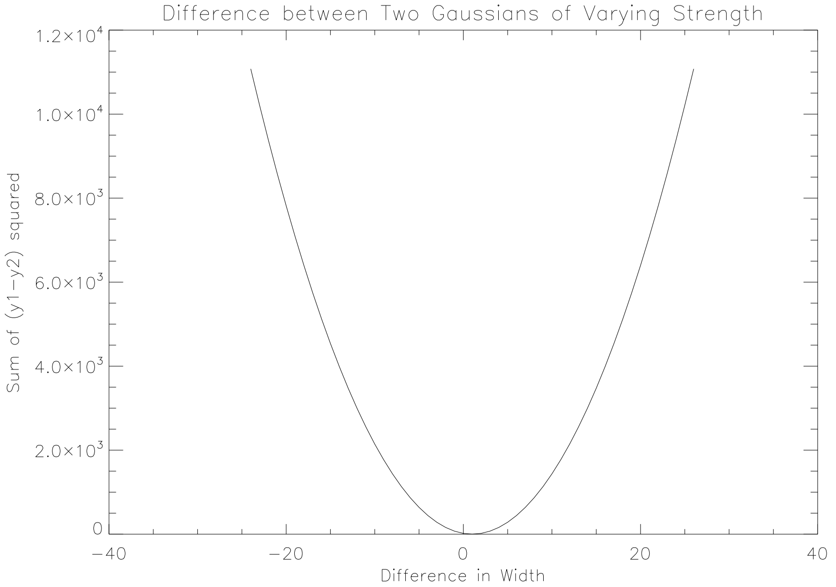

Figure 6.7: Plot showing the sum of the square differences of two Gaussians of varying height

value of the initial guess (wherever the initial point on the parabola is situated) the retrieval will converge to the solution (the bottom of the parabola).

These analyses show that, for convergence to occur within a reasonable number of iterations, a good first guess of position is required. However, there is greater tolerance in the first guess of the width and strength of the bands.

We are now ready to compare measured aerosol data to the literature values to date, and begin a retrieval of the refractive indices from this measured data.

6.3 Validation

Measurements of dry sodium chloride aerosol were made in order to provide independent validation of the pre-processing[1] and retrieval algorithms. The refractive indices of dry NaCl are well known, although there is a slight discrepancy in measured values for synthetic crystals when compared to natural crystals (Harting, 1948). However, this is considered negligible for the current studies. Refractive indices were retrieved for the dry NaCl aerosol in the range 2000–8000 cm^{-1} (figure 6.8). No refractive index data is shown below 2000 cm^{-1} due to a low absorption signal in the measurements in this region. The peak at approximately 3450 cm^{-1} is attributed to water. While the RH of the sample was measured at $0 \pm 2\,\%$[2], the aerosol originated as wet particles that were subsequently dried, and this may account for the O-H stretch feature at this point in the spectrum. This feature was also later found in the spectra of SSA particles. Overall, the retrieved refractive indices show excellent correlation with the current data, with the retrieved values fitting the current data well within the error over almost all of the spectral range analysed.

6.4 Summary

- Application of the retrieval algorithm to simulated measurements determined that convergence to a solution was dependent on the a priori information regarding the band parameters.

---

[1] These include the algorithms written to complete the background removal, smoothing and gas retrieval processes before refractive index retrieval can begin.

[2] This value was measured during the experiment using a Honeywell relative humidity sensor placed at the entrance of the aerosol cell. Subsequent gas retrievals from the spectra also indicated an RH value of 0 %.

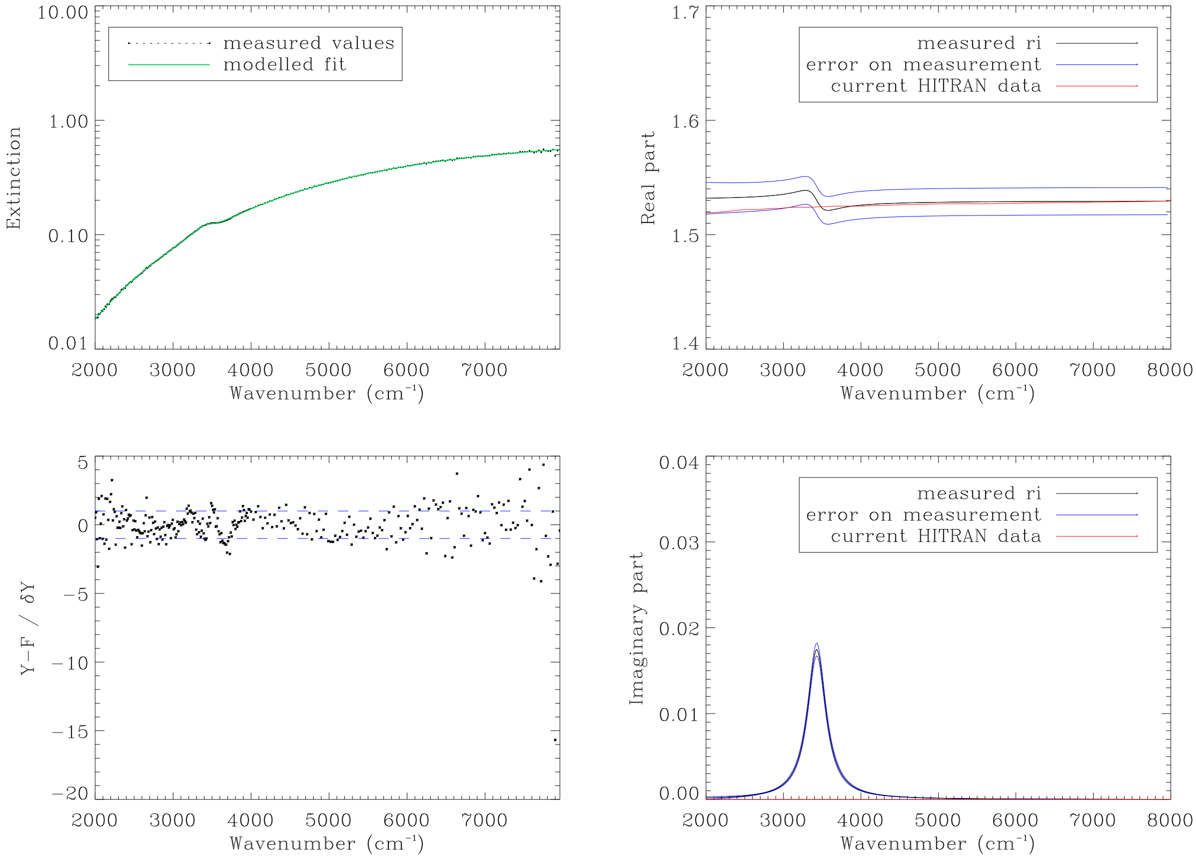

Figure 6.8: Refractive index retrieval output for dry NaCl aerosol data. $M_{500} = 1.53$, particle radius= $0.45\,\mu$m. It should be noted that most of the measured values in the extinction plot are not visible as they are almost completely obscured by the modelled fit. The difference between the modelled and measured values is given in the residual plot below the extinction.

- Further analysis suggested that the refractive index could be retrieved well providing that a good first guess of the position of the bands was given.
- A retrieval of the refractive index spectrum of sodium chloride from measurements of dry aerosol showed good agreement with the current data, within the error bounds. This provides independent validation of the retrieval.

Chapter 7

Sea Salt Aerosol

The extinction spectra of sea salt aerosol were calculated from transmission measurements over the wavenumber range $450 - 8000\,\mathrm{cm}^{-1}$, at an average resolution of $4\,\mathrm{cm}^{-1}$. Some spectra were recorded at a higher resolution (approximately $0.2\,\mathrm{cm}^{-1}$) but no finer structure was visible due to this higher resolution, other than at those places in the spectra where gas lines were present. Measurements of transmission were made up to $2 \times 10^4\,\mathrm{cm}^{-1}$ at much lower resolutions solely to provide a value for m at as high a wavenumber as possible. No complex refractive index retrievals were performed in this wavenumber range.

7.1 Aerosol Extinction

The retrieval algorithm fits extinction curves from the measured data. Figure 7.1 shows a plot of sea salt extinction calculated from measurements (green line) compared to the extinction calculated from current knowledge of sea salt refractive indices (black line), obtained from the HITRAN database (Rothman, 2005). This data is based on measurements taken by Volz (1972), and subsequent models based on the Volz data, produced by Shettle and Fenn (1979). The extinction was calculated using the forward model from the refractive index retrieval algorithm combined with size and number density measurements from experimental data.

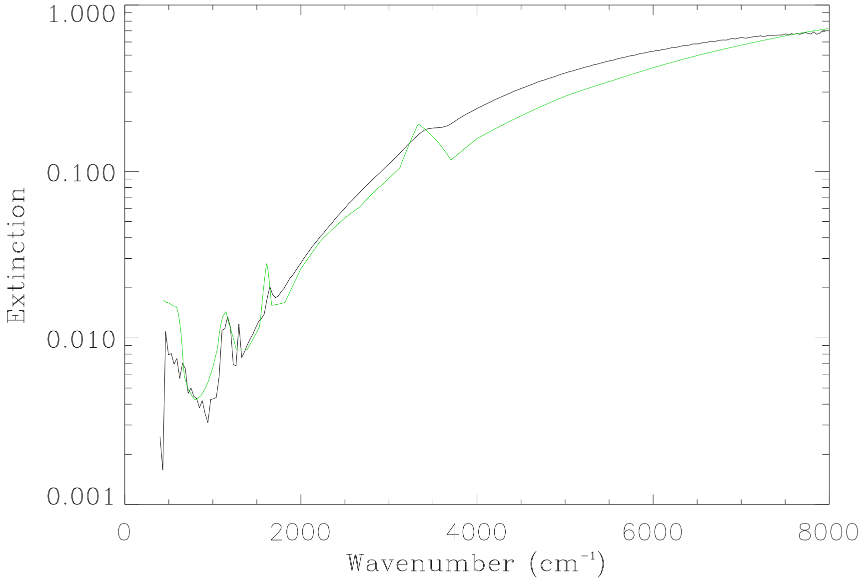

Figure 7.1: Sea salt aerosol extinction from HITRAN data (green) and measurements from RAL (black).

There is a clear similarity between the extinction curves shown in figure 7.1. However, the HITRAN data is based on far fewer points (60 data points rather than the ~2000 points in the new data) and does not show the peak at ~1300 cm^{-1} that is evident in the experimental data. This peak is also present in the infrared extinction spectra of seawater (Cziczo et al., 1997), and both NH_4HSO_4 and NH_4NO_3 which are component compounds of sea salt (Cziczo and Abbatt, 2000). The peaks at ~1645 cm^{-1} and ~3425 cm^{-1} are also much larger in the HITRAN data. The positions of these peaks correspond to the positions of peaks expected due to water features. However, the peak at $\sim$3425 cm^{-1} is quite symmetric in the HITRAN curve. This peak corresponds to an asymmetric OH stretch region. Since there was contradictory information in the original investigation regarding the amount of water in the sea salt samples analysed (as discussed in section 1.4.3) it is likely that this peak is due to excess water in the sample, and the symmetry of the shape is due to poor resolution[1]. Finally the extinction curve of the HITRAN data tends towards a much lower extinction value at high wavenumbers than the data from the experiment. These differences give additional justification to the decision to make additional measurements of the optical properties of sea salt.

7.2 Band Parameters

The retrieval code was altered to retrieve band parameters from the refractive index data from HITRAN. It was anticipated that these would provide the basis of the a priori state vector for retrievals from the sea salt experimental data. However, attempts to retrieve band parameters from the original data proved unsuccessful, indicating that the real and imaginary parts of the refractive index data from HITRAN did not correspond according to the equations used to relate these parameters in the CDHO model (Thomas et al., 2004). These equations are known as the Kramers-Kronig relation. Further investigation into the origin of these refractive indices is therefore required. Nevertheless this too provides justification for further measurements of the optical properties of sea salt aerosol.

The eventual a priori band set was built up by the inclusion of expected absorp-

---

[1] As mentioned in section 1.4.3 the average resolution of the Volz data is approximately 87 cm^{-1}. However, in the O-H stretch region, between 3000 and 3800 cm^{-1}, the resolution is at approximately 160 cm^{-1}.

Origin	Position (cm^{-1})	Width (cm^{-1})	Strength (cm^{-2})
Water	351.5	168.4	438015
Water	607.7	277.9	207943
NaCl	1146.8	140.3	10706
Possible nitrate peak	1447.5	376.7	70858
NaCl	1643.4	86.4	109899
Water	2094.3	251.9	39014
OH-stretch region	3470.8	152.1	1137066

Table 7.1: Band parameters for 74% RH sea salt aerosol. The compounds with which the bands may be associated are also given in the table.

tion bands from prior knowledge, and the addition and removal of subsequent bands based on a trial and error method. Prior knowledge of expected absorption bands came from current data on the infra-red absorption features of the component compounds of SSA available in the literature (Cziczo et al., 1997; Cziczo and Abbatt, 2000). Band parameters are described in terms of position, width and strength. The position refers to the wavenumber position of the oscillator centre, the width is the damping constant and the strength gives the maximum intensity of each band described by the CDHO model. Table 7.1 shows the set of band parameters for 74 % RH sea salt aerosol. As the RH of the aerosol increased, the size and width of the parameters corresponding to water bands increased. The aerosols measured were always dried to approximately 0 % RH and then re-hydrated to different RH values in order to avoid hysteresis effects.

Tables listing the complete sets of band parameters retrieved for all the SSA refractive index retrievals performed are given in appendix D.

7.2.1 Particle Size and Number Density

The complex refractive index of an aerosol varies significantly with particle size. Small particles will cause less light extinction than larger particles, resulting in smaller overall values for the refractive indices. A sample of small aerosol particles with a high particle number density may produce a similar extinction spectrum to a sample of large aerosol particles with a low particle number density. However, the refractive index spectra of these samples will be very different. It is therefore important to ensure that the correct values for particle size and number density are retrieved to differentiate between these two possible scenarios. Thus the independent measurements made using the Aerosizer and GRIMM SMPS+C instruments were crucial.

These measurements were used to provide a priori data. The aerosizer was primarily used for size measurements whilst the GRIMM instrument was used primarily for measurements of particle number density. This was primarily due to malfunctions of the DMA column during measurement. Figure 7.2 shows an example of the data obtained from the aerosizer instrument. The aerosizer instrument also measures particle number density, as shown in the plot. However, the GRIMM CPC provides a more frequent and accurate measurement of the number density than the aerosizer, which takes infrequent measurements. In addition the accuracy of the aerosizer number density count is compromised at high number densities due to saturation of the instrument.

Figure 7.3 shows an example of the aerosizer size distribution measurement. The aerosizer measures the number density of particles within specific size ranges and produces a normalised histogram output. Each measurement is taken over a

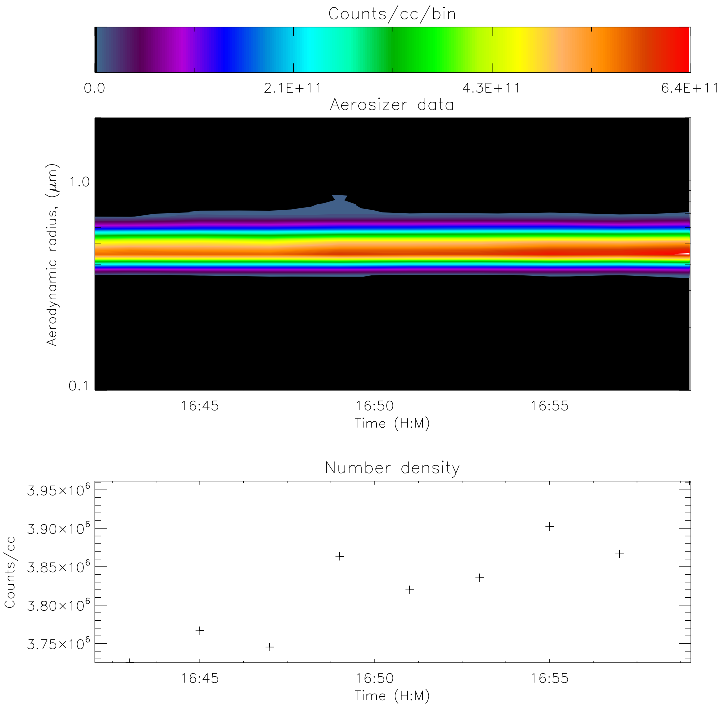

Figure 7.2: Aerosizer data for dry sea salt aerosol. The topmost plot shows the variation of the particle size distribution with time. The lower plot gives the aerosizer measurement of particle number density.

two minute sampling time period, and continuous measurements are taken over the course of each experiment. A lognormal distribution is fitted to the averaged result. As mentioned in section 3.3.1, the aerosizer has a practical size cut-off of approximately 0.3 μm. This means that it only provides the upper half of the size distribution, and the measurement count tails off rapidly at low radii. Thus the lognormal curve is fitted only to the distribution from the peak values upwards. Figure 7.4 shows a close up of the measurement in figure 7.3, this time as a line graph

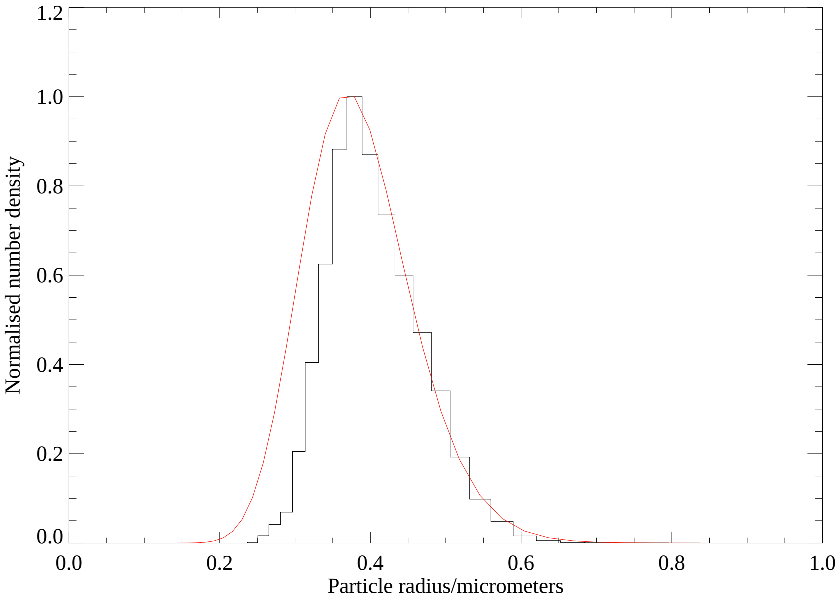

Figure 7.3: Averaged aerosizer output for dry sea salt aerosol. The red line shows a lognormal distribution fitted to the data with a modal size of 0.36 μm.

using the centre of each size bin to represent the particle radius. Upper and lower error bounds for the size distribution have been calculated using the variance of the aerosizer measurements taken over the course of the 30 minute spectral measurement. The lognormal distribution is clearly within the error bounds for the majority of the size range.

7.2.2 Modelling Particle Size

The modal values of the size distributions were used to represent the particle size for measured spectra of the 0.4 %, 22.9 %, 38.5 % and 48.9 % RH aerosols. For the aerosol samples above these RH values, no size information was available due to instrument malfunctions. These size measurements were therefore used in conjunction

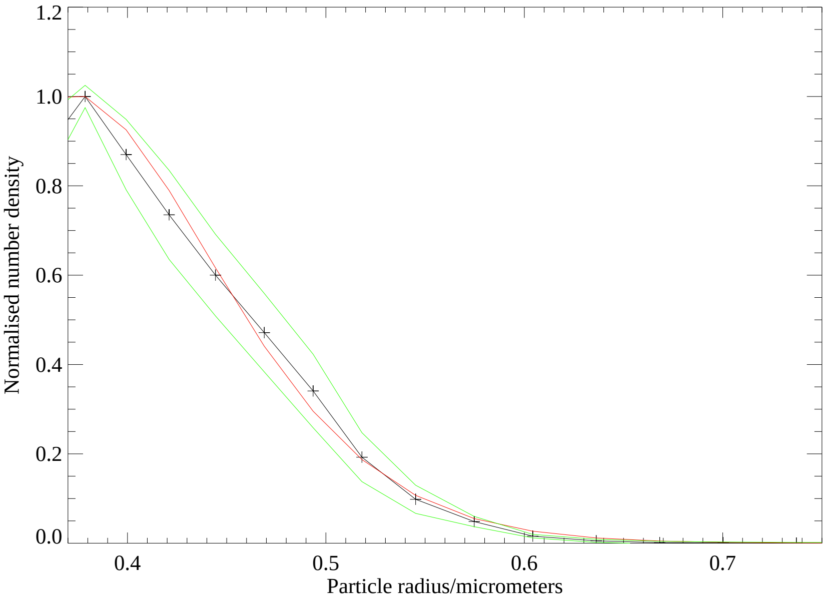

Figure 7.4: Close up of the measurement in figure 7.3. This time only the centre of each size bin is marked (black line and cross) and error bounds for these values are given in green. The red line once more shows the lognormal distribution fitted to the data.

with equation 7.1 to model the variation of SSA particle size with RH.

$$r_{RH} = r_{\text{dry}} \left(\frac{4.0}{3.7}\right) \left(\frac{2 - RH}{1 - RH}\right)^{\frac{1}{3}} \tag{7.1}$$

where r_{RH} is the particle radius at a particular RH and r_{dry} is the dry particle radius (Lewis and Schwartz, 2006). Equation 7.1 describes the radius of a sea salt aerosol particle at a given RH value as a function of the dry particle radius. This relationship describes the RH-dependent growth of SSA particles and therefore also neglects hysteresis effects.

The measured data is shown in figure 7.5, along with the models calculated using equation 7.1. Modelled sizes are calculated for the three RH values for which

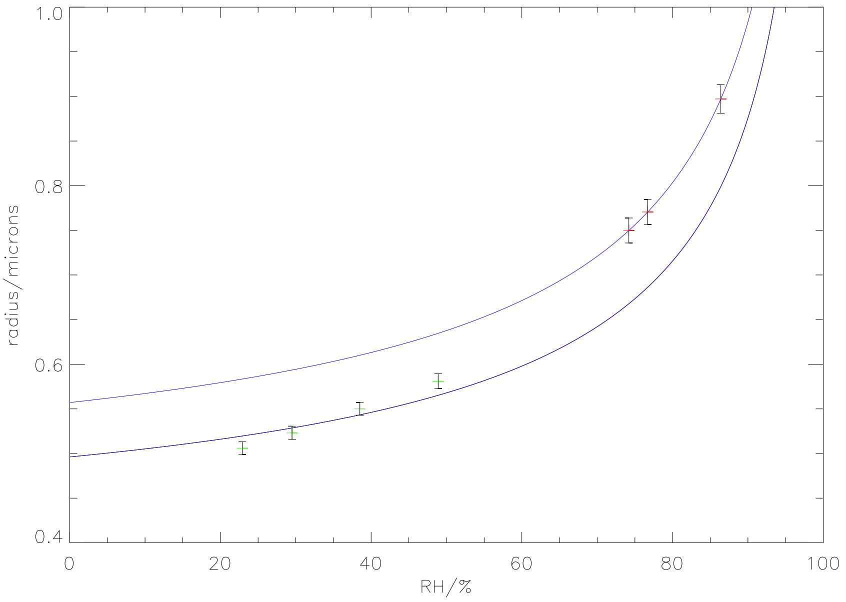

Figure 7.5: Variation of particle radius with RH for sea salt aerosol. The measured values are shown in green while the blue lines represent the modelled data. The red values are those taken from the model to provide an estimate of the aerosol particle sizes required where independent measurements were unavailable.

size data was unavailable (74.2 %, 76.7 % and 86.4 %). The model for this data is based on the measured dry size of particles created on the same day. The errors in this dry size were used to propagate the errors for the modelled sizes. These were then provided as a priori data for the refractive index retrieval. The two curves in figure 7.5 correspond to different equivalent dry sizes for the particles measured. The lower curve shows the modelled fit to size measurements taken using the aerosizer. The concentration of the solution that was nebulised to produce the aerosol for these measurements was lower than the concentration of the solution nebulised to create aerosol for the measurements made. This meant that, once the aerosols had passed through the diffusion dryers, they resulted in dry particles of different sizes, which were then rehydrated to specific RH values. The concentration of the solution used to produce the aerosols at 74.2 %, 76.7 % and 86.4 % RH was the same as that used to produce an aerosol at 0.34 % RH[2], which was assumed to be effectively dry. The size distribution of this dry aerosol was measured using the aerosizer and was therefore used to determine the position of the modelled size curve for the aerosols as the three highest RH values, for which there was no aerosizer data. Thus the upper curve refers to aerosol with an equivalent dry size of approximately 0.41 μm, while the lower curve corresponds to aerosol with an equivalent dry size of approximately 0.36 μm.

7.3 Molality

Two iterations of the refractive index retrieval were performed on this data in total. A first order approximation of the refractive index was obtained by using concomitant measurements of size and number density as a priori information for the retrieval. From this, the variation with molality[3] of the refractive index at a fixed point could be derived. At high wavenumbers, the real part of the refractive index tends towards a constant value. The refractive index at $2 \times 10^4\,\mathrm{cm}^{-1}$ (500 nm) was used to represent this value, as this was the highest wavenumber at which measurements were taken. These m_{500} values are shown in figure 7.6. A cubic interpolation was then performed on this data to provide a model from which fixed index values could be derived for use in the final refractive index retrieval. The equation of the

---

[2] The transmission spectra for this measurement were not included in the final refractive index retrieval as the transmission data for the 0.4 % RH SSA exhibited a better signal to noise ratio. This latter data was therefore chosen to represent dry SSA.

[3] Molality is the concentration of a solution defined as the number of moles of solute per unit mass of solvent.

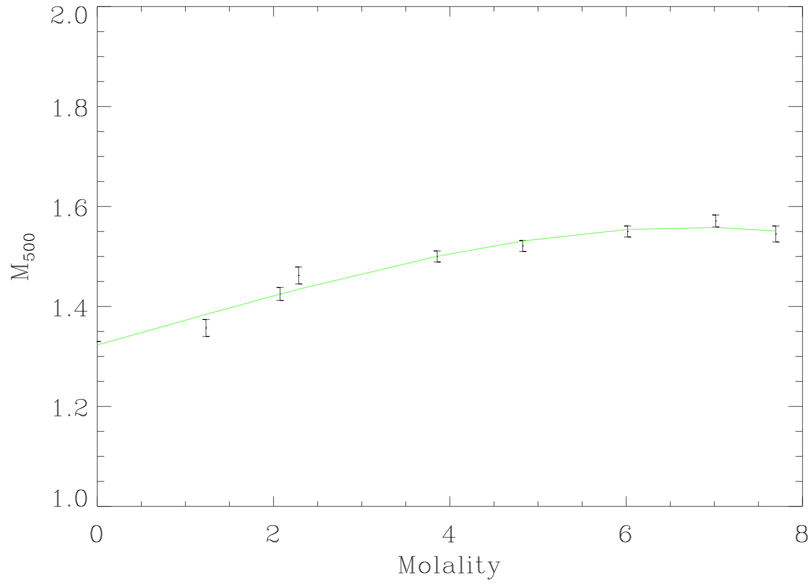

Figure 7.6: Variation of m_{500} with molality for sea salt aerosol. The initial point at 0 molality is that of pure water and is included for comparison.

curve fitted to the data points is $y = ax^3 + bx^2 + cx + d$ where $a = -4.41 \times 10^{-4}$, $b = 1.39 \times 10^{-3}$, $c = 4.51 \times 10^{-2}$ and $d = 1.33$.

7.4 Dry Aerosol Results

The results of the refractive index retrieval for dry sea salt aerosol are shown in figure 7.7. The retrieved particle size is 0.355 μm, which is very close to the size measured by the aerosizer (0.36 μm). The retrieved spectrum shows greater detail than the HITRAN data due to a higher resolution. However, the real part of the refractive index, m, from the experimental data looks very different to that presented by HITRAN. These data were originally obtained by reflectance measurements (Volz, 1972), rather than from transmittance measurements. As previous attempts to retrieve band parameters determined that the real and imaginary parts of the refractive index data from HITRAN do not correspond (see sections 7.1 and 7.2), the significant differences between the experimental and HITRAN data for the real part of the refractive index for dry sea salt are unsurprising. The new retrieved

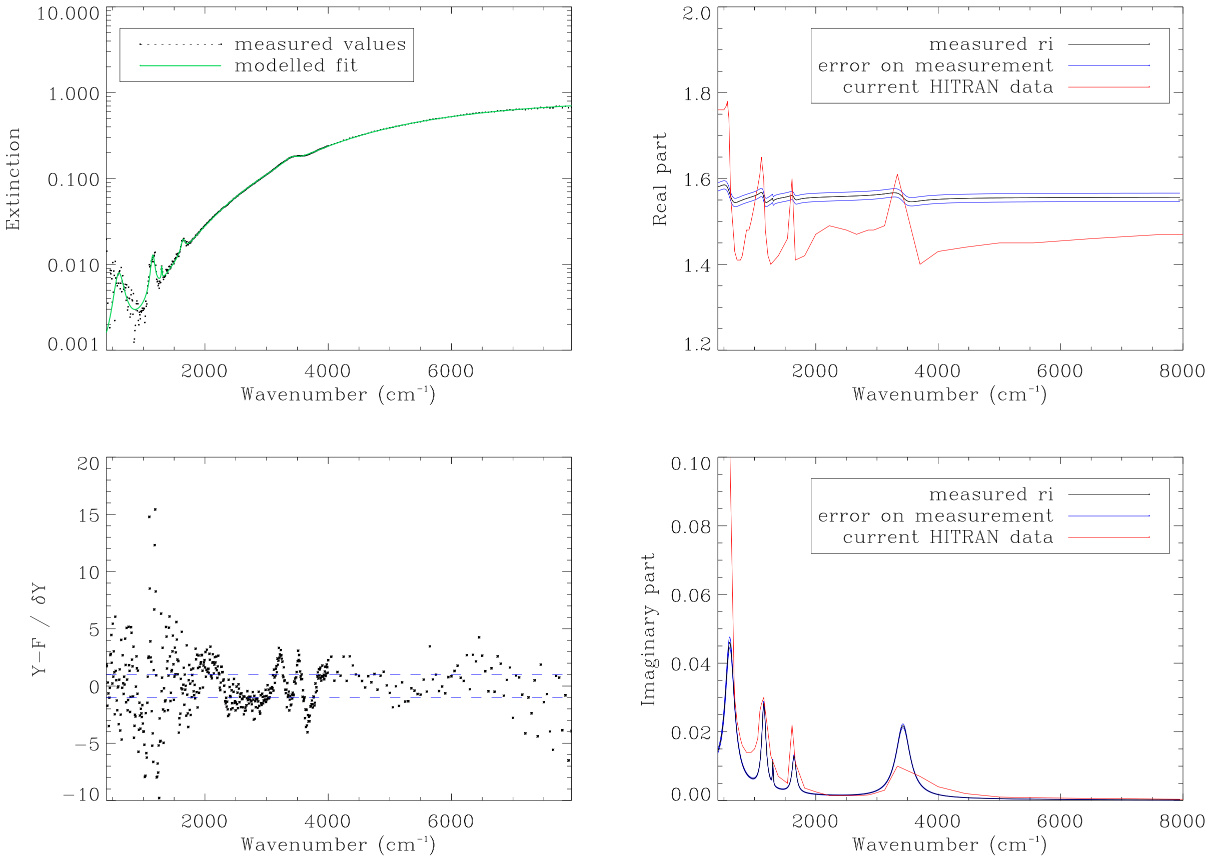

Figure 7.7: Refractive index retrieval output for dry sea salt aerosol. $M_{500} = 1.56$, particle radius$= 0.355\,\mu$m

real values are relatively constant, although slight disturbances are observed at the wavenumber values where peaks are evident in the HITRAN data. Two of these peaks are expected to be the result of water at $\sim$1625 cm^{-1} and $\sim$3430 cm^{-1}, and these were evident in the extinction graph (figure 7.1). It was noted in chapter 1 that there was some ambiguity as to whether the sea salt samples used for the original refractive index measurements remained dry. The presence and size of these water peaks confirms that there was more water in the bulk sea salt sample measured by Volz (1972) than in the aerosol samples produced and measured for this thesis.

Once more, there is evidence of a slight disturbance at $\sim$1350 cm^{-1} which suggests the presence of an additional peak here, undetected by HITRAN. As mentioned earlier, this peak is not present in the HITRAN data, but is present in the FTIR extinction spectra of seawater (Cziczo et al., 1997) as well as in the spectra of NH_4HSO_4 and NH_4NO_3, components of sea salt (Cziczo and Abbatt, 2000). The retrieved values of the imaginary part of the refractive index, k, follow the shape of the HITRAN data but again, the additional peak at $\sim$1350 cm^{-1} is evident. The greatest difference between the new data and the current HITRAN data is the increased magnitude of the real part of the new data. The imaginary parts of both the new and the current HITRAN data tend to zero at $\sim$7000 cm^{-1}.

The retrievals of water lines from these new measurements of dry sea salt aerosol indicate a relative humidity value of 0.4%, which is assumed to be negligible for this analysis as minimal water features are observed in the retrieved refractive index spectrum.

7.5 Wet Aerosol Results

The measured refractive indices of 49% and 86% RH sea salt aerosol are shown in figures 7.8 and 7.9 respectively for further comparisons with the current data from HITRAN. Once again the magnitude of both parts of the measured refractive

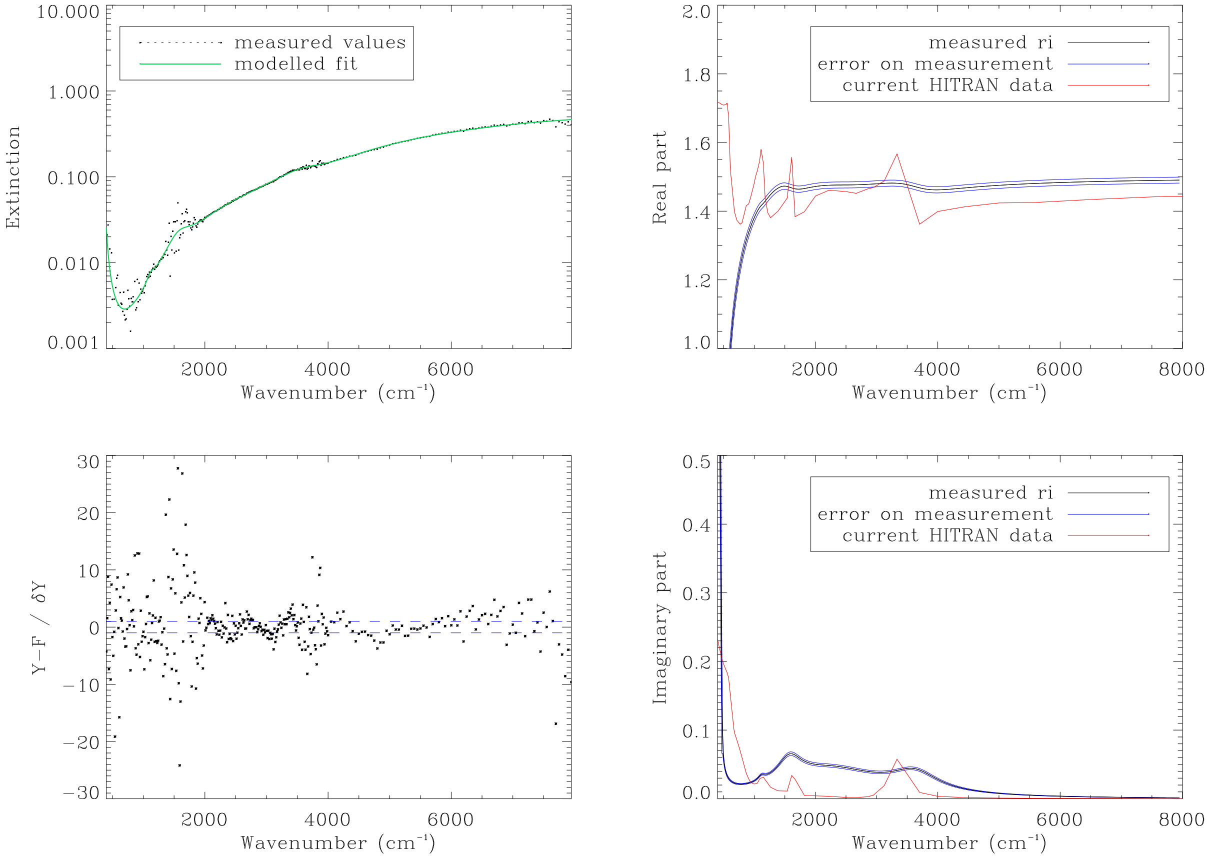

Figure 7.8: Refractive index retrieval output for 49 % RH sea salt aerosol. $M_{500} = 1.50$, particle radius= 0.573 μm

indices are greater than the magnitude of the current data, although this difference becomes smaller as the RH increases. At 49% RH the peaks of the real part of the HITRAN data are greater in amplitude and better defined than those of the new measurements, suggesting a greater level of water than in the aerosol produced for the new measurements. The HITRAN data also show a peak at ~400 cm^{-1} in the real part of the refractive index that is not present in the new measurements. However, this peak does appear in the new measurements of 86% RH sea salt aerosol, suggesting that it is due to a high water content. The new 86% RH measurement

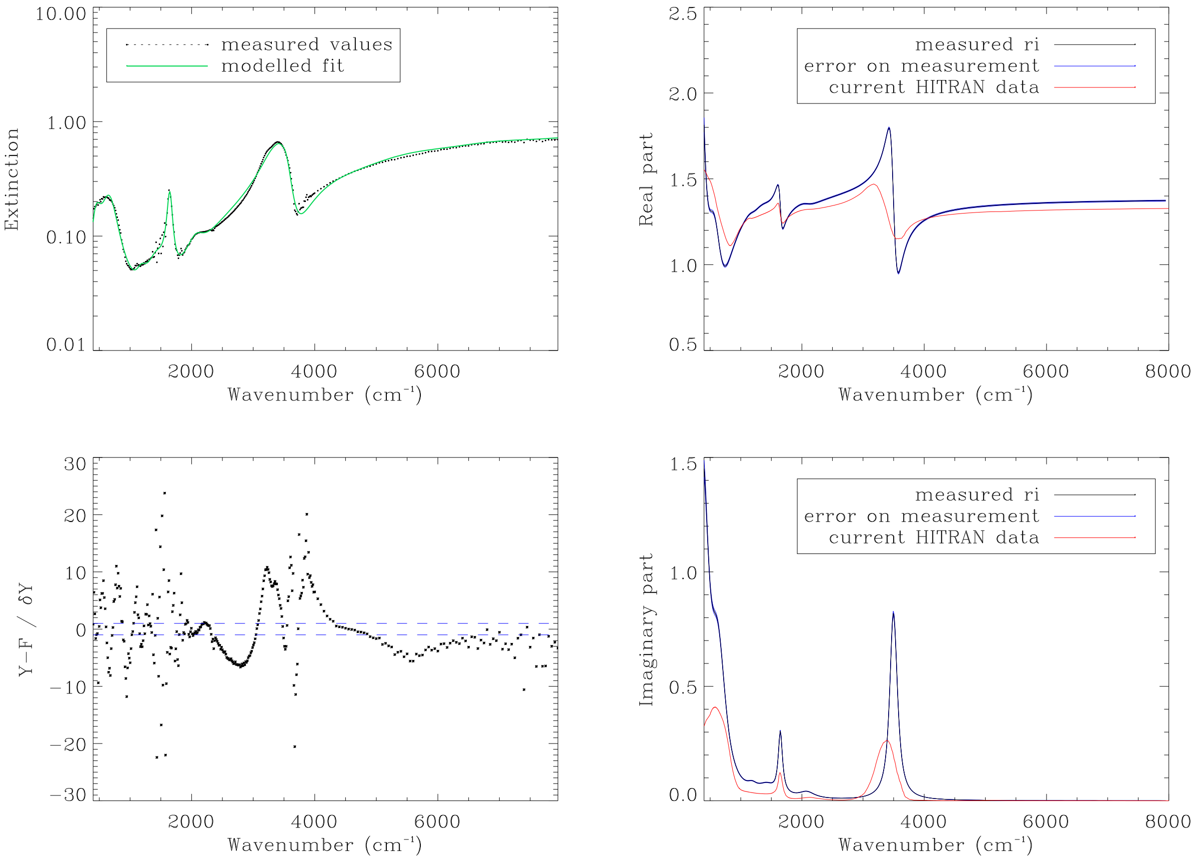

Figure 7.9: Refractive index retrieval output for 86 % RH sea salt aerosol. $M_{500} = 1.39$, particle radius= $0.897\,\mu$m

also shows much more structure in both the real and imaginary parts than the current HITRAN data. The peaks at $\sim$1625 cm^{-1}, $\sim$2000 cm^{-1} and $\sim$3430 cm^{-1} are all attributable to water, and the increased resolution of the new measurements compared to that of the original Volz (1972) measurements allows the structure of the peaks to be better defined. However, the scattering of data points around $\sim$1625 cm^{-1} in the new data indicates remnants of water lines that may provide an additional source of error. Therefore more work is necessary to improve the method of eliminating gas lines. The amplitude of these water peaks is much greater in the new measurements than in the HITRAN data. Also the large O-H stretch feature at ~3330 cm^{-1} in the HITRAN data is centred at the slightly higher wavelength of ~3430 cm^{-1}, although the positions of the remaining peaks remain unchanged between the two data sets. Currently the O-H stretch feature is modelled using a number of overlapping bands. This is due to limitations of the CDHO model that require absorption bands to be symmetric. However, it is anticipated that further work on the model may include an asymmetry parameter to better model this feature.

The differences between the new measurements and the current data were anticipated in chapter 1. These differences are attributed to the inaccuracy of the volume weighting model used to calculate the refractive indices in the HITRAN data. The possible presence of water and the apparent inconsistencies between the real and imaginary parts of this refractive index data is also a source of error.

7.6 Variation With Increasing Relative Humidity

At high wavenumbers, the real part of the refractive index for sea salt aerosol tends towards a constant value (figures 7.7, 7.8 and 7.9). As the water content of the aerosol increases, this value decreases (figures 7.8 and 7.9). This is to be expected as more water is present in the aerosol and so its refractive index should become closer to that of water (1.33 at 500 nm). This is particularly noticeable in the variation of the refractive index at 500 nm (m_{500}) shown in figure 7.6. The final retrieved parameters for all of the sea salt aerosol retrievals are given in table 7.2.

Figures 7.10 to 7.11 show the retrieved refractive index spectra for sea salt aerosol at six different RH values. For the three data sets at 22.9, 29.5 and 38.5% RH, no

RH (%)	Molality	m_{500}	N_0 ($\times 10^6$ cm^{-3})	R_m (μm)	S
0.4	7.697	1.557	3.806	0.355	1.379
22.9	7.016	1.562	0.469	0.499	1.166
29.5	6.016	1.555	0.639	0.516	1.156
38.5	4.827	1.530	0.756	0.543	1.142
48.8	3.856	1.499	0.676	0.573	1.161
74.2	2.285	1.434	0.385	0.764	1.171
76.7	2.074	1.425	0.543	0.756	1.239
86.4	1.234	1.386	0.526	0.897	1.010

Table 7.2: The RH, molality, m_{500}, number density, particle size and spread values for the sea salt aerosols produced and measured.

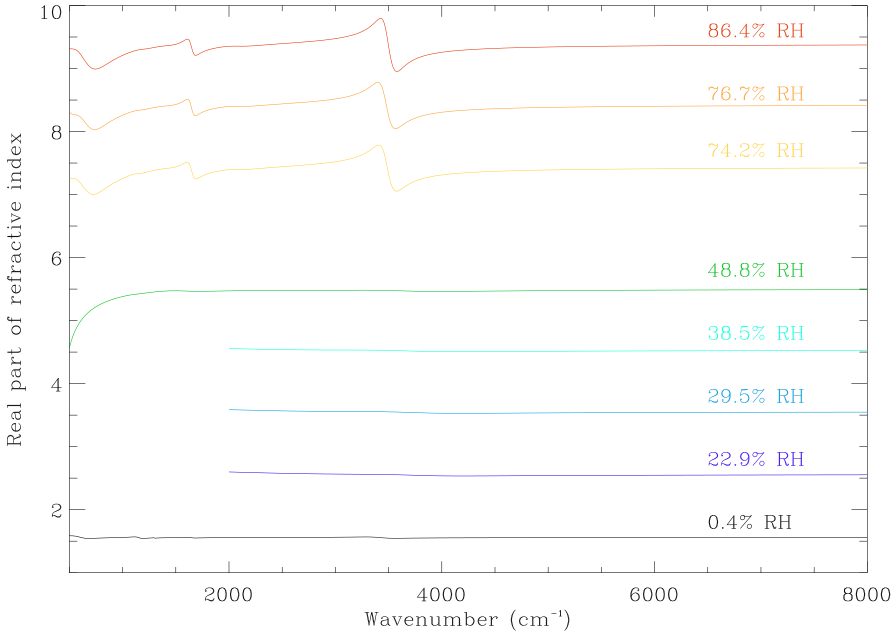

Figure 7.10: Variation of the real part of the measured refractive index, m with relative humidity. The 0.4% RH data are shown at the correct scale. Successive plots are displaced vertically by $+1$ unit each time, except the plot at 74.2 % RH which is at $+2$ to illustrate the difference between the RH of this sample and the one below it.

refractive index data is shown below 2000 cm^{-1} due to a low absorption signal in the measurements in this region. It can be seen that, in the real part of the refractive

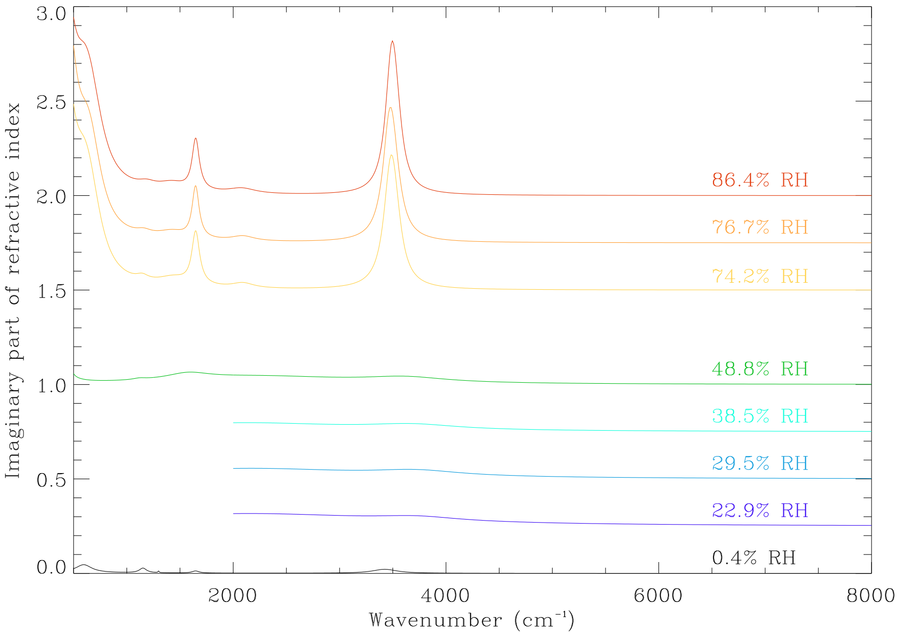

Figure 7.11: Variation of the imaginary part of the measured refractive index, k with relative humidity. The 0.4% RH data are shown at the correct scale. Successive plots are vertically displaced by +0.25 units each time except the plot at 74.2 % RH which is at +0.5 to illustrate the difference between the RH of this sample and the one below it.

index, the size of the O-H stretch feature at ∼3430 cm^{-1} increases with RH, as does the size of the peak at ∼1625 cm^{-1}. The imaginary part of the refractive index exhibits similar trends. The peak due to the O-H stretch from water at ∼3430 cm^{-1} grows significantly larger in amplitude as the RH increases, as does the peak at ∼1625 cm^{-1}. This is consistent with data from Weis and Ewing (1999) which showed similar trends in the O-H stretch regions for aqueous NaCl spectra with increasing RH. However, the peak at ∼1350 cm^{-1} disappears as RH increases, suggesting that it is due to the sea salt rather than water. The trough at ∼800 cm^{-1} in the real part of the data becomes deeper and more defined as the RH increases and the peak at ∼400 cm^{-1} begins to appear.

7.7 Volume Mixing Rules

The calculations performed by Shettle and Fenn (1979) used sea salt data from Volz (1972) and water refractive indices from Hale and Querry (1973). Further and more comprehensive measurements have been made of the refractive indices of water, most recently by Segelstein (1981). To confirm that the discrepancy between the new measurements and the refractive indices calculated by Shettle and Fenn (1979) are not merely due to inaccurate data for water, the volume mixing calculations are repeated here using the new measurements of dry sea salt aerosol, and the Segelstein (1981) data for the refractive indices of water. The refractive index spectrum for 74%

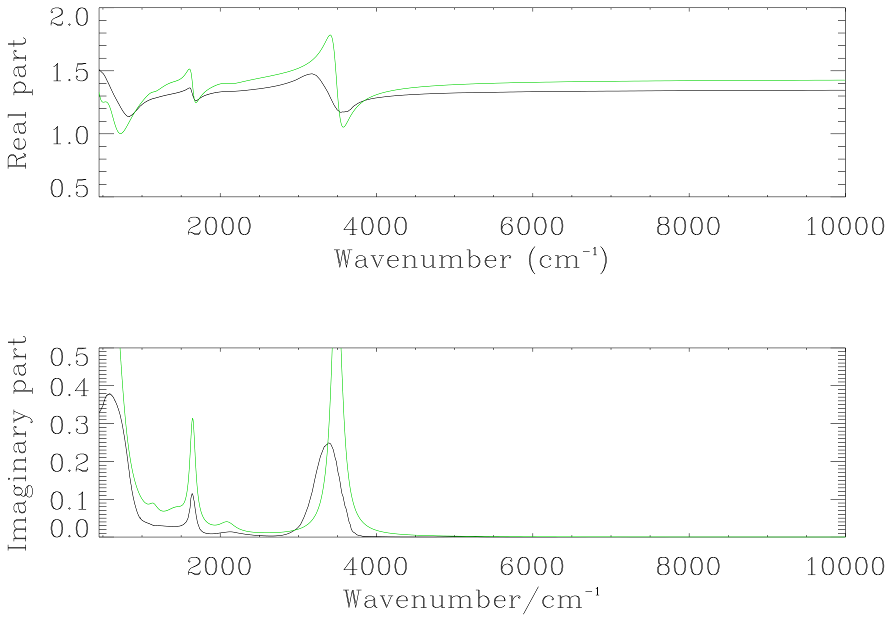

Figure 7.12: Refractive index spectra of 70% RH SSA from new, direct measurements (green), and calculated from the volume mixing rules using the newly measured dry SSA refractive index (black). The real part of the refractive index is shown in the top plot, and the imaginary part in the bottom plot.

RH sea salt aerosol was calculated using the volume weighting formula (following Shettle and Fenn, 1979):

$$n = n_w + (n_0 + n_w)\left[\frac{r_0}{r(a_w)}\right] \tag{7.2}$$

where n_0 is the refractive index of dry sea salt aerosol, n_w is the refractive index of water, r_0 is the dry aerosol particle size and $r(a_w)$ is the size of the wet sea salt aerosol for which the refractive index is required. The calculated refractive indices are compared with the new measurements in figure 7.12.

It is clear that, while the positions and shapes of the peaks are similar, the two refractive index spectra are sufficiently different that it may be assumed that the volume mixing rules used to calculate refractive index for wet aerosols provide an inaccurate result compared to direct measurements. This is expected as the dissociation of salt ions upon dissolution of the salt means that the resulting solution cannot merely be considered as a mixture of whole salt particles and water. Nevertheless, the implications of this result are considerable. A cursory enquiry into the number of studies performed using the volume mixed refractive indices of Shettle and Fenn (1979) alone on the Web of Science database (Thomson-Scientific, 2008) result in a total of 610 results, 23 of which are solely for work published in 2008. These include studies on the radiative forcing associated with sea salt aerosols (Li et al., 2008), the relationship between clouds, aerosols and meteorology (Loeb and Schuster, 2008) and aerosol climate effects and air quality impacts (Menon et al., 2008), all of which will have potentially erroneous results due to the inadequacy of the volume mixing rules.

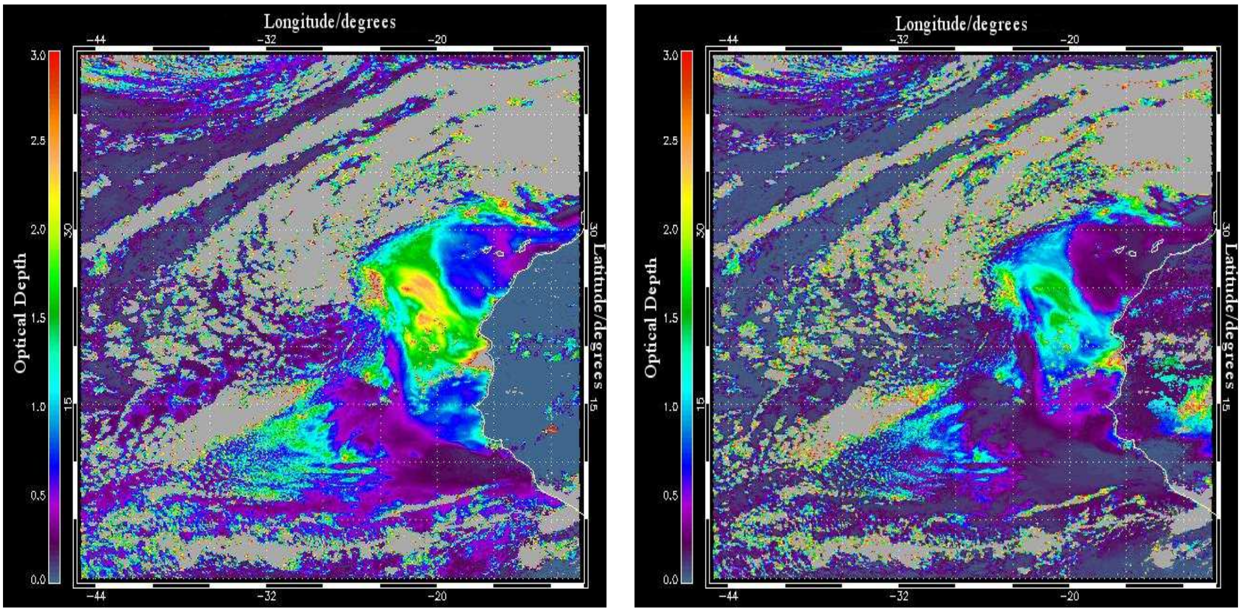

Figure 7.13: Aerosol optical depth retrieved from SEVIRI data using current sea salt refractive indices from HITRAN (left hand plot) and using new sea salt refractive indices (right hand plot). Latitude and longitude measurements are given in degrees.

7.8 Application of the New Data - Preliminary Results

The new refractive indices have been employed by Carboni (2008) in the retrieval of aerosol optical depth from satellite data collected by the SEVIRI[4] instrument. The retrieved data is for the 8th March, 2008, and is centred off the north-western coast of Africa. Figure 7.13 shows the preliminary results for aerosol optical depth over the Atlantic calculated using the old data from the HITRAN database and the same retrieval performed using the new sea salt aerosol refractive index data. Both retrievals assume a relative humidity of 50 %.

The variation of emissivity over land masses has not been rigorously accounted

---

[4] The Spinning Enhanced Visible and Infrared Imager carried aboard the Meteosat 2nd generation satellite.

for in these retrievals, thus the data over land is currently inaccurate. However, the outline of the landmass has been included to demonstrate the variability of aerosol optical depth off the coastal regions. The data clearly shows a decrease in the optical depth over the oceans of approximately 40 %. This suggests that the new refractive index data will also have a significant effect on global climate models.

7.9 Summary

- Comparison of the measured extinction of dry SSA with extinction calculated from current refractive index data shows a number of discrepancies which underline the requirement for new, higher resolution measurements.
- Attempts to retrieve band parameters from the HITRAN data proved unsuccessful as the real and imaginary parts of the refractive indices did not follow the Kramers-Kronig relations, as expected. This is not entirely unexpected as they were measured independently by two different methods. This also provides further justification for new measurements.
- An a priori set of band parameters was built from current infra-red absorption data on the component compounds of SSA.
- Particle size and number density measurements were used as a priori data for the refractive index retrievals. Lognormal distribution curves were fitted to the aerosizer data, taking into consideration the low-radius size cut-off of the instrument. All fitted distributions were well within the error bounds for the majority of the size ranges measured. Where size data was not available, the expected sizes were modelled using the parameterisation derived by Lewis and

Schwartz (2004) and any available measurements.

- The variation of the fixed index point m_{500} with molality was modelled and used to provide further information to improve the accuracy of the retrieval.
- The refractive indices of dry sea salt aerosol were retrieved, and shown to be significantly different to the HITRAN data. The new data showed smaller peaks in those regions of the spectrum specific to water features, when compared to the current data from HITRAN. This was expected as the original data was thought to have been compromised by the presence of water in the sample (see section 1.4.3).
- The refractive indices of wet sea salt aerosol were retrieved at seven different RH values. Significant differences to the current data were evident in all the spectra, which implied that the volume mixing rules used to derive the current data were inadequate, as suggested in chapter 1.
- To confirm the inadequacy of the volume mixing rules, these equations were applied to the newly measured refractive indices of dry SSA. The refractive index data for water was taken from Segelstein (1981), as these measurements superceded the data used for previous calculations of wet SSA, which were from Hale and Querry (1973). Comparisons of the volume-mixed data with the direct measurements show distinct differences. This confirms that the volume mixing rules are indeed inadequate for describing the refractive indices of solutions.
- Preliminary retrievals from SEVIRI data by Carboni (2008) show that the new data reduces the magnitude of retrieved aerosol optical depth, and suggest that

it will have a significant effect on satellite retrievals and global climate models.

Chapter 8

Additional Work

Due to the success of the experimental and retrieval techniques with sea salt aerosols, further studies were undertaken on a smaller scale on other aerosols of atmospheric importance.

8.1 Ammonium Sulphate & Ammonium Nitrate Aerosols

Ammonia is a major contributor in the formation of secondary aerosol in the atmosphere (Wayne, 1991) and reacts rapidly with sulphuric and nitric acids. It is primarily generated from agricultural livestock wastes and from fertiliser production and application (Buijsman et al., 1987). It is also emitted into the atmosphere from the oceans as a result of biological activity (Quinn et al., 1988).

Sulphates and nitrates compete for ammoniation and are the major sinks for ammonia in the atmosphere. Ammonia reacts with sulphuric acid to form ammonium bisulphate, which reacts with ammonia to produce ammonium sulphate aerosols.

These reactions with sulphuric acid and ammonium bisulphate are favoured so ammonium sulphate dominates over ammonium nitrate (Seinfeld and Pandis, 1998). Over the oceans the major source of biogenic sulphur to the atmosphere is dimethylsulphide (DMS), a by-product of phytoplankton emissions. The dominant oxidation product of gaseous DMS is sulphur dioxide, which eventually leads to the formation of ammonium sulphate. Common in both the stratosphere and the troposphere, ammonium sulphate can occur as a solid or in solution (Toon et al., 1976).

Sulphate particles are important as they are the largest contributors to the global anthropogenic accumulation mode aerosol mass budget. They are non-absorptive in the visible region of the electromagnetic spectrum and so provide a significant anthropogenic cooling contribution to global radiative forcing (Charlson et al., 1992; Adams et al., 2001; IPCC, 2007). Over polluted continental regions the direct forcing of sulphate alone can be as large as those of the combined greenhouse gases, but opposite in sign (Charlson et al., 1992; Kiehl and Briegleb, 1993). There is also a strong correlation between visibility degradation and sulphate mass concentration (Cass, 1979). In the troposphere, ammonium sulphate is the dominant sulphate aerosol and is therefore of great importance (Twomey, 1971; Nemesure et al., 1995). The IPCC rate the level of scientific understanding of sulphate aerosols as low, even though they are estimated to have a significant radiative forcing effect (figure 8.1).

Where there are fewer sulphur-based compounds present, for example in regions with fewer power plants like the Western US, the available ammonia is scavenged by nitric acid to form ammonium nitrate, becoming the important aerosol component (Jarzembski et al., 2003). Nitric acid is produced in the gas phase when OH oxidises NO_x. Ammonium nitrate is in equilibrium with $NH_3 + HNO_3$ and the partitioning between particle and gas is a strong function of temperature and relative humidity

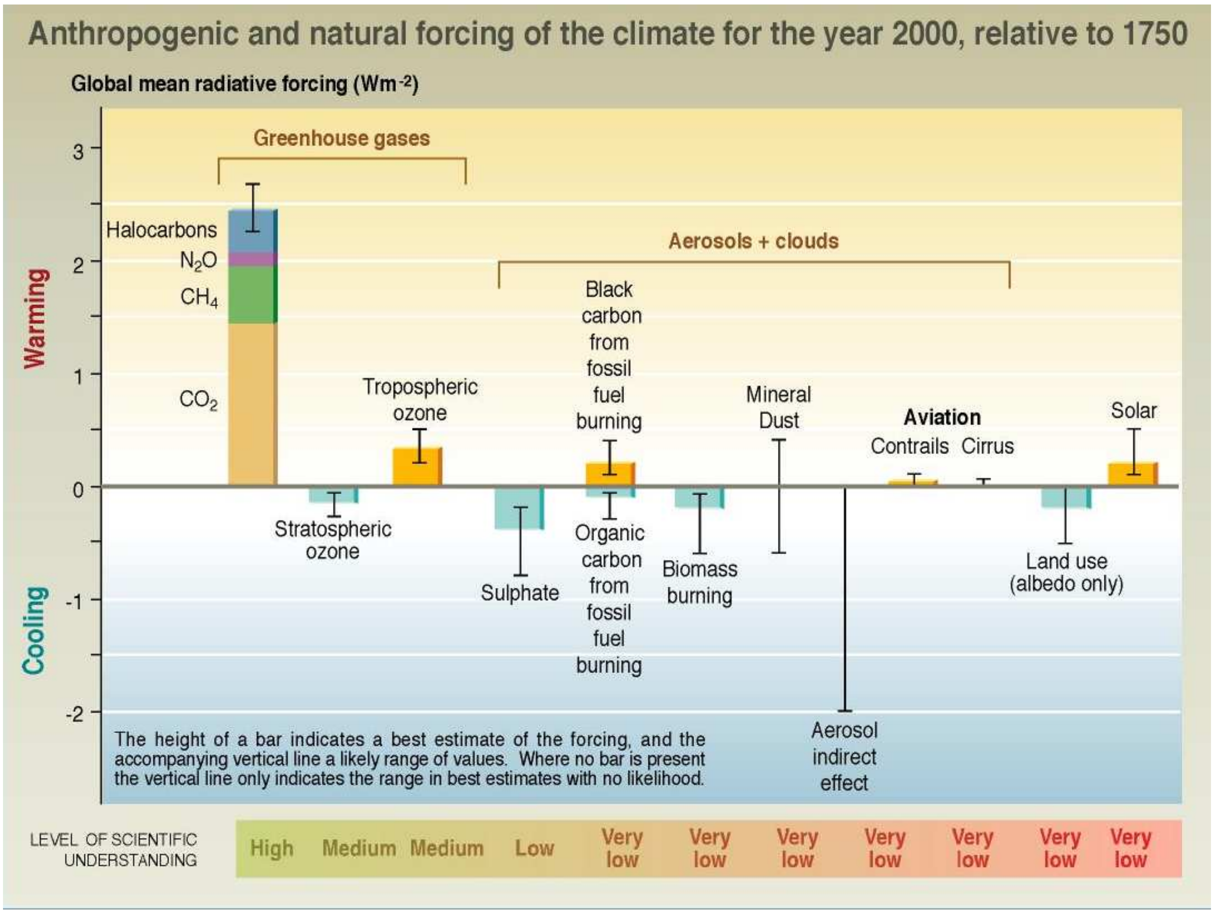

Figure 8.1: Current level of scientific understanding compared to the radiative forcing effect of various aerosols (IPCC, 2001).

(Lightstone et al., 2000). The formation of ammonium nitrate is encouraged by high nitric acid and ammonia levels, low temperatures and high relative humidity. Over the oceans, nitric acid and NO_2 reactions with sea salt create ammonium nitrate and release chloride gas into the atmosphere (Myhre and Grini, 2006).

Ammonium nitrate is considered to be a significant anthropogenic constituent of fine particulate matter of particle size 2.5 μm or less. This is considered to be of extreme impact to pollution and climate forcing and is considered a pollutant harmful to public health and the environment (Clean Air Act, 1990). Ammonium nitrate is common to urban areas (Marinoni et al., 2004) and can contribute substantially to total aerosol extinction on a regional scale. For example, in LosAngeles 10–15 % of aerosol mass in the accumulation mode is attributed to particulate ammonium nitrate (John et al., 1990). Over Europe nitrate particles account for about 10–20 % of the total aerosol mass (Putaud et al., 2004) and in winter in Western Europe, nitrate concentrations often exceeded those of sulphate (Schaap et al., 2002; ten Brink et al., 1997) (sub-micron nitrate is predominantly present in the form of ammonium nitrate). However, the IPCC report did not present a best estimate of the direct forcing by nitrate mainly because of a lack of reliable measurement data. Nevertheless, the importance of ammonium nitrate has been highlighted by recent global model studies (Adams et al., 1999; Metzger et al., 2002), and Adams et al. (2001) even suggested that by 2100 ammonium nitrate would be more important than sulphate with respect to aerosol radiative forcing.

8.1.1 Previous Measurements

While there has been a considerable amount of work done on these compounds, the optical properties of the aerosols have not been measured directly. Previous measurements of the refractive indices of ammonium sulphate have been carried out either using bulk samples, for example in the form of pellets (Volz, 1973) or on single suspended droplets that are much larger than the actual size of the tropospheric aerosol particle (Tang and Munkelwitz, 1994). It is therefore doubtful whether this data could be applicable to tropospheric aerosol. The current refractive index spectra for ammonium sulphate are available from the HITRAN database. Similarly, the refractive indices of ammonium nitrate have been measured using powders dispersed in Nujol, a mineral oil (Jarzembski et al., 2003).

To date all measurements have been made at room temperature and pressure. Although there is a general consensus that measurements over a range of temperatures are necessary, such measurements have not as yet been conducted. It is therefore doubtful whether the current data would be useful for optically modelling stratospheric aerosol (Volz, 1973). Measurements have been made at very few humidities, yet the physical state of these aerosols has a clear effect on their direct radiative forcing (Martin et al., 2004). There have also been many discrepancies in the measurements of optical properties of these aerosols and further work is therefore important (Remsberg, 1973; Volz, 1973).

A better understanding of the optical properties of these aerosols may also be helpful in the design of instruments used for measuring the aerosol distribution and for pollution monitoring. A series of experiments was therefore proposed to create and measure ammonium sulphate and ammonium nitrate aerosols in the laboratory. The transmission spectra of these aerosols was measured over a range of temperatures and humidities representative of the troposphere in order to compare the results of direct measurements of aerosol with the previous measurements of bulk samples. The measurements were made over a wavenumber range $900-8000\,\mathrm{cm}^{-1}$, at an average resolution of $4\,\mathrm{cm}^{-1}$. However, the quality of this data was not as high as that of the sea salt data.

8.2 Low Temperature Measurements

Measurements at low temperatures, i.e. lower than room temperature, were conducted on ammonium sulphate and ammonium nitrate aerosols over a range of relative humidity values. A small range of temperatures and RH values was used due to limited availability of time. A schematic representation of the experimental set-up used for the low temperature measurements is shown in figure 8.2. The set-up was similar to that used for the room temperature measurements, with the addition of a pre-cooler inserted between the conditioner and the aerosol cell. In addition to this, the aerosol cell itself had a cooling jacket, and an ethanol based cooling system

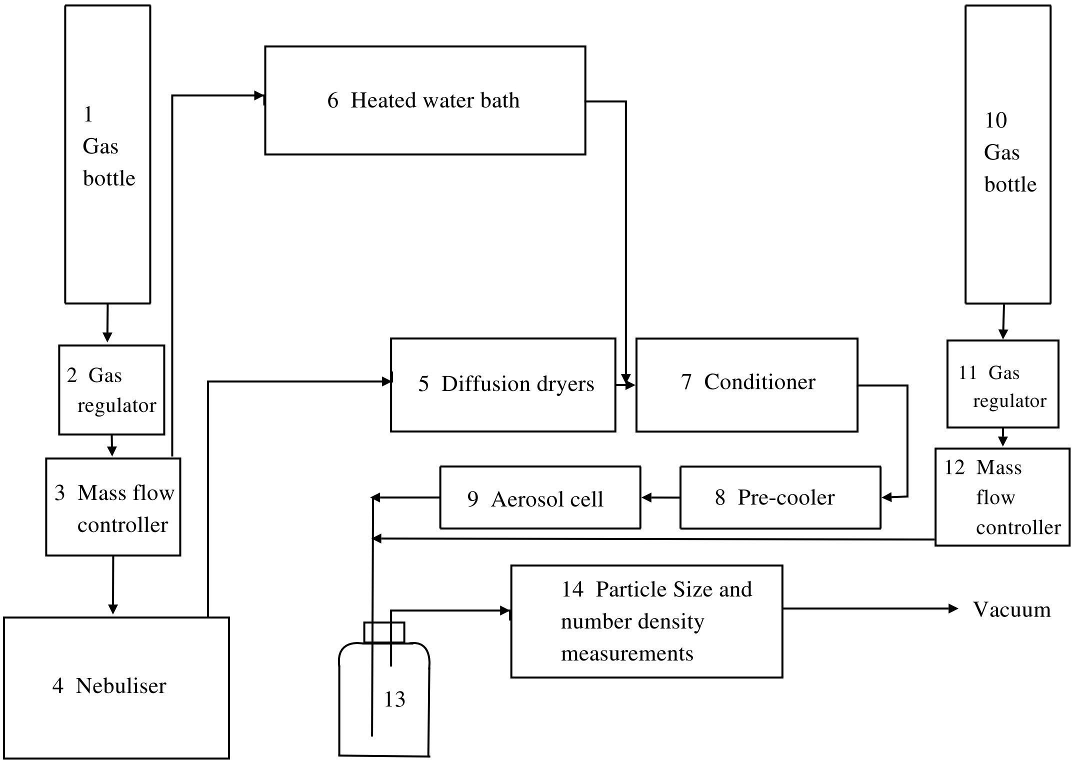

Figure 8.2: Overview of experimental set-up for low-temperature measurements. Part 13 is a dilution vessel required to dilute the aerosol flow to a suitable level for the particle sizing instruments.

was used to vary the temperature of the aerosol. The pre-cooler was designed to be used with the aerosol cell and was also constructed of double-walled stainless steel. It was of a size identical to the aerosol cell, which was sufficient to allow the aerosol to attain equilibrium temperature before entering the cell. Additional Vaisala temperature and RH sensors positioned at the entrance to the cell were used to provide further information on the aerosol.

A TOPAS diluter was initially used to replace the dilution bottle in the experiment for the ammonium nitrate and ammonium sulphate measurements. This is a device that provides an additional, dilution flow of buffer gas to the main experiment, in order to reduce the number density of aerosol particles reaching the particle sizing instruments. The advantage of this device over the dilution bottle was that it provided an accurate measurement[1] of the incoming and outgoing gas flows without the addition of extra mass flow controllers. However, this device proved to be highly inefficient and would regularly become clogged with aerosol. This caused the gas flow through the entire experiment to come to a stop. For the low temperature measurements, therefore, the TOPAS diluter was removed and replaced once more with the dilution bottle used for the sea salt measurements..

8.2.1 Detailed Procedure

The procedure for the low temperature experiments was identical to that of the room temperature experiments, with the following differences:

1. The temperature at which measurements were to be made was set at the beginning of each day. Having reached the required temperature according

---

[1] The TOPAS diluter provides a measurement of gas flow in terms of litres per minute, to the nearest tenth of a litre.

to the temperature sensor at the entrance of the aerosol cell, the system was allowed a further 30 minutes to equilibrate, during which time it was flushed through with nitrogen. This process was repeated if the temperature of the cell was changed at any point during the day.

2. If sufficient time remained at the end of the day, the temperature was increased to room temperature. The system was then given a further 30 minutes to equilibrate while being flushed through with nitrogen before an additional background measurement was taken.

3. If the temperature was increased from a lower to a higher temperature during a day when wet measurements were being performed, there was a high risk of water vapour condensing on the windows of the aerosol cell as ice crystals melted. This was immediately obvious in the spectral output of the spectrometer. Therefore, wherever possible, the temperature was kept constant on each day of the experiment, at a level determined at the start of the day. If any sign of water vapour condensate became evident in the spectra then the measurements were halted and the system was cleaned and flushed through with nitrogen before measurements recommenced.

8.3 Ammonium Sulphate Aerosol

Measurements of ammonium sulphate aerosol were made at room temperature, as well as at $-10\,^{\circ}$C, $-20\,^{\circ}$C and $-30\,^{\circ}$C. A small number of measurements were also taken at relative humidity values between 0 and 80 %. However, these were limited due to a shortage of available time at the RAL MSF, and as a result little useful information was obtained. However, useful comparisons were made of the extinction spectra of the dry aerosols, with the extinctions calculated from current data that was collected using bulk samples.

8.3.1 Dry Room Temperature Measurements

The current refractive index data for dry ammonium sulphate aerosol is available from the HITRAN database. This data was used to calculate an extinction curve for ammonium sulphate aerosol using the forward model of the retrieval algorithm. Figure 8.3 shows the extinction calculated from transmission measurements compared to the extinction calculated from the current refractive index data from HITRAN. When compared with figure 7.1, figure 8.3 clearly shows more noise in the

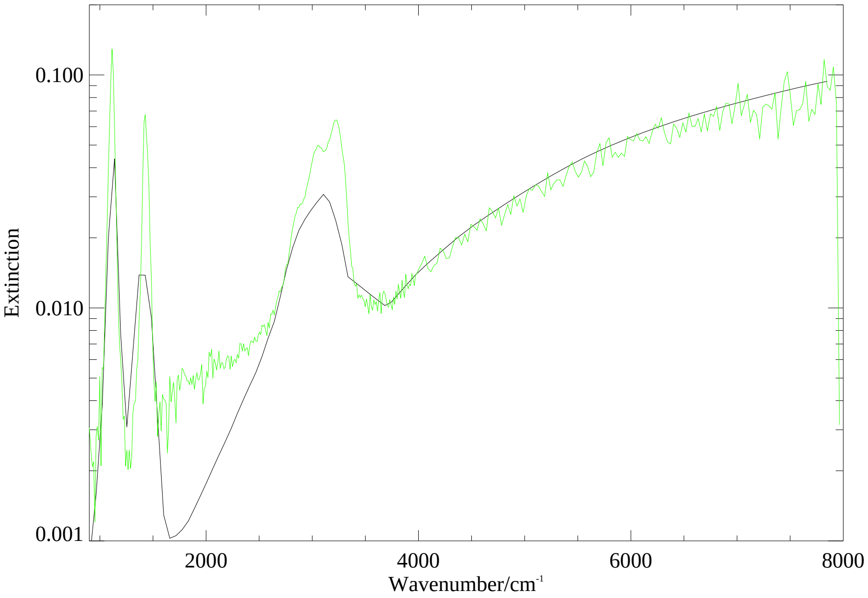

Figure 8.3: Ammonium sulphate aerosol extinction from HITRAN data (black) and measurements from RAL (green). Particle size $r \sim 0.5\,\mu$m, particle number density $N \sim 1.7 \times 10^5\,\text{cm}^{-3}$.

data. Nevertheless the main peaks corresponding to ammonium sulphate are clearly visible.

The scattering curve between 4000 and $8000\,\mathrm{cm}^{-1}$ closely follows that of the extinction calculated from the HITRAN data, which suggests that the particle size distributions set for the forward model are in good agreement with the measurements taken for this spectrum. However, below approximately $3500\,\mathrm{cm}^{-1}$ the measured extinction curve is much higher than the extinction calculated from HITRAN data. As a result, the peaks at $\sim 1100\,\mathrm{cm}^{-1}$, $\sim 1475\,\mathrm{cm}^{-1}$ and $\sim 3250\,\mathrm{cm}^{-1}$ all seem to have much higher amplitudes in the measured data than in the HITRAN data. Finally, the peak at $\sim 3250\,\mathrm{cm}^{-1}$ appears to have three very distinct turning points at its apex in the measured data, but the calculated extinction from HITRAN shows no such detail. This peak corresponds to the O-H stretch regions mentioned earlier in chapter 5. Several other measurements were made of dry ammonium sulphate aerosol which exhibited the same features evident in figure 8.3.

8.3.2 Dry Low Temperature Measurements

Measurements of dry ammonium sulphate aerosol were taken at $-10\,^{\circ}\mathrm{C}$, $-20\,^{\circ}\mathrm{C}$ and $-30\,^{\circ}\mathrm{C}$. Figures 8.4, 8.5 and 8.6 show the extinction spectra for measurements at each of these temperatures respectively, as well as the extinction calculated from current refractive index data, which was taken at room temperature. The measurements at $-10\,^{\circ}\mathrm{C}$ show a large amount of noise (figure 8.4). As a result of this, little detail is discernible at the lower wavenumbers. The main peaks are at similar positions in both datasets and have similar heights and widths. The shape of the scattering curve for the measured data closely follows that of the calculated extinc-

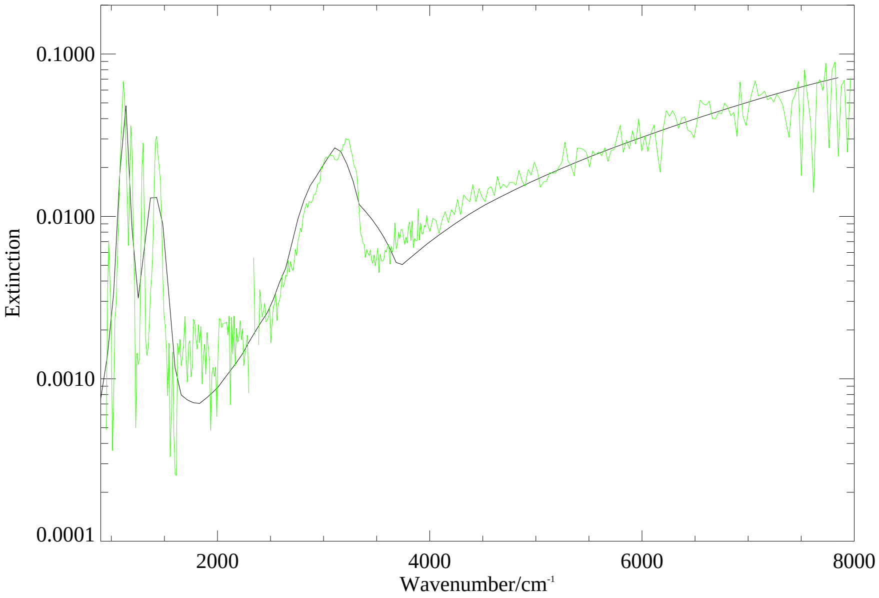

Figure 8.4: Ammonium sulphate aerosol extinction from current data taken at room temperature (black) and measurements from RAL taken at $-10\,^{\circ}$C (green). Particle size $r \sim 0.35\,\mu$m, particle number density $N \sim 5.3 \times 10^5\,\text{cm}^{-3}$.

tion. In addition there appear to be an additional peak appearing at $\sim 1750\,\text{cm}^{-1}$. However, the low signal to noise ratio makes it difficult to precisely separate the possible peak from the background noise.

The measurements at $-20\,^{\circ}$C show much less noise (figure 8.5) and the main peaks at $\sim 650\,\text{cm}^{-1}$, $\sim 1200\,\text{cm}^{-1}$, $\sim 1400\,\text{cm}^{-1}$ and $\sim 3200\,\text{cm}^{-1}$ are easily distinguishable. Again, the peak at $\sim 3200\,\text{cm}^{-1}$ appears to have three turning points at its peak in the measured extinction, but these features are not visible in the HITRAN data. The base value of the extinction from HITRAN data falls much lower than measured values below $\sim 3000\,\text{cm}^{-1}$. This feature was also present for the room temperature dry ammonium sulphate data, but is more exaggerated at $-20\,^{\circ}$C. Two additional small peaks are visible in the measured data at $\sim 1750\,\text{cm}^{-1}$

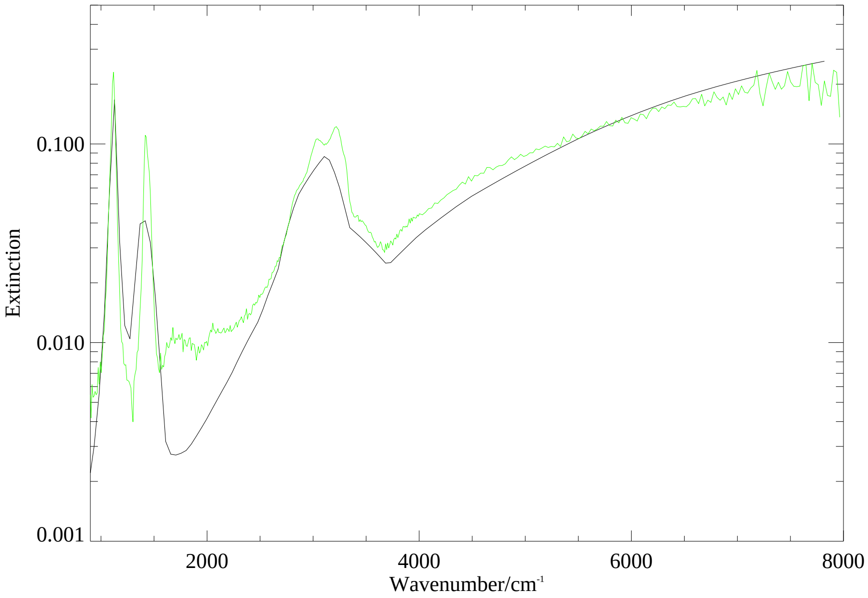

Figure 8.5: Ammonium sulphate aerosol extinction from current data taken at room temperature (black) and measurements from RAL taken at $-20\,°\mathrm{C}$ (green). Particle size $\mathrm{r} \sim 0.45\,\mu\mathrm{m}$, particle number density $\mathrm{N} \sim 7.0 \times 10^5\,\mathrm{cm}^{-3}$.

and $\sim 2100\,\mathrm{cm}^{-1}$ that are not visible in the data from HITRAN. One of these may have appeared at $-20\,°\mathrm{C}$, although the noise level means that it is difficult to resolve. Nevertheless, it does provide justification for further measurements at low temperatures.

The measurements at $-30\,°\mathrm{C}$ are incomplete below approximately $2000\,\mathrm{cm}^{-1}$. However, above this value, there is a high signal to noise ratio. The peak at $\sim 3200\,\mathrm{cm}^{-1}$ is clearly visible and appears to be much smaller and wider than for previous measurements. This may be due to trace residual water in the aerosol particles freezing and settling out before the aerosol reaches the cell.

In summary, there is little evidence to suggest that the refractive index of dry ammonium sulphate aerosol varies significantly with temperature over the range

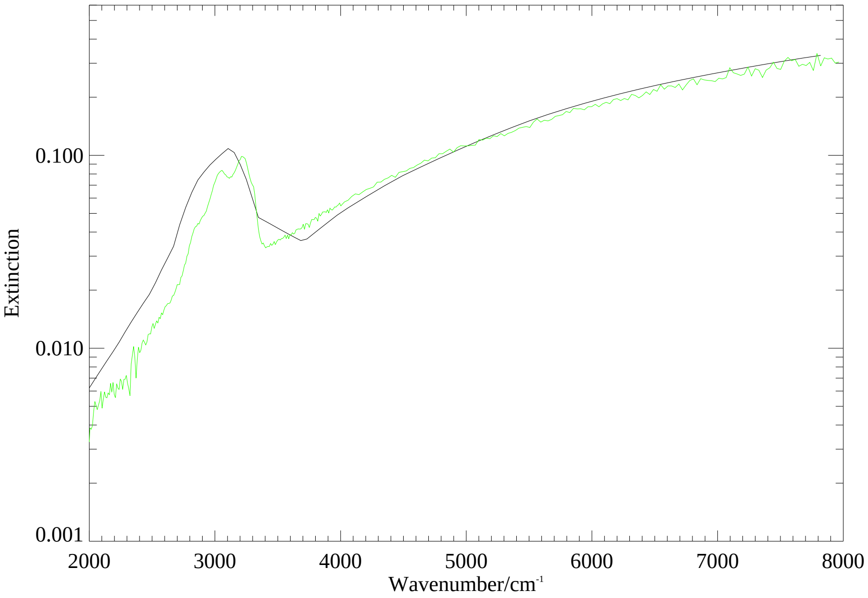

Figure 8.6: Ammonium sulphate aerosol extinction from current data taken at room temperature (black) and measurements from RAL taken at $-30\,^{\circ}$C (green). Particle size $r \sim 0.5\,\mu$m, particle number density $N \sim 6.0 \times 10^5\,\text{cm}^{-3}$.

$-30-25\,^{\circ}$C. However, the incomplete nature of the data at $-30\,^{\circ}$C means that detailed analyses of any trends in the far-infrared have not been possible.

8.4 Ammonium Nitrate Aerosol

Measurements of ammonium nitrate aerosol were made at room temperature, as well as at $-10\,^{\circ}$C, $-20\,^{\circ}$C and $-30\,^{\circ}$C. A number of measurements were also taken at relative humidity values between 0 and 50 %. However, these were once again limited due to a shortage of available time at the RAL MSF.

8.4.1 Dry Room Temperature Measurements

The current refractive indices for dry ammonium nitrate aerosol Jarzembski et al. (2003) were used to calculate an extinction spectrum, in the same way as for the previous aerosol samples. Figure 8.7 shows this calculated extinction, as well as one of the new measured extinction spectra. The signal to noise ratio for this spectrum is sufficient to allow the characteristic peaks of the ammonium nitrate aerosol to be seen. While the peaks at $\sim 1400\,\mathrm{cm}^{-1}$, $\sim 2350\,\mathrm{cm}^{-1}$ and $\sim 3200\,\mathrm{cm}^{-1}$ are of a similar amplitude and width in both datasets, those at $\sim 1750\,\mathrm{cm}^{-1}$ and $\sim 2350\,\mathrm{cm}^{-1}$ are at slightly different wavenumber positions, with the measured data showing these peaks to be more separate and distinct from the other neighbouring peaks. The small structural details in the calculated dataset between approximately $1900\,\mathrm{cm}^{-1}$

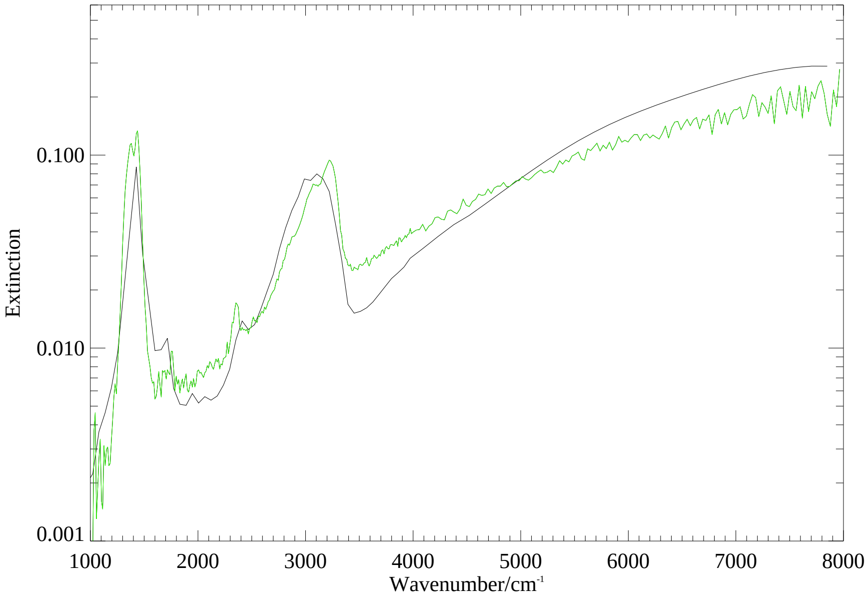

Figure 8.7: Ammonium nitrate aerosol extinction from current data (black) and measurements from RAL (green).

and 2100 cm^{-1} are not discernible in the measured extinction due to the noise level.

The signal to noise ratio for this spectrum was sufficient to attempt a refractive index retrieval. The a priori set of band parameters for this retrieval were obtained from the current set of refractive indices. Preliminary results are shown in figure 8.8, and are in good agreement with the current data, although the width and height of the peak at ~3200 cm^{-1} differ between the two datasets. The final set of band parameters from this retrieval is given in table 8.1.

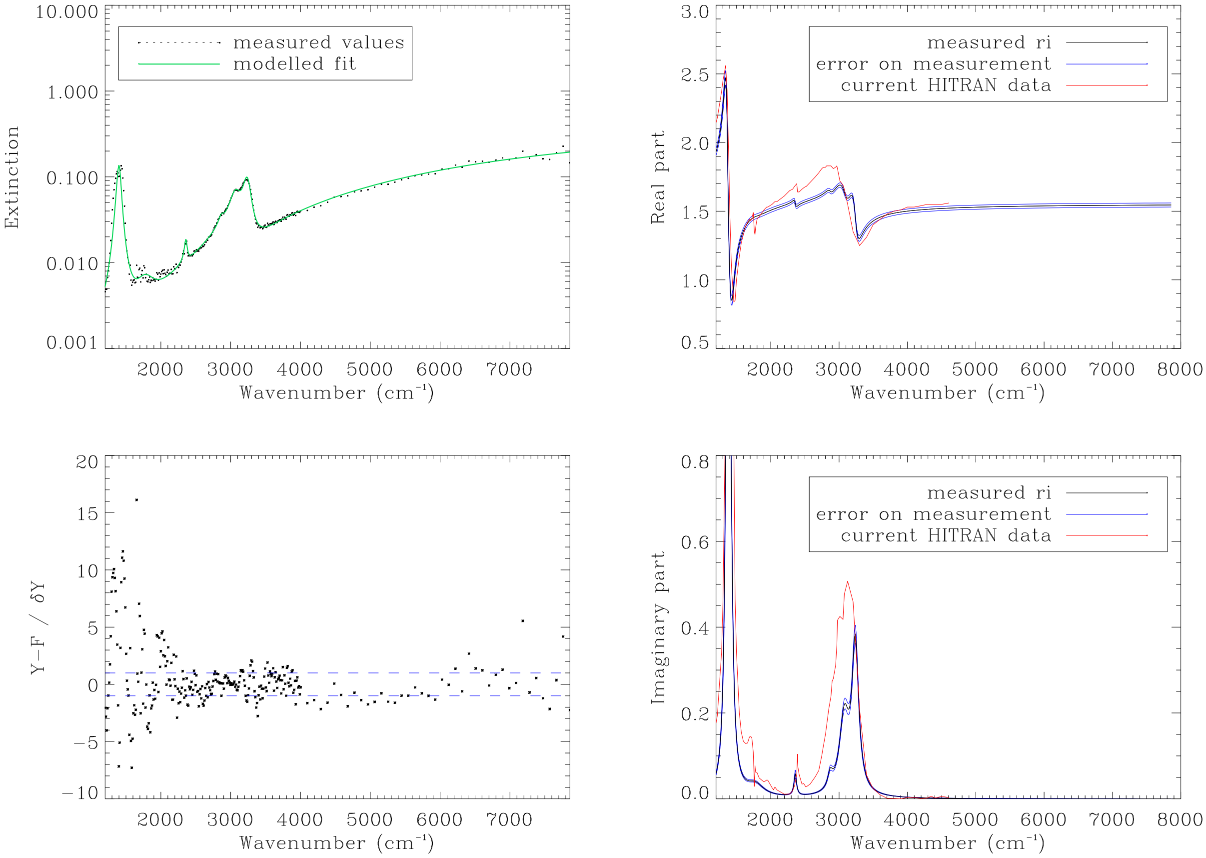

Figure 8.8: Preliminary results from refractive index retrieval for dry ammonium nitrate aerosol. $M_{500} = 1.55$, particle radius= 0.250 μm

These results are approximate as the particle size distribution parameters have

Position (cm^{-1})	Width (cm^{-1})	Strength (cm^{-2})
1362.7	63.1	518412
1780.5	313.2	43872
2358.6	45.2	16769
2870.3	88.4	29524
3074.4	173.8	314618
3231.2	115.6	374895

Table 8.1: Band parameters for dry ammonium nitrate aerosol. Bands due to water are present at ~1650 cm^{-1} and ~3430 cm^{-1}.

been retrieved by the algorithm. Further analysis of the particle size measurements taken during this experiment is necessary to improve the retrieved results. Problems with the sizing instruments during these measurements mean that much of the size data taken during this experiment has been corrupted. More detailed investigation into these results will determine whether or not useful data can be retrieved.

8.4.2 Dry Low Temperature Measurements

Measurements of dry ammonium nitrate aerosol were taken at 0 °C, − 10 °C and − 30 °C. Figures 8.9, 8.10 and 8.11 show the extinction spectra for measurements at each of these temperatures respectively, as well as the extinction calculated from current refractive index data, which was taken at room temperature. Aerosol measurements were made at − 20 °C; however, insufficient aerosol was present in the aerosol cell during these measurements to provide any discernible extinction.

The extinction measured at 0 °C is shown in figure 8.9. The peaks at ~ 1400 cm^{-1}, ~ 1750 cm^{-1}, ~ 2350 cm^{-1} and ~ 3200 cm^{-1} are present in both datasets, although the amplitude of the peaks is slightly greater in the measured extinction spectrum than in the extinction calculated from current refractive indices. The base of the

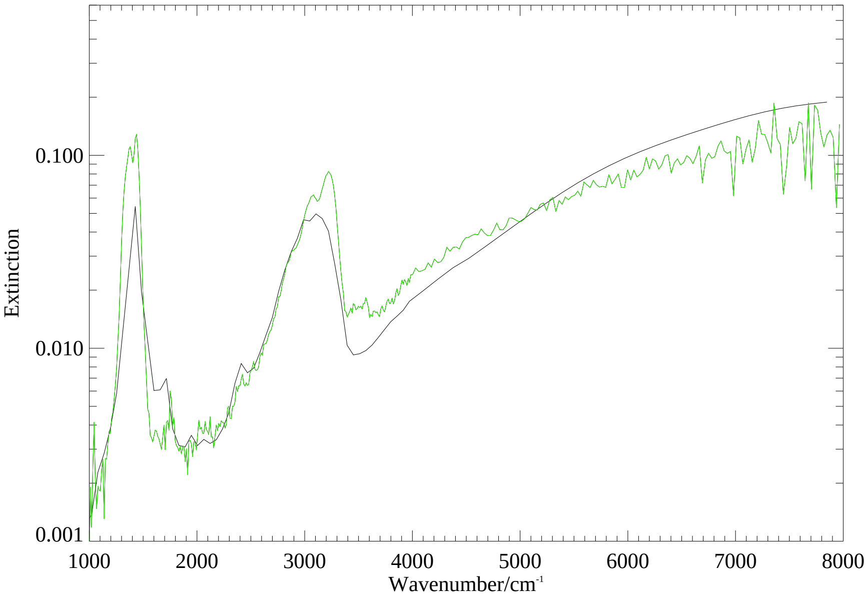

Figure 8.9: Ammonium nitrate aerosol extinction from current data taken at room temperature (black) and measurements from RAL taken at 0 °C (green). Particle size r ∼ 0.47 μm, particle number density N ∼ 2.0×10^5 cm^{-3}.

peak at the O-H stretch region (∼ 3200 cm^{-1}) is slightly wider here than for the data at room temperature, and overlaps the peak at ∼ 2350 cm^{-1} so that it is less distinct. A similar feature is also present to the right of the O-H stretch region at approximately 3600 cm^{-1}. This feature is not present in the calculated or measured extinctions from room temperature data. There is now also the suggestion of a peak at approximately 2000 cm^{-1} in the measured extinction, although the amplitude is only slightly greater than the noise for this dataset.

At − 10 °C the four main peaks are again visible in both datasets (see figure 8.10), although the amplitudes of the peaks at ∼ 1400 cm^{-1}, ∼ 1750 cm^{-1} and ∼ 3200 cm^{-1} are once more greater in the measured extinction than in that calculated from current refractive indices. While the peak at ∼ 1750 cm^{-1} remains separate and distinct from

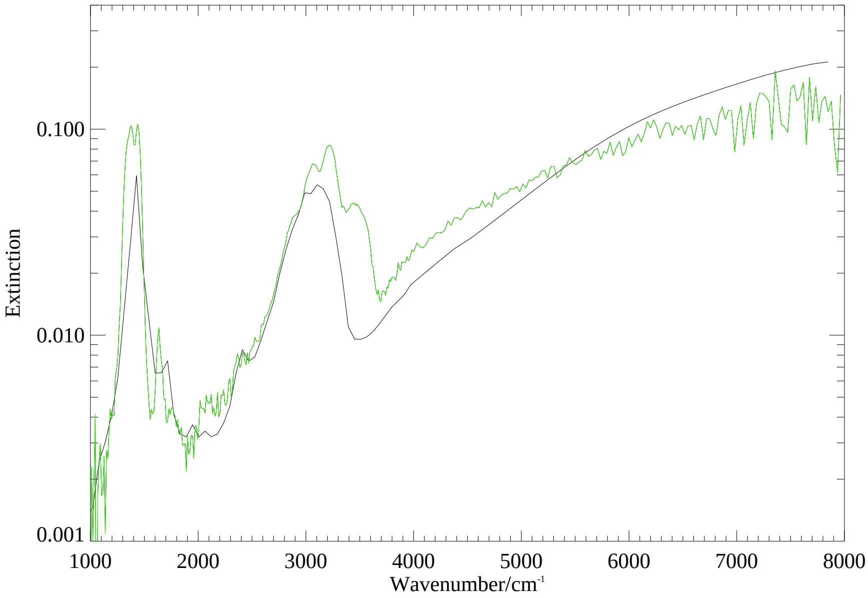

Figure 8.10: Ammonium nitrate aerosol extinction from current data taken at room temperature (black) and measurements from RAL taken at $-10\,^{\circ}$C (green). Particle size $r \sim 0.45\,\mu$m, particle number density $N \sim 2.5 \times 10^5\,\mathrm{cm}^{-3}$.

its nearest large peak at $\sim 1400\,\mathrm{cm}^{-1}$, the feature at $\sim 2350\,\mathrm{cm}^{-1}$ has now become merged with its nearest neighbour, the O-H stretch feature at $\sim 3200\,\mathrm{cm}^{-1}$. This has become much wider as the feature at approximately $3600\,\mathrm{cm}^{-1}$ that appeared at $0\,^{\circ}$C has more than doubled in amplitude. This suggests that this feature is related to a decrease in temperature. Finally, an additional step feature has appeared in the measured extinction data at approximately $1950\,\mathrm{cm}^{-1}$ that is not present in the calculated extinction.

At $-30\,^{\circ}$C the changes outlined for the spectra at $0\,^{\circ}$C and $-10\,^{\circ}$C have become more pronounced. While the four main peaks are still present, the amplitude difference between the measured and calculated data is no longer as great as it was at room temperature. The peak at $\sim 2350\,\mathrm{cm}^{-1}$ is no longer recognisable as a separate

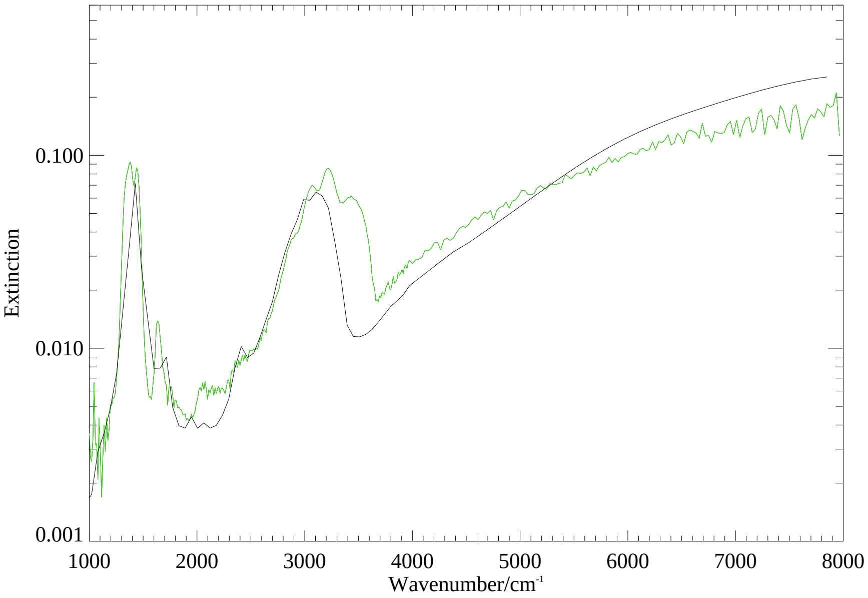

Figure 8.11: Ammonium nitrate aerosol extinction from current data taken at room temperature (black) and measurements from RAL taken at $-30\,°\mathrm{C}$ (green). Particle size $\mathrm{r} \sim 0.45\,\mu\mathrm{m}$, particle number density $\mathrm{N} \sim 3.0 \times 10^5\,\mathrm{cm}^{-3}$.

peak and has become a shoulder to the O-H stretch feature at $\sim 3200\,\mathrm{cm}^{-1}$. The peak over-lapping this feature at $\sim 3600\,\mathrm{cm}^{-1}$ has once more increased in amplitude, and the additional step feature that appeared at $\sim 1950\,\mathrm{cm}^{-1}$ has also increased in amplitude.

Figure 8.12 shows a close-up of the extinction spectra of all three low temperature measurements in order to allow a clearer comparison of the variation of these features with decreasing temperature. The increase in size of the new peak at $\sim 3600\,\mathrm{cm}^{-1}$ is clearly visible, and the feature at $\sim 2350\,\mathrm{cm}^{-1}$, although smaller, is also clearly increasing in size as the temperature decreases.

These changes confirm that a change in temperature does indeed alter the extinction, and therefore may alter the refractive indices, of dry ammonium nitrate

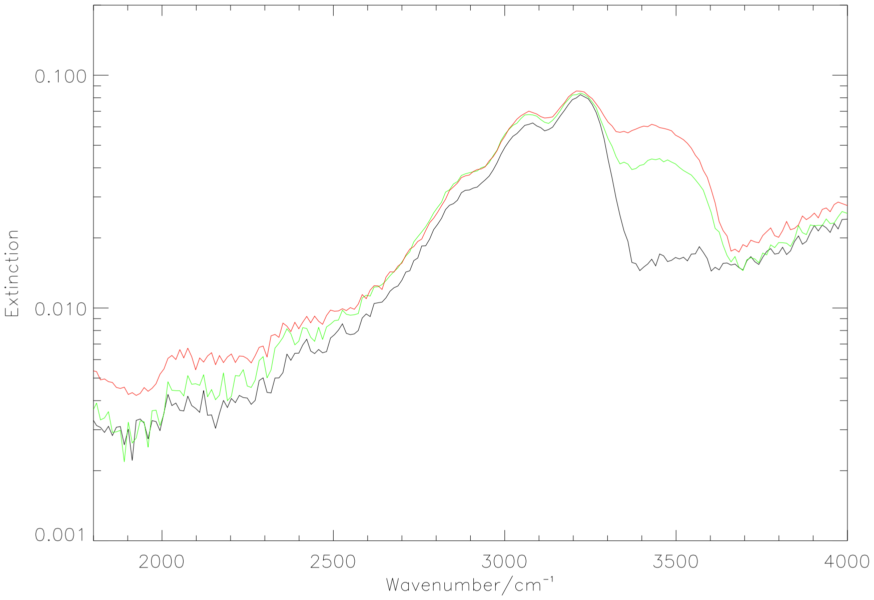

Figure 8.12: Ammonium nitrate aerosol extinction from measurements from RAL taken at 0 °C (black), − 10 °C (green) and at − 30 °C (red).

aerosol over the range 25 to −30 °C.

8.4.3 Wet Low Temperature Measurements

A single measurement was obtained for ammonium nitrate aerosol at 12.7 % RH, at − 10 °C (see figure 8.13). While there was no viable equivalent measurement at room temperature for this RH value, a comparison with figure 8.10 (the extinction of dry ammonium nitrate aerosol at − 10 °C) shows clear differences. The relative size of the peaks at ∼ 1400 cm^{-1} and ∼ 1750 cm^{-1} is different in the two measured spectra - the difference in the amplitudes of these peaks is greater for the dry measurement than for the wet measurement. The feature that appeared at ∼ 3600 cm^{-1} due to the decreased temperature appears to also be present in the wet sample, although

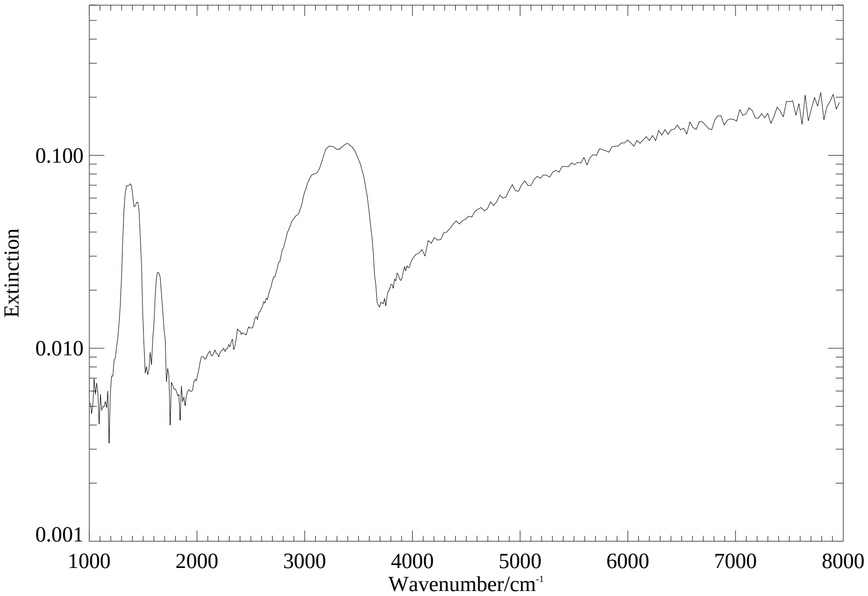

Figure 8.13: Ammonium nitrate aerosol extinction at 12.7 % RH taken at − 10 °C.

it is larger here than for the dry aerosol at this temperature. Further measurements of wet ammonium nitrate aerosol, both at room temperature and at − 10 °C, would allow definitive conclusions to be made about these changes.

At − 20 °C, measurements were made 30.2 % and 48.8 % RH (see figure 8.14). However, no aerosol could be seen in the cell for any of the measurements of dry ammonium nitrate aerosol taken at this temperature, which means there is no possibility of comparison. Intercomparison between the two RH values is also difficult due to the high signal to noise ratio of the measurement at 30.2 % RH. The extinction spectrum at 48.8 % RH is clearer and the low temperature feature at $\sim 3600\,\mathrm{cm}^{-1}$ appears to be present in that the width of the peak at $\sim 3200\,\mathrm{cm}^{-1}$ is greater than in the room temperature spectra. A single viable measurement was made with wet aerosol at 9.2 % RH at − 30 °C. However, the level of noise in this spectrum

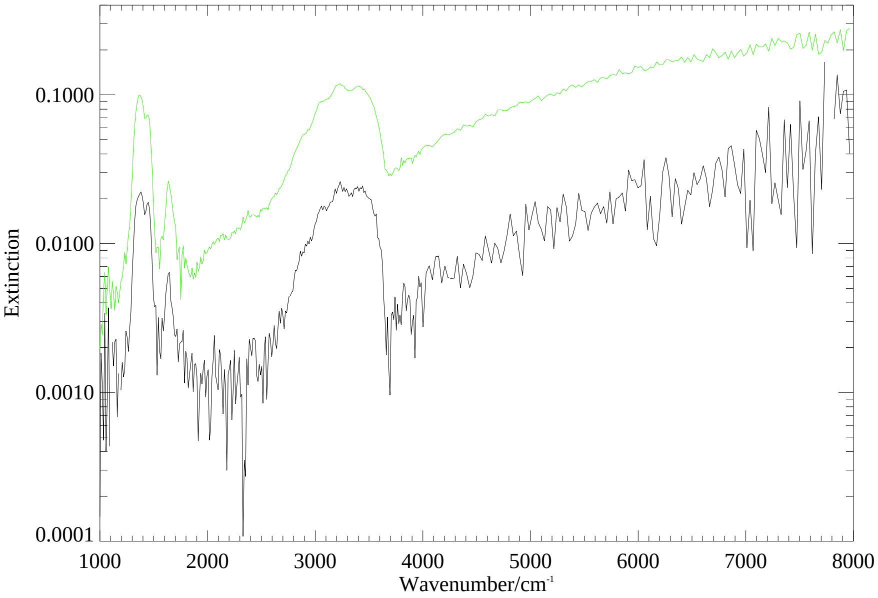

Figure 8.14: Ammonium nitrate aerosol extinction at 30.2 % RH (black) and at 48.8 % RH (green) taken at − 20 °C.

meant that only the low temperature feature at ∼3600 cm^{-1} is clearly visible (see figure 8.15).

8.5 Summary

- The optical properties of ammonium sulphate and ammonium nitrate aerosols have been derived from measurements on bulk samples, at room temperature.
- New measurements were made of dry ammonium sulphate and ammonium nitrate at room and low temperatures. A small number of measurements of wet ammonium nitrate aerosol were also made at low temperatures.
- The room temperature measurements for dry ammonium sulphate aerosol ex-

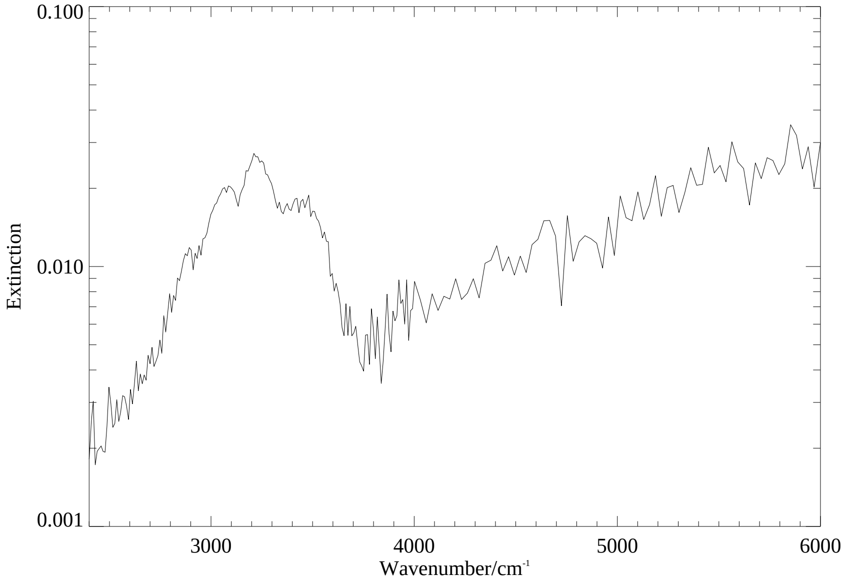

Figure 8.15: Ammonium nitrate aerosol extinction at 9.2 % RH taken at − 30 °C.

hibit the same peaks as the extinction calculated from current data, but there are differences in the size and shape of these peaks. At low temperatures there appears to be no discernible variation of the extinction with temperature. Although the spectrum measured at − 20 °C shows the presence of additional peaks, the relationship between these peaks and the temperature cannot yet be confirmed.

- Room temperature measurements for ammonium nitrate aerosol show the same main features as the current data. Retrieved refractive indices are also similar to the current data. However, there are differences in the height and width of a number of the peaks. This retrieval could be improved by the inclusion of a priori data from the sizing instruments.

- Low temperature measurements of ammonium nitrate aerosol show the appearance of a peak at $\sim 3600\,\mathrm{cm}^{-1}$ that grows with decreasing temperature. Low temperature measurements of wet ammonium nitrate aerosol also show this peak.

- Generally, the signal to noise ratios for this data are lower than for the sea salt data, due to practical difficulties in producing sufficient number densities of aerosol particles. Nevertheless, the data clearly show that the extinction of low temperature ammonium nitrate aerosol is different to that at room temperatures, and therefore provide justification for future studies on the optical properties of this aerosol at low temperatures.

Chapter 9

Conclusions

A summary of the work done to date is given in this chapter, as well as an overview of possible future work.

9.1 Summary

This thesis details the design and construction of an experiment to produce sea salt aerosols at a variety of relative humidity values and measure the aerosol transmission by Fourier transform spectrometry, as well as the particle size and number densities with appropriate instrumentation. This was done with a view to retrieving the refractive indices of sea salt aerosol using the CDHO model pioneered by Thomas et al. (2004).

9.1.1 Sea Salt Aerosol

It was suggested that the current refractive index data for SSA were inadequate for the following reasons:

- Previous measurements by Volz (1972) were made on bulk samples of powdered sea salt on KBr pellets, rather than actual SSA.
- Two independent methods were used to determine the real and imaginary parts of the refractive indices. However, these did not correspond according to the Kramers-Kronig equations which describe the relationship between these two parts of complex refractive indices.
- It was reported both that the surfaces of the samples remained essentially dry and that there was significant deterioration of the samples due to exposure to humidity, therefore the integrity of the samples was not verifiable.
- The refractive indices of wet SSA were calculated by Shettle and Fenn (1979) using volume mixing rules. It was suggested that this method may not hold for solutions of salts that readily dissolve in water, due to the dissociation of the ions of the salt.
- The refractive indices of water used by Shettle and Fenn (1979) have been superceded by more recent measurements made by Segelstein (1981), which are at a higher resolution to previous measurements. Thus any calculations made using the older refractive indices of water require updating, regardless of the validity of the volume mixing rules.

In order to determine the validity of the volume mixing rules, and to provide direct measurements of both dry and wet SSA particles, an experiment was designed and set up to produce and measure soluble aerosols over a range of RH values. Necessary hardware was sourced, modified and, where required, designed and manufactured. These are outlined below:

- Instruments to produce the aerosol were investigated. An OMRON U-17 nebuliser was chosen after in-house testing showed that it could produce the required particle number densities over a size range representative of tropospheric aerosol. Stainless steel fittings were designed and manufactured to provide gas-tight connections to a nitrogen source and to carry the aerosol to the remaining instrumentation.

- The decision was made to dry the aerosol particles produced from solution and then re-hydrate them to controlled RH values in order to avoid hysteresis effects. Two diffusion dryers were therefore designed and manufactured to remove water from the aerosol by means of a non-reactive beaded silica gel desicant. Swagelok fittings and tubing were used to carry the aerosol through the dryers.

- The RH of the aerosol was varied by the addition of water vapour from a heated bath. The ratio of the gas flows carrying aerosol and water vapour were varied to determine the different RH values produced. A 2.75 litre glass conditioning vessel was designed and manufactured to provide a sufficient volume to allow the aerosol particles to reach equilibrium. A Honeywell sensor was used to monitor the temperature and RH of the aerosol leaving the conditioner.

- The existing small aerosol cell at the RAL MSF was used to hold the aerosol during transmission measurements which were made using a Bruker 66V/S Fourier transform spectrometer and DLaTGS detector. The resolution of these instruments was greater than that of previous measurements of SSA.

- Particle size and number density measurements were made using a GRIMM

SMPS+C device in conjunction with an API Aerosizer instrument in order to cover the complete size range of aerosols that may be produced.

Algorithms were then required to complete the pre-processing of FTIR intensity data, ready for retrieval of refractive index. This included Kalman filtering of background data to provide more accurate and representative spectral backgrounds, as well as procedures for the retrieval and removal of water and carbon dioxide gas lines from the measurement spectra. A comprehensive software suite was produced in IDL to perform this pre-processing on any intensity spectra measured using a spectrometer.

Additional measurements of dry sodium chloride aerosol were made and the refractive index spectrum was retrieved using a retrieval algorithm which combined the CDHO model with a Mie scattering algorithm. The resultant refractive indices showed good agreement with the current data. This provided independent validation of the refractive index retrieval method, in addition to the validation exercises performed by Bass (2003).

The refractive indices of sea salt aerosol were obtained for nine different relative humidity values, and proved to be different to previous data, as well as at a higher resolution. The refractive indices for dry SSA specifically were different to the Volz (1972) data which showed evidence of water, suggesting that the original questions regarding the potential contamination of the measured sample were justified.

In order to investigate the validity of the volume mixing rules, further calculations were performed using new refractive index data for dry sea salt aerosol and more recent data for the refractive indices of water from Segelstein (1981). The resulting refractive indices of wet sea salt aerosol were different to direct measurements of sea salt aerosol at the same RH. This suggests that the volume mixing rules are inadequate for describing the refractive indices of solutions. This result has significant and far-reaching implications due to the large number of studies currently being undertaken using volume-mixed refractive indices for soluble solutions including, but not limited to, sea salt aerosol.

The refractive indices presented here were retrieved from direct measurements of aerosols and are therefore more representative of the natural aerosol than previous data. This means that the infrared scattering and absorption of sea salt aerosols can now be more accurately predicted, and more realistic parameters may be used in atmospheric models.

Preliminary results from satellite retrievals using this new data show a significant decrease in the magnitude of retrieved aerosol optical depth over the Atlantic ocean for a specific case study on the 8th March, 2008. The values retrieved using the new refractive indices are approximately 40 % lower than those retrieved using the current data available on HITRAN. This suggests that the new data will cause considerable changes to satellite retrievals and global climate models.

9.1.2 Additional Work

Due to the success of the work with sea salt aerosol, the same experimental design was used to produce and measure ammonium sulphate and ammonium nitrate aerosols. This time, the aerosols were carried through a pre-cooler and the aerosol cell was also cooled in order to make low temperature measurements. Transmission measurements were made at a lower resolution than for sea salt aerosol and extinction spectra were calculated from current refractive index data for comparison with the new measurements. The results are summarised below:

Ammonium Sulphate Aerosol

- The extinction spectra of dry ammonium sulphate aerosol at room temperature show good agreement with current data, with small differences.
- The extinction spectra of dry ammonium sulphate aerosol have also been obtained at − 10 °C, − 20 °C and − 30 °C. On analysis there was no clear sign to show any significant variation of the extinction spectra with decreasing temperatures in the range studied. However, the presence of new peaks in the data at − 20 °C justifies further investigation.
- There was a low signal to noise ratio for the data at − 10 °C, and missing information in the spectra at − 30 °C. Therefore further measurements at these temperatures would be advisable before definitive conclusions can be made.

Ammonium Nitrate Aerosol

- The extinction spectra of dry ammonium nitrate aerosol at room temperature are also in good agreement with current data. There are some slight differences between the new measurements and the current data, but a high noise level means that it is possible that some detail has been lost in the new measurements. Nevertheless, a refractive index retrieval was performed to provide a first estimate of the refractive index spectrum from the new measurements. Once again there were small differences between the new retrieved and the current refractive indices, but this may change once particle size and number density measurements are also added to the retrieval.

- Measurements of the extinction of dry ammonium nitrate aerosol at 0 °C, − 10 °C and − 30 °C were presented. Analysis of the spectra clearly shows a marked variation of the extinction as the temperature decreases. This indicates that the extinction spectra of ammonium nitrate aerosol are dependent on temperature, and suggests the possibility that the refractive indices may vary with temperature.

- Measurements of the extinction spectra of wet ammonium nitrate aerosol were made at − 10 °C, − 20 °C and − 30 °C. These show that the features that appear in the dry ammonium nitrate spectra as the temperature decreases are also present at low temperatures for the wet aerosol.

9.2 Suggestions for Future Work

- There remain difficulties in removing gas lines due to water from the measurement spectra, especially at high RH values. Possible further work may involve improving the retrieval of gas lines from transmission spectra to improve accuracy in the spectral regions where water is expected.

- Currently, the CDHO model assumes that all bands are symmetric. In order to make the model more realistic, it should be extended to allow for the presence of asymmetry in the absorption bands.

- Since it has been shown that the volume mixing rules do not adequately describe the refractive indices of wet sea salt aerosol, further measurements at other RH values may be advantageous, as would the detailed analysis of the variation in refractive index with RH with a view to describing a possible parametrisation.

- The SSA measurements made during this study were limited to room temperature. Low temperature measurements of wet SSA could be made in order to investigate the formation of ice crystals on such particles.

- Additionally, the new refractive index data obtained for sea salt aerosols may be used to improve current radiative transfer models of the atmosphere. Future work may involve the implementation of the new data in such models, and comparisons with previous models to quantify possible improvement. This would entail detailed knowledge of the variation of the RH of SSA both geographically and with height in the atmosphere. Current models of the atmosphere tend to assume an RH of 98 % immediately above the oceans, and between 50 to 75 % at tropospheric heights, depending on the model used. From preliminary results, the difference in the new and old refractive indices is expected to have a noticeable effect on satellite retrievals and global climate models. The use of this more accurate data can only improve these models by making them more representative of actual aerosol.

- Refractive index retrievals have yet to be performed on most of the ammonium sulphate and ammonium nitrate data collected. This process would involve the building of an a priori band set from current data, followed by the running of retrievals using a priori data from the Aerosizer and GRIMM SMPS+C instruments. As there is much more data available on the ammonium compounds than there was for sea salt aerosol, this should be a simpler process for these compounds than for the SSA. For the dry ammonium nitrate aerosol, for which an a priori band set has been obtained, it is only the particle size and number density data that remains to be analysed, before being incorporated into the retrieval.

- The noise level on the current measurements may prove to be too great to allow accurate retrieval of refractive indices. However, the low temperature variations in the extinction spectra of ammonium nitrate clearly show that further measurements of this aerosol at higher resolutions are justifiable. Further measurements of low temperature ammonium sulphate would also definitively confirm any variation of the extinction with temperature.
- In addition, while measurements were made on wet ammonium sulphate and ammonium nitrate aerosols, these were of poor quality, with very small amount of aerosol absorption and large amounts of noise. It would therefore be advisable to repeat these experiments in order to obtain more complete and less noisy spectra from which detailed and accurate refractive indices may be retrieved, as it has been shown that refractive indices obtained using the volume mixing rules are inaccurate.
- Finally, the experimental set-up may be used to create and measure other aerosols at room and low temperatures.

Appendix A

Retrieval Theory

A.0.1 Forward Model

Let us describe the measurements as a vector, **y**, and the amount of unknown gas in the transmission spectra as the scalar value of the state, x. After Rodgers (2000), a forward model may be used to describe the physics of the measurement process, and therefore the approximate relationship between the measurement and the state:

$$\mathbf{y} = \mathbf{F}(\mathrm{x}) + \epsilon \tag{A.1}$$

where $\mathbf{F}(\mathrm{x})$ is the forward model and ϵ is the error on the measurement.

The forward model incorporates all aspects of the state of which we have knowledge, for example the length of the aerosol cell and the temperature and pressure in the cell, etc. It also takes into account factors such as the influence of line-mixing on CO_2 and the spectral line shape etc. The model therefore consists of a complicated set of equations that cannot be solved explicitly for x. Computational methods are therefore used to retrieve the state. In this case the model used to derive transmission spectra at different values of CO_2 and H_2O concentration is the AOPP Reference Forward Model (AOPP, 2006). This is a radiative transfer model originally designed to provide reference spectral calculations for the MIPAS instrument.

An iterative method is used to fit spectra generated by the forward model to the measurement spectra using an estimate of the state. At each iteration the estimate of x is updated and the process is repeated until some predefined convergence criterion is met.

A.0.2 Non-Linear Retrieval

The problem is non-linear and this requires us to find the solution iteratively using linear equations. If we ignore the measurement error, these equations are of the form:

$$\mathrm{x}_{\mathrm{n}+1} = \mathrm{x}_{\mathrm{n}} + \mathbf{G}_{\mathrm{n}}[\mathbf{y} - \mathbf{F}(\mathrm{x}_{\mathrm{n}})] \tag{A.2}$$

where $\mathbf{G}_n$ is known as the Gain Matrix (Rodgers, 2000). The Gain Matrix is the inverse of the Jacobian $\mathbf{k}$ where $\mathbf{k} = \frac{\partial \mathbf{F}}{\partial \mathrm{x}}$. Here, n denotes the number of the estimate of each quantity, so x_0 is the initial estimate of x.

A.0.3 Least Squares Fit Retrieval

In the linear state, for a set of measurements, $\mathbf{y}$, and a scalar state, x, we may write:

$$\mathbf{y} = \mathbf{k}\mathrm{x} \quad \mathrm{x} = \mathbf{g}^{\mathrm{T}}\mathbf{y} \tag{A.3}$$

where $\mathbf{k}$ is the vector Jacobian, and $\mathbf{g}^T$ the inverse of $\mathbf{k}$, as required to find x. However, $\mathbf{k}$ is a vector so we cannot simply find its inverse. Instead, to find $\mathbf{g}^T$, and therefore x, by the least squares fit method we minimise the sum of the square difference $\sum_i (y_i - k_i x)^2$. This is the cost function, χ^2:

$$\chi^2 = (\mathbf{y} - \mathbf{k}\mathrm{x})^{\mathrm{T}}(\mathbf{y} - \mathbf{k}\mathrm{x}) \tag{A.4}$$

In the non-linear case we linearise about an estimate of the solution, x_n, and equation A.2 becomes:

$$\mathrm{x_{n+1}} = \mathrm{x_n} + (\mathbf{k}_\mathrm{n}^\mathrm{T}\,\mathbf{k}_\mathrm{n})^{-1}\mathbf{k}_\mathrm{n}^\mathrm{T}[\,\mathbf{y} - \mathbf{F}(\mathrm{x_n})] \tag{A.5}$$

Next let us consider the errors involved. These may be represented using covariance matrices. The elements of the error covariance matrix are given by:

$$S_{ij} = E\left(\epsilon_i \epsilon_j\right) \tag{A.6}$$

where E is the expected value operator and ϵ_i and ϵ_j are the elements of the measurement error. Therefore if we now include the measurement error covariance, $\mathbf{S}_\epsilon$, then the total covariance is:

$$\mathbf{S} = (\mathbf{k}^\mathrm{T}\mathbf{S}_\epsilon\,\mathbf{k})^{-1} \tag{A.7}$$

and the cost function becomes:

$$\chi^2 = (\mathbf{y} - \mathbf{k}\mathrm{x})^{\mathrm{T}}\mathbf{S}_\epsilon^{-1}(\mathbf{y} - \mathbf{k}\mathrm{x}) \tag{A.8}$$

A.0.4 Levenberg- Marquardt Method

The refractive index retrieval algorithm is based on the Levenberg-Marquardt method. To understand this, let us consider the determination of the value of a state vector $\mathbf{x}$ for which the forward model $\mathbf{F(x)}$ produces a best fit to a measurement $\mathbf{y}$ subject to constraints from prior knowledge of the state. If we now constrain the solution to be close to some a priori solution $\mathbf{x}_a$, then the cost function becomes:

$$\chi^2 = [\mathbf{y} - \mathbf{F}(\mathbf{x})]^{\mathrm{T}}\mathbf{S}_{\epsilon}^{-1}[\mathbf{y} - \mathbf{F}(\mathbf{x})] + (\mathbf{x} - \mathbf{x}_{\mathrm{a}})^{\mathrm{T}}\mathbf{S}_{\mathrm{a}}^{-1}(\mathbf{x} - \mathbf{x}_{\mathrm{a}}) \tag{A.9}$$

where $\mathbf{x}_a$ is the best estimate of the state before measurement and $\mathbf{S}_a$ is the corresponding covariance matrix representing the uncertainty in $\mathbf{x}_a$. This is the function minimised by the retrieval algorithm (Thomas et al., 2004).

Appendix B

Examples of Measured Spectra

Samples of the transmission spectra of sodium chloride and sea salt aerosols calculated from measurements are given below. The transmission spectra are shown over the full range at which measurements are taken before regridding of the data. Kalman filtered backgrounds have been removed to provide transmission but no further processing has been completed on the spectra shown.

Gas retrievals were performed on the ammonium sulphate and ammonium nitrate spectra which allowed the RH values of the aerosol samples to be retrieved and the extinction spectra to be calculated. These extinction spectra are therefore given, wherever possible, rather than the raw transmission data.

B.0.5 Sodium Chloride Aerosol

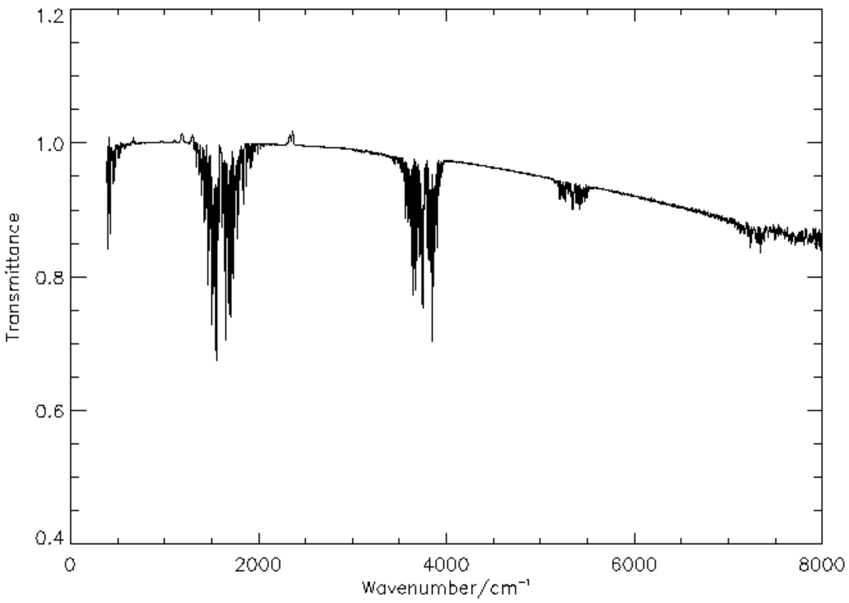

Figure B.1: Wet NaCl aerosol transmission spectrum taken on 02/11/05.

Figure B.1 shows a transmission spectrum for wet sodium chloride aerosol. There is a relatively low absorption signal due to the aerosol compared to most of the sea salt spectra that were eventually analysed for refractive index retrieval. However, there is a great deal of contamination due to gas lines from water that are clearly evident at $\sim$1600 cm^{-1}, $\sim$3600 cm^{-1}, $\sim$5350 cm^{-1} and $\sim$7250 cm^{-1}. The peak at approximately 2400 cm^{-1} is due to carbon dioxide. The shape of this peak resembles an emission line rather than an absorption line, which suggests that for this particular sample there was more carbon dioxide in the aerosol cell during the background measurement than during the sample measurement. The gas line retrieval was modified to allow for this possibility and remove the contaminant lines regardless.

Figure B.2 shows a transmission spectrum for another wet sodium chloride

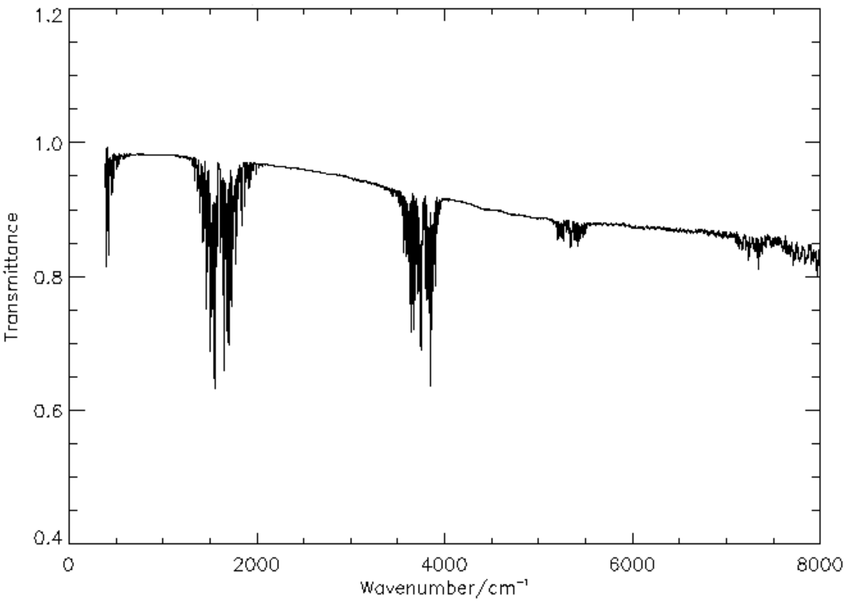

Figure B.2: Wet NaCl aerosol transmission spectrum taken on 04/11/05.

aerosol sample. This time there is slightly more absorption and scattering due to aerosol and no carbon dioxide contaminant gas lines are visible.

B.0.6 Sea Salt Aerosol

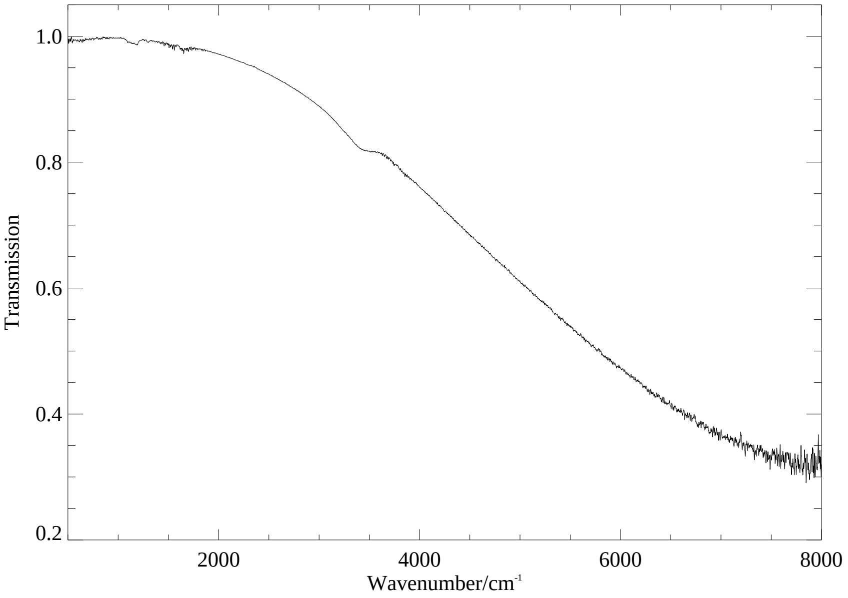

Figure B.3: Dry sea salt aerosol transmission spectrum taken on 09/11/05.

Figure B.3 shows a typical transmission spectrum for dry sea salt aerosol. Absorption features are visible at ∼1300 cm^{-1} as well as the well-defined O-H stretch feature at ∼3400 cm^{-1}. There is a great deal of scattering due to aerosol and a very small level of gas line contamination, once more at those wavenumber regions representative of water and carbon dioxide. The small carbon dioxide peak at ∼2400 cm^{-1} again shows that there was more carbon dioxide in the background measurement than for the sample measurement.

Figure B.4 is another transmission spectrum for dry sea salt aerosol, taken on a different day to the spectrum in figure B.3. This time aerosol absorption features are not clearly visible and the carbon dioxide line at ∼2400 cm^{-1} shows that gas contamination was greater during the sample measurement than the background.

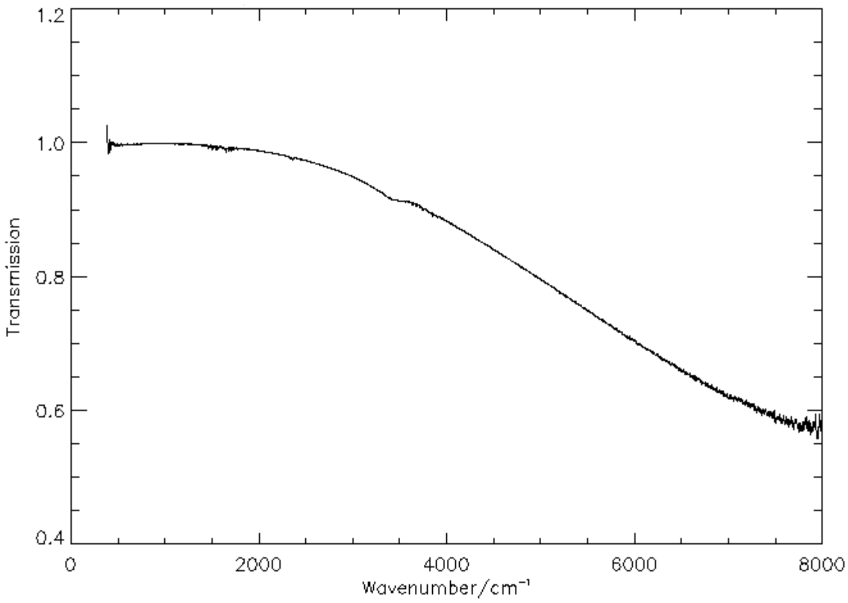

Figure B.4: Dry sea salt aerosol transmission spectrum taken on 25/11/05 (second salt compound).

There is also much more scattering due to the aerosol in this measurement than in the spectrum shown in figure B.3.

The transmission spectrum in figure B.5 is of wet sea salt aerosol. This figure shows the result of excessive water vapour in the aerosol cell. The spectrum is distorted by large amounts of absorption at those places in the spectrum representative of water. After this measurement was taken, the aerosol cell was removed from the spectrometer's sample compartment and dismantled for cleaning. Liquid aerosol solution was clearly visible on the windows of the cell, where it had condensed.

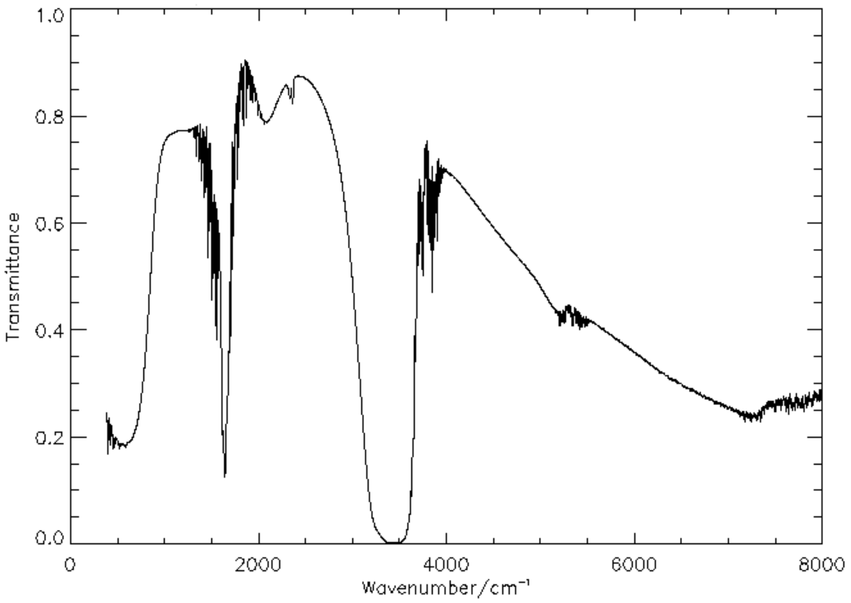

Figure B.5: Wet sea salt aerosol transmission spectrum taken on 23/11/05.

B.0.7 Ammonium Sulphate Aerosol

Figure B.6 shows an example of one of the best extinction spectra obtained for wet ammonium sulphate aerosol. While the level of extinction by the aerosol is relatively small, and the noise level relatively high, the characteristic features of the compound are clearly discernible. The low level of water can be seen in the distinctive lines at $\sim 3750\,\mathrm{cm}^{-1}$ which the gas retrieval algorithm failed to distinguish from the background noise.

Figure B.7 is at 18.5 % RH which means that more of the residual water lines can be seen at both $\sim 1750\,\mathrm{cm}^{-1}$ and $\sim 3750\,\mathrm{cm}^{-1}$. The O-H stretch feature at $\sim 3300\,\mathrm{cm}^{-1}$ has become wider at the base due to the increased RH of the aerosol; this response is also observed in the extinction spectra of wet sea salt aerosol.

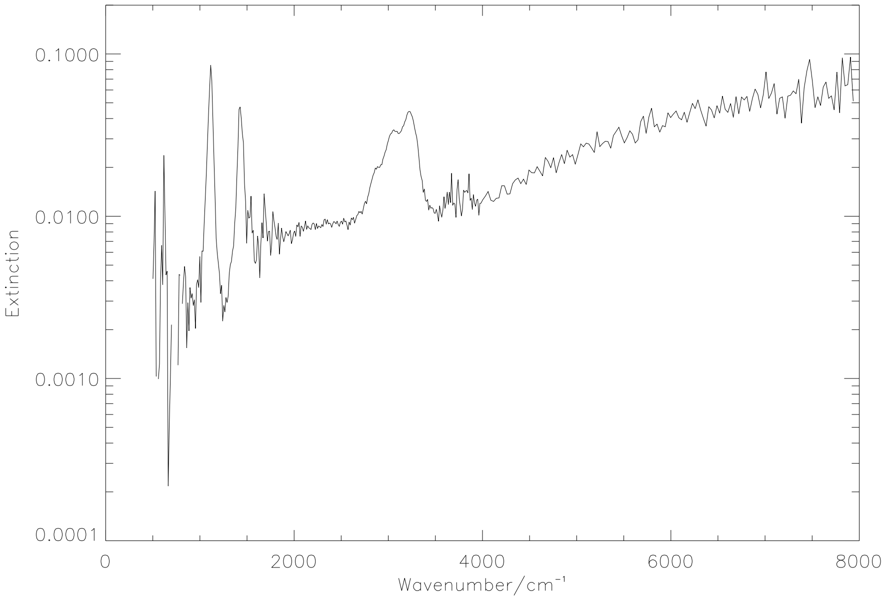

Figure B.6: Ammonium sulphate aerosol extinction spectrum at 8.6 % RH taken on 01/12/06.

B.0.8 Ammonium Nitrate Aerosol

Figure B.8 shows one of the better examples of the extinction spectra calculated for wet ammonium nitrate aerosol. The noise level is high and the signal is poor but some features remain visible. Residual lines from the gas retrievals can also be seen.

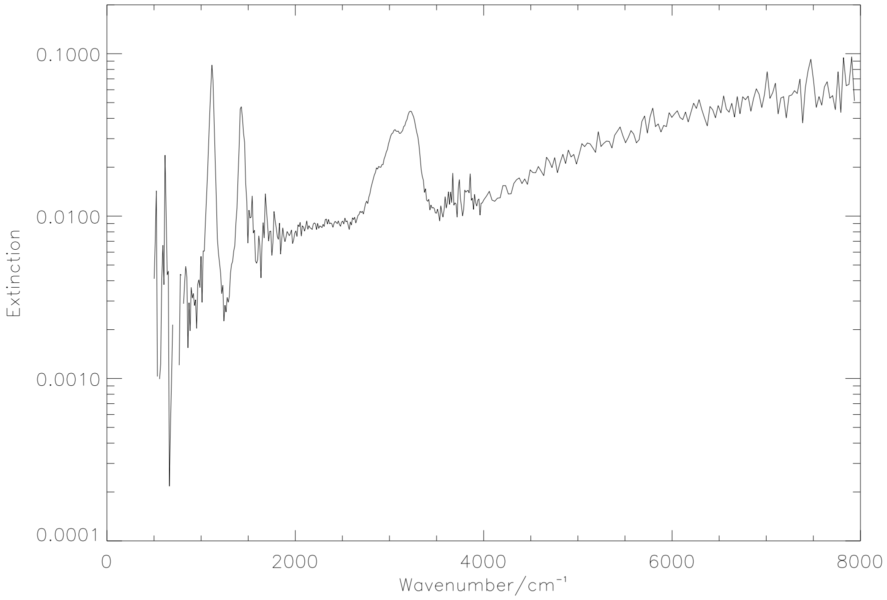

Figure B.7: Ammonium sulphate aerosol extinction spectrum at 18.5 % RH taken on 06/12/06.

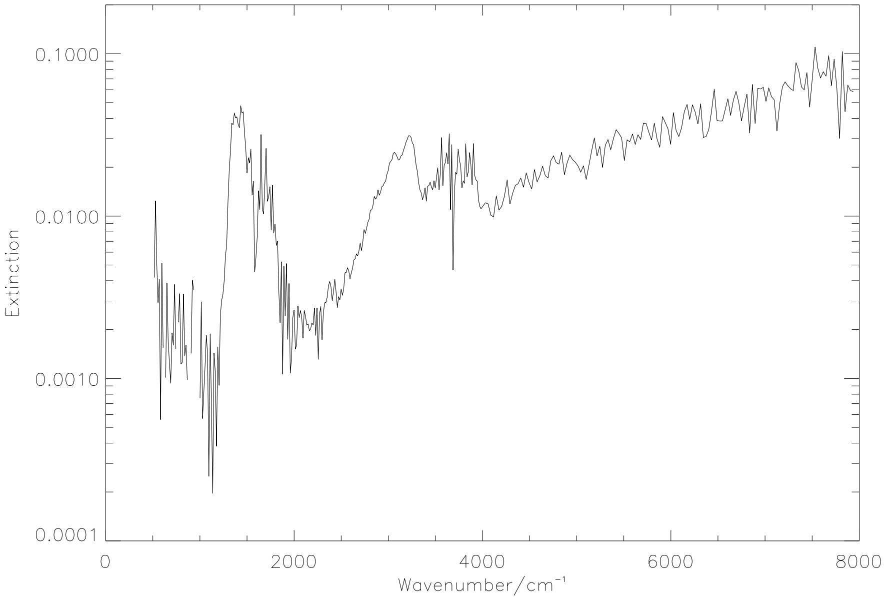

Figure B.8: Ammonium nitrate aerosol extinction spectrum at 12.6 % RH taken on 12/12/06.

Appendix C

Kalman Filters

A Kalman filter (Kalman, 1960) consists of a set of mathematical equations that describe a recursive method of estimating the state of a process. This is done in such a way as to minimise the variance of the estimation error. For a series of measurements made over time, the Kalman filter combines all measurement data and uncertainties with any prior knowledge of the system to provide estimates of the state at a particular point in time (Welch and Bishop, 2006).

The Kalman smoother uses the Kalman filter to estimate the state at any point in time by also taking into account measurements of future states, after that time. This is useful when the state of a system cannot be measured directly but must be inferred from the available data, for example, when estimating the exact background intensity spectrum at time [t] inferred from background spectra taken at other times [t-1] or [t+1] (Maybeck, 1979).

To describe the Kalman filter equations, let us look at a simple one-dimensional problem. Consider the following equations:

$$\mathbf{x}_{\mathrm{t}} = \mathbf{F}\,\mathbf{x}_{\mathrm{t-1}} + \boldsymbol{\alpha}_{\mathrm{t}} \tag{C.1}$$

$$\mathbf{y}_{\mathrm{t}} = \mathbf{M}\,\mathbf{x}_{\mathrm{t}} + \boldsymbol{\beta}_{\mathrm{t}} \tag{C.2}$$

Equation C.1 is a state equation that describes the evolution of the state, $\mathbf{x}$, with time, t. Equation C.2 describes the measurement as a function of $\mathbf{x}$ that is corrupted by noise. $\mathbf{F}$ and $\mathbf{M}$ are known matrices, while $\boldsymbol{\alpha}$ is the process noise. This is a random vector that is uncorrelated with other variables, or with past values of $\boldsymbol{\alpha}$. In equation C.2, $\boldsymbol{\beta}$ represents the noise in the measurement, which is also random and independent (Rodgers, 2000). This means that the process noise covariance is given by $S_\alpha = E(\boldsymbol{\alpha}_t\,\boldsymbol{\alpha}_t^T)$ and the measurement noise covariance is given by $S_\beta = E(\boldsymbol{\beta}_t\,\boldsymbol{\beta}_t^T)$, where $E(n)$ implies the expectation value of n. From equation C.1 we can say that the a priori state estimate, based on a knowledge of the state at t, is given by:

$$\mathbf{x}_{\mathrm{at}} = \mathbf{F}\,\mathbf{x}_{\mathrm{t-1}}$$

We can also describe the corresponding covariance at time t as:

$$\mathbf{S}_{\mathrm{at}} = \mathbf{F}\,\mathbf{S}_{\mathrm{t-1}}\,\mathbf{F}^{\mathrm{T}} + \mathbf{S}_\alpha$$

The Kalman filter then uses the available measurements $\mathbf{y}$ to estimate the state $\mathbf{x}$, given a knowledge of the behaviour of the system described by the state equation.

This is done using the following equations:

$$\mathbf{K}_{\mathrm{t}} = \mathbf{S}_{\mathrm{at}}\,\mathbf{M}^{\mathrm{T}}(\mathbf{M}\,\mathbf{S}_{\mathrm{at}}\,\mathbf{M}^{\mathrm{T}} + \mathbf{S}_{\beta})^{-1} \tag{C.3}$$

$$\mathbf{x}_{\mathrm{t}} = \mathbf{x}_{\mathrm{at}} + \mathbf{K}_{\mathrm{t}}(\mathbf{y}_{\mathrm{t}} - \mathbf{M}\,\mathbf{x}_{\mathrm{at}}) \tag{C.4}$$

$$\mathbf{S}_{\mathrm{t}} = \mathbf{S}_{\mathrm{at}} - \mathbf{K}_{\mathrm{t}}\,\mathbf{M}\,\mathbf{S}_{\mathrm{at}} \tag{C.5}$$

where $\mathbf{K}_{\mathrm{t}}$ is the Kalman Gain matrix, chosen to minimise the variance of the estimation error, $\mathbf{x}_{\mathrm{t}}$ is the state estimate and $\mathbf{S}_{\mathrm{t}}$ is the estimation error covariance. The second term in equation C.4 is the correction term which represents the correction applied to the propagated state estimate due to the measurement value (Simon, 2001).

The Kalman Smoother then extends these equations to run the filter both backwards and forwards in time. The forward filter provides an estimate of present and future states based on prior measurements. The backward filter provides an estimate of the present and prior states based on future measurements. The Smoother combines the two estimates with appropriate weightings to give a final, more accurate estimate of the state.

For a clearer understanding of how these filters are applied, please refer back to the examples given in section 4.2.

Appendix D

Band Parameters

The final retrieved sets of band parameters for the sea salt aerosol refractive index retrievals are given in this section.

RH (%)	0.4			22.9			29.5		
Bands	pos.	width	height	pos.	width	height	pos.	width	height
Band 1	0	5933	73625	n/r	n/r	n/r	n/r	n/r	n/r
Band 2	627	129	10259	n/r	n/r	n/r	n/r	n/r	n/r
Band 3	1157	86	7165	n/r	n/r	n/r	n/r	n/r	n/r
Band 4	0	0	0	n/r	n/r	n/r	n/r	n/r	n/r
Band 5	1647	82	4326	n/r	n/r	n/r	n/r	n/r	n/r
Band 6	0	0	0	2622	3447	1684728	2493	2846	1116197
Band 7	3427	284	63844	3756	946	248618	3752	998	318577

Table D.1: Band parameters for SSA measurements from 0.4 to 29.5 % RH. Where no bands were retrieved due to low resolution data, the entry lists ”n/r”. ”Pos.” refers to the wavenumber position of the bands.

RH (%)	38.5			48.8			74.2		
Bands	pos.	width	height	pos.	width	height	pos.	width	height
Band 1	n/r	n/r	n/r	0	10	524241	352	168	438015
Band 2	n/r	n/r	n/r	0	0	0	608	278	207944
Band 3	n/r	n/r	n/r	1122	150	3461	1147	140	10706
Band 4	n/r	n/r	n/r	0	0	0	1448	377	70858
Band 5	n/r	n/r	n/r	1592	494	78155	1643	86	109899
Band 6	2398	2576	813568	2478	2210	634962	3094	252	39014
Band 7	3717	1035	306825	3644	947	284898	3471	152	1137066

Table D.2: Band parameters for SSA measurements from 38.5 to 74.2 % RH. Where no bands were retrieved due to low resolution data, the entry lists ”n/r”. ”Pos.” refers to the wavenumber position of the bands.

RH (%)	76.7			86.4		
Bands	pos.	width	height	pos.	width	height
Band 1	397	175	397104	367	171	374696
Band 2	631	262	179481	613	285	234891
Band 3	1162	178	12122	1189	202	15526
Band 4	1434	352	57572	1434	349	60573
Band 5	1643	78	96828	1644	81	96702
Band 6	2095	269	41152	2086	324	51791
Band 7	3461	151	1125995	3479	133	1128639

Table D.3: Band parameters for SSA measurements at 76.7 % and 86.4 % RH. ”Pos.” refers to the wavenumber position of the bands.

Bibliography

Adams, P. J., Seinfeld, J. H., and Koch, D. M.: Global concentrations of tropospheric sulphate, nitrate and ammonium aerosol simulated in a general circulation model, Journal of Geophysical Research, 104, 13 791–13 823, 1999.

Adams, P. J., Seinfeld, J. H., Koch, D., Mickley, L., and Jacob, D.: General circulation model assessment of direct radiative forcing by the sulfate-nitrate-ammonium-water inorganic aerosol system, Journal of Geophysical Research (atmospheres), 106, 1097–1111, 2001.

Adamson, A. W. and Gast, A. P.: Physical Chemistry of Surfaces, Wiley, New York, sixth edn., 1997.

Andreae, M. O.: Climatic effects of changing atmospheric aerosol levels. Vol. 16: Future Climates of the World, in: World Survey of Climatology, edited by Henderson-Sellers, A., Elsevier, 1995.

AOPP: Reference Forward Model, http://www.atm.ox.ac.uk/RFM/, 2006.

Arons, A. B. and Kientzler, C. F.: Vapor pressure of sea-salt solutions, Trans. Am. Geophys. Union, 35, 722–728, 1954.

Banwell, C. N.: Fundamentals of Molecular Spectroscopy, McGraw-Hill Book Company, third edn., 1983.

Baron, P. A. and Willeke, K.: Aerosol Measurement – Principles, Techniques and Applications, Wiley, 2001.

Bass, S. F.: Optical Properties of Laboratory-generated polar stratospheric cloud particles, Ph.D. thesis, AOPP, University of Oxford, 2003.

Beer, R.: Remote Sensing by Fourier Transform Spectrometry, John Wiley and Sons Inc., 1992.

Bertie, J. E., Zhang, S. L., and Keefe, C. D.: Infrared intensities of liquids XVI. Accurate determination of molecular band intensities from infrared refractive index and dielectric constant spectra, Journal of Molecular Structure, 324, 157–176, 1994.

Blackford, D. B. and Simons, G. R.: Particle Size Analysis of Carbon Black, Particle Characterization, 4, 112–117, 1986.

Born, M. and Wolf, E.: Principles of Optics, Cambridge University Press, seventh edn., 2003.

Brabham, C.: Visit to Cambridge seeking advice on instrument design, 2004.

Brian, A.: Multiple Scattering by Aerosols, Master's thesis, AOPP, University of Oxford, 2001.

Buijsman, E., Mass, H. F. M., and Asman, W. A.: Anthropogenic NH3 emissions in Europe, Atmospheric Environment, 21(5), 1009–1022, 1987.

Carboni, E.: Aerosol optical depth retrievals from SEVIRI, unpublished data retrieved using new sea salt aerosol refractive index data and the AOPP RFM., 2008.

Cass, G. L.: On the relationship between sulfate air quality and visibility with examples in Los Angeles, Atmospheric Environment, 13, 1069–1084, 1979.

Chamaillard, K., Kleefeld, C., Jennings, S. G., Ceburnis, D., and O'Dowd, C. D.: Light scattering properties of sea-salt aerosol particles inferred from modeling studies and ground-based measurements, Journal of Quantitative Spectroscopy and Radiative Transfer, 101, 498–511, 2006.

Chamberlain, J.: The Principles of Interferometric Spectroscopy, John Wiley and Sons, 1979.

Chameides, W. L., Yu, H., Liu, S. C., Bergin, M., Zhou, X., Mearns, L., Wang, G., Kiang, C. S., Saylor, R. D., Luo, C., Huang, Y., Steiner, A., and Giorgi, F.: Case study of the effects of atmospheric aerosols and regional haze on agriculture: An opportunity to enhance crop yields in China through emission controls, Procedures of the National Academy of Sciences, 96, 13 626–13 633, 1999.

Charlson, R. J. and Heintzenberg, J.: Aerosol Forcing of Climate, John Wiley and Sons Ltd, 1994.

Charlson, R. J., Schwartz, S. E., Hales, J. M., Cess, R. D., Coakley Jr., J. A., Hansen, J. E., and Hoffman, D. J.: Climate forcing by anthropogenic aerosols, Science, 255, 423–430, 1992.

Clean Air Act: Http://www.epa.gov/air/caa/, 1990.

Cziczo, D. J. and Abbatt, J. P. D.: Infrared observations of the response of NaCl, MgCl2, NH4HSO4, and NH4NO3 aerosols to changes in relative humidity from 298 to 238K, J. Phys. Chem. A., 104, 2038–2047, 2000.

Cziczo, D. J., Nowak, J. B., Hu, J. H., and Abbatt, J. P. D.: Infrared spectroscopy of model tropospheric aerosols as a function of relative humidity: observations of deliquescence and crystallization, J. Geophys. Res, 102, 18 843–18 850, 1997.

d'Almeida, G. A., Koepke, P., and Shettle, E. P.: Atmospheric Aerosols; Global Climatology and Radiative Characteristics, A. Deepak Publishing, 1991.

Davies, C. N.: Size distribution of atmospheric particles, Journal of Aerosol Science, 5, 293–300, 1974.

Deirmendjian, D.: Electromagnetic Scattering on Spherical Polydispersions, Elsevier, New York, 1969.

Dignam, M. J.: Fourier Transform polarization spectroscopy, Applied Spectroscopy Reviews, 24, 99–135, 1988.

Dobbie, J. S., Li, J., Harvey, R., and Chylek, P.: Sea-salt optical properties and GCM forcing at solar wavelengths, Atmospheric Research, 65, 211–233, 2003.

Dorsey, N. E.: Properties of Ordinary Water -Substance in all its Phases: Water Vapor, Water and all the Ices, Reinhold Publishing Corp., New York, 1940.

Dubovik, O., Holben, B., Eck, T. F., Smirnov, A., Kaufman, Y. J., King, M. D., Tanre, D., and Slutsker, I.: Variability of absorption and optical properties of key aerosol types observed in worldwide locations, Journal of the Atmospheric Sciences, 59, 590–608, 2002.

Duce, R. A.: On the source of gaseous chlorine in the marine atmosphere, Journal of Geophysical Research, 74, 4597–4599, 1969.

Fang, L., Minzheng, D., Daren, L., and Okada, K.: Modification of sea-salt aerosols over the coastal area in China, Advance in Atmospheric Sciences, 15, 531–540, 1998.

Finlayson-Pitts, B. J. and Hemminger, J. C.: Physical chemistry of airborne sea salt particles and their components, Journal of Physical chemistry A, 104, 11 463–11 477, 2000.

Fox, M.: Optical Properties of Solids, Oxford University Press, 2001.

GeeJay Chemicals: Http://www.geejaychemicals.co.uk/default.htm, 2005.

Grainger, R., Lucas, J., Thomas, G. E., and Ewen, G. B. L.: Calculation of Mie Derivatives, Applied Optics, 43, 5386–5393, 2004.

GRIMM, 2006: GRIMM U-DMA, Universal Type Electrostatic Classifier, Grimm Technologies, Inc., 2006.

Hale, G. M. and Querry, M. R.: Optical properties of water in the near infrared, Applied Optics, 12, 564–568, 1973.

Harting, H.: Ber. deutsch. Akad. Wiss., 1948.

Hecht, E. and Zajac, A.: Optics, Addison-Wesley Publishing Company, 1980.

Hess, M., Koepke, P., and Schult, I.: Optical Properties of Aerosols and Clouds: The software package OPAC, Bull. Amer. Meteor. Soc., 79, 831–844, 1998.

Hinds, W. C.: Aerosol Technology: Properties, Behaviour and Measurement of Airborne Particles, J. Wiley, 1982.

Hinds, W. C.: Physical and chemical changes in the particulate phase, in: Aerosol Measurement, edited by Willeke, K. and Baron, P., Van Nostrand Reinhold, second edn., 2001.

Hodkinson, J. R. and Greensleaves, I.: Computations of light scattering and extinction by sphere according to diffraction and geometrical optics and some comparison with the Mie theory, Journal of the Optical Society of America, 53, 577–588, 1963.

Hummes, D., Stratmann, F., Neumann, S., and Fissan, H.: Experimental determination of a differential mobility analyser (DMA) in the nanometer size range, Particle and Particle Systems Characterization, 13, 327–332, 1996.

IPCC: Climate Change 2001: Working Group 1: The Scientific Basis, URL `http://www.ipcc.ch/ipccreports/tar/wg1/001.htm`, 2001.

IPCC: The Physical Basis of Climate Change, URL `http://ipcc-wg1.ucar.edu/wg1/wg1-report.html`, 2007.

Jarzembski, M. A., Norman, M. L., Fuller, K. A., Srivastava, V., and Cutten, D. R.: Complex refractive index of ammonium nitrate in the 2-20-mu m spectral range, Applied Optics, 42 (6), 922–930, 2003.

Jeong, M. J. and Li, Z.: Quality, compatibility, and synergy analyses of global aerosol products derived from the advanced very high resolution radiometer and Total Ozone Mapping Spectrometer, J. Geophys. Res., 110, 2005.

John, W., Wall, S. M., Ondo, J. L., and Winklmayr, W.: Modes in the size distributions of atmospheric inorganic aerosol, Atmospheric Environment, 24A (9), 2349–2359, 1990.

Junge, C. E.: Atmospheric Chemistry, in: Advances in Geophysics, edited by Landsberg, H. E., vol. 4, Academic Press Inc., New York, 1958.

Kalman, R. E.: A New Approach to Linear Filtering and Prediction Problems, J. Basic Eng., 82, 35, 1960.

Kiehl, J. T. and Briegleb, B. P.: The relative roles of sulfate aerosols and greenhouse gases in climate forcing, Science, 260 (5106), 311–314, 1993.

King, M. D., Kaufman, Y. J., Tanre, D., and Nakajima, T.: Remote sensing of tropospheric aerosols from space: past, present and future, Bull. Amer. Meteor. Soc., 80, 2229–2259, 1999.

Kuhn, H. G.: Atomic Spectra, Longmans, 1969.

Lajunen, L. H. J. and Peramaki, P.: Spectrochemical Analysis of Atomic Absorption and Emission, Royal Society of Chemistry, 2005.

Latham, J. and Smith, M. H.: Effect on global warming of wind-dependent aerosol generation at the ocean surface, Nature, 347, 372–373, 1990.

Lewis, E. R. and Schwartz, S. E.: Sea Salt Aerosol Production – Mechanisms, Methods, Measurements, and Models, American Geophysical Union, 2004.

Lewis, E. R. and Schwartz, S. E.: Comment on "size distribution of sea-salt emissions as a function of relative humidity", Atmospheric Environment, 40, 588–590, 2006.

Li, J., Ma, X., von Salzen, K., and Dobbie, S.: Parameterization of sea salt optical properties and physics of the associated radiative forcing, Atmospheric Chemistry and Physics, 8, 4787–4798, 2008.

Liger-Belair, G., Marchal, R., and Jeandet, P.: Close-up on Bubble Nucleation in a Glass of Champagne, Am. J. Enol. Vitic., 53 (2), 151–153, 2002.

Lightstone, J. M., Onasche, T. B., Imre, D., and Oatis, S.: Deliquescence, efflorescence, and water activity in ammonium nitrate and mixed ammonium nitrate/succinic acid microparticles, Journal of Physical Chemistry A, 104 (41), 9337–9346, 2000.

Loeb, N. G. and Schuster, G. L.: An observational study of the relationship between cloud, aerosol and meteorology in broken low-level cloud conditions, Journal of Geophysical Research - Atmospheres, 113, doi:10.1029/2007JD009763, 2008.

Lohmann, U. and Feichter, J.: Global indirect aerosol effects: a review, Atmos. Chem. Phys., 5, 715–737, 2005.

Mamakos, A., Ntziachristos, L., and Samaras, Z.: Diffusion broadening of DMA transfer functions. Numerical validation of Stolzenburg model., Journal of Aerosol Science, 38, 747–763, 2007.

Marinoni, A., Laj, P., Deveau, P. A., Marino, F., Ghermandi, G., Aulagnier, F., and Cachier, H.: Physicochemical properties of fine aerosols at Plan d'Aups during ESCOMPTE, Atmospheric Research, 74, 565–580, 2004.

Martin, S. T., Hung, H. M., Park, R. J., Jacob, D. J., Spurr, R. J. D., Chance, K. V., and Chin, M.: Effects of the physical state of tropospheric ammonium-sulfate-nitrate particles on global aerosol direct radiative forcing, Atmospheric Chemistry and Physics, 4, 183–214, 2004.

Maybeck, P. S.: Stochastic Models, Estimation and Control, vol. 1, Academic Press Inc., 1979.

McInnes, L. M., Covert, D. S., Quinn, P. K., and Germani, M. S.: Measurements of chloride depletion and sulphur enrichment in individual sea salt particles collected from the remote marine boundary layer, Journal of Geophysical Research, 99, 8257–8268, 1994.

McPheat, R. A., Bass, S. F., Newnham, D. A., Ballard, J., and Remedios, J. J.: Comparison of aerosol and thin film spectra of supercooled ternary solution aerosol, Journal of Geophysical Research, 107, doi: 10.1088/1748-9326/3/2/024004, 2002.

Menon, S., Unger, N., Koch, D., Francis, J., Garrett, T., Sednev, I., Shindell, D., and Streets, D.: Aerosol climate effects and air quality impacts from 1980 to 2030, Environmental Research Letters, 3, doi:10.1029/2001JD000641, 2008.

Metzger, S., Dentener, F. J., Jeuken, A., Krol, M., and Lelieveld, J.: Gas/aerosol partitioning II: Global modelling results, Journal of Geophysical Research, 107 D16, doi:0.1029/2001JD001103, 2002.

Mie, G.: Beitrage zur optik truber medien, speziell kolloidaler metallosungen, Ann. d. Physik, 25, 377, 1908.

Millero, F. J. and Sohn, M. L.: Chemical Oceanography, CRC Press, 1992.

Montgomery, R. B.: Water characteristics of Atlantic ocean and of world ocean, Deep-Sea Research, 5, 134–148, 1958.

Murphy, D. M., Anderson, J. R., Quinn, P. K., McInnes, L. M., Brechtel, F. J., Kreidenweis, S. M., Middlebrook, A. M., Posfai, M., Thomson, D. S., and Buseck, P. R.: Influence of sea-salt on aerosol radiative properties in the Southern Ocean marine boundary layer, Nature, 392, 62–65, 1998.

Myhre, G. and Grini, A.: Modelling of nitrate particles: importance of sea salt, Atmospheric Chemistry and Physics Discussions, 6, 1455–1480, 2006.

NASA: Goddard Earth Sciences Data and Information Services Centre Parameter Information Pages, http://daac.gsfc.nasa.gov/PIP, 2008.

Naylor, D. A., Schultz, A. A., and Clark, T. A.: Eliminating channel spectra in Fourier transform spectroscopy, Applied Optics, 27, 2603–2607, 1988.

Nemesure, S., Wagener, R., and Schwartz, S. E.: Direct shortwave forcing of climate by anthropogenic sulfate aerosol: sensitivity to particle size, composition, and relative humidity, Journal of Geophysical Research, 100, 26 105–26 116, 1995.

Neto, R. B. S., de Mendonca, J. P. R. F., and Lesche, B.: Determination of absolute values of refractive index of liquids using an interferometric method, Revista de Fisica Aplicada e Instrumentacao, 17, 74–79, 2004.

Norton, R. H. and Beer, R.: New apodizing functions for Fourier spectrometry, J. Opt. Soc. Am., 66, 259–264, 1976.

Oskouie, A. K., Wang, H. C., Mavliev, R., and Noll, K. E.: Calculated Calibration

Curves for Particle Size Determination Based on Time-of-Flight (TOF), Aerosol Science and Technology, 29, 433–441, 1998.

Peach, G.: Theory of the pressure broadening and shift of spectral lines, Advances in Physics, 30, 367–474, 1981.

Penner, J. E., Andreae, M., Annegarn, H., Barrie, L., Feichter, J. F., Hegg, D., Jayaraman, A., Leaitch, R., Murphy, D., Nganga, J., and Pitari, G.: Aerosols, their direct and indirect effects, in: Climate Change 2001: The Scientific Basis. Contribution of Working Group I to the Third Assessment Report of the Intergovernmental Panel on Climate Change, edited by Houghton, J. T., Ding, Y., Griggs, D. J., Noguer, M., van der Linden, P. J., Dai, X., Maskell, K., and Johnson, C. A., vol. 1, pp. 289–348, Cambridge University Press, first edn., 2001.

Peters, D. M. and Grainger, R. G.: Measurement of the optical properties of volcanic ash, 2004.

Pruppacher, H. R. and Klett, J. D.: Microphysics of Clouds and Precipitation: An Introduction to Cloud Chemistry and Cloud Electricity, Springer, 1997.

Putaud, J. P., Raes, F., Dingenen, R. V., Bruggemann, E., Facchini, M. C., Decesari, S., and Fuzzi..., S.: European aerosol phenomenology-2: chemical characteristics of particulate matter at kerbside, urban, rural and background sites in Europe, Atmospheric Environment, 38 (16), 2579–2595, 2004.

Querry, M. R., Holland, W. E., and Waring, R. C.: Complex refractive index in the infrared for NaCl, NaNO3, and NaHCO3 in water, J. Opt. Soc. Am., 66, 830–836, 1976.

Quinn, P. K., Charlson, R. J., and Bates, T. S.: Simultaneous observations of ammonia in the atmosphere and ocean, Nature, 335, 336–338, 1988.

Remsberg, E. E.: Stratospheric aerosol properties and their effects on infrared radiation, Journal of Geophysical Research, 78 (9), 1401–1408, 1973.

Robinson, R. A.: The vapour pressure and osmotic equivalence of sea water, J. Marine. Biol. Assoc. UK, 33, 449–454, 1954.

Rodgers, C. D.: Inverse Methods for Atmospheric Sounding: Theory and Practice, vol. Series on Atmospheric, Oceanic and Planetary Physics - Vol. 2, World Scientific Publishing Co. Pte. Ltd., 2000.

Rothman, L. S.: The HITRAN 2004 molecular spectroscopic database, Journal of Quantitative Spectroscopy and Radiative Transfer, 96, 139–204, 2005.

Salhotra, A. M., Adams, E. E., and Harleman, D. R. F.: The alpha, beta, gamma of evaporation from saline water bodies, Water Resources Res., 23, 1769–1774, 1987.

Savoie, D. L. and Prospero, J. M.: Particle size distribution of nitrate and sulfate in the marine atmosphere, Geophysical Research Letters, 9, 1207–1210, 1982.

Schaap, M., Muller, K., and ten Brink, H. M.: Constructing the European aerosol nitrate concentration field from quality analysed data, Atmospheric Environment, 36, 1323–1335, 2002.

Segelstein, D. J.: The complex refractive index of water, Master's thesis, University of Missouri – Kansas City, 1981.

Seinfeld, J. H. and Pandis, S. N.: Atmospheric Chemistry and Physics : From Air Pollution to Climate Change, J. Wiley and Sons, 1998.

Shettle, E. P. and Fenn, R. W.: Models for the Aerosols of the Lower Atmosphere and the Effects of Humidity Variations on Their Optical Properties, AFGL-TR-79-0214, 1979.

Simon, D.: Kalman Filtering, Embedded Systems programming, pp. 72–79, 2001.

Sjogren, S., Gysel, M., Weingartner, E., Baltensperger, U., Cubison, M. J., Coe, H., Zardini, A. A., Marcolli, C., Krieger, U. K., and Peter, T.: Hygroscopic growth and water uptake kinetics of two-phase aerosol particles consisting of ammonium sulfate, adipic and humic acid mixtures, Journal of Aerosol Science, pp. 157–171, 2007.

Syvitski, J. P. M.: Principles, Methods and Application of Particle Size Analysis, Cambridge University Press, 2007.

Tang, I. N. and Munkelwitz, H. R.: Simultaneous determination of refractive index and density of an evaporating aqueous solution droplet, Aerosol Sci. Tech., 15, 201–207, 1991.

Tang, I. N. and Munkelwitz, H. R.: Water Activities, Densities, and Refractive-Indexes of Aqueous Sulfates and Sodium-Nitrate Droplets of Atmospheric Importance, Journal of Geophysical Research - Atmospheres, 99 (D9), 18 801–18 808, 1994.

Tang, I. N., Tridico, A. C., and Fung, K. H.: Thermodynamic and optical properties of sea salt aerosols, Journal of Geophysical Research - Atmospheres, 102 (D19), 23 269–23 275, 1997.

ten Brink, H. M., Kruisz, C., Kos, G. P. A., and Berner, A.: Size/composition of the light-scattering aerosol in the Netherlands, Atmospheric Environment, 37, 3955–3962, 1997.

Thomas, G. E., Bass, S. F., Grainger, R. G., and Lambert, A.: Retrieval of aerosol refractive index from extinction spectra using a damped oscillator band model, Applied Optics, 44, 1332–1341, 2004.

Thomsen, D. C.: Bruker IFS 66v Fourier Spektrometer, http://www.ifkp.tu-berlin.de/menue/arbeitsgruppen/ag_thomsen/labore/infrarot, 2008.

Thomson, W.: On the equilibrium of vapour at a curved surface of liquid, Phil. Mag., 42, 448–452, 1871.

Thomson-Scientific: ISI Web of Knowledge, URL `http://apps.isiknowledge.com/`, 2008.

Toon, O., Pollack, J., and Khare, B.: The optical constants of several atmospheric species: Ammonium sulfate, ammonium oxide and sodium chloride, Journal of Geophysical Research, 81, 5733–5748, 1976.

Torres, O., Bhartia, P. K., Herman, J. R., Ahmad, Z., and Gleason, J.: Derivation of aerosol properties from satellite measurements of backscattered ultraviolet radiation – Theoretical basis, Journal of Geophysical Research, 103 (D14), 17 099–17 110, 1998.

Twomey, S.: On the nature and origin of cloud nuclei, Bull. de l'Obseratoire du Puy de Dome, 1, 1–19, 1960.

Twomey, S.: The composition of cloud nuclei, Journal of Atmospheric Science, 28, 377–381, 1971.

Twomey, S.: Influence of pollution on short wave albedo of clouds, Journal of Atmospheric Sciences, 34, 1149–1152, 1977a.

Twomey, S.: Atmospheric Aerosols, Elsevier, New York, 1977b.

Twomey, S. and McMaster, K. N.: The production of condensation nuclei by crystallizing salt particles, Tellus, 7, 458–461, 1955.

Vinoj, V. and Satheesh, S. K.: Direct and indirect radiative effects of sea-salt aerosols over Arabian Sea, Current Science, 86, 1381–1390, 2004.

Volz, F. E.: Infrared refractive index of atmospheric aerosol substances, Applied Optics, 11, 755–759, 1972.

Volz, F. E.: Infrared optical-constants of ammonium sulfate, sahara dust, volcanic pumice, and flyash, Applied Optics, 12 (3), 564–568, 1973.

Wayne, R.: Chemistry of Atmospheres, 2nd edn., Oxford University Press, 1991.

Weis, D. D. and Ewing, G. E.: Water content and morphology of sodium chloride particles, J. Geophys. Res., 104, 21 275–21 285, 1999.

Welch, G. and Bishop, G.: An Introduction to the Kalman Filter, department of Computer Science, University of North Carolina, 2006.

White, F. M.: Fluid Mechanics, McGraw-Hill, fifth edn., 2003.

Winter, B. and Chylek, P.: Contribution of sea salt aerosol to the planetary clear sky albedo, Tellus, 49 (B), 72–79, 1997.

Yunus, W. M. M.: Temperature dependence of refracrive index and absorption of NaCl, MgCl2, and Na2SO4 solutions as major components in natural seawater, Applied Optics, 31 (16), 2963–2970, 1992.